Optimal Control for Race Car Minimum Time Maneuvering

S. van Koutrik

TUDelft Delft University of Technology

Delft Center for Systems and Control

Optimal Control for Race Car Minimum Time Maneuvering

MASTER OF SCIENCE THESIS

For the degree of Master of Science in Systems and Control at Delft University of Technology

S. van Koutrik

March 19, 2015

Audi Sport

TUDelft
Delft
University of
Technology

DCSC

Abstract

Minimizing the time needed to travel a prescribed distance is the main development goal in motorsports. In racing car development, simulations are used to predict the effect of design parameter changes on vehicle performance. If approached as an optimal trajectory planning problem, a maneuver simulation can be used to determine not only the maneuver time, but also to identify the performance limitations on the system. This thesis describes the development and implementation of an optimal trajectory planning method using optimal control for short maneuvers. The requirements and modeling decisions are based on the application of the method to example problems related to Traction Control (TC) design.

The model for the method is based on a study of steady-state acceleration limits and stability. The rigid two-track model resulting from this study includes lateral and longitudinal load transfer, a nonlinear tire model, a limited-slip differential and aerodynamic downforce. An important contribution is the omission of wheel rotational velocities from the model, reducing the number of states by four and relaxing the requirements on the discretization interval. Possible misuse of this formulation is prevented by a constraint representing wheel rotational stability limitations. The formulation is validated by comparison to a reference model which includes wheel rotational velocities.

The optimal trajectory planning method is formulated as an optimal control problem. The cost function is the maneuver time, and the constraints consist of the system dynamics and maneuver boundaries. The time-based dynamics are transformed into spatial dynamics, and a curvilinear coordinate system is used.

The optimal control problem is discretized using a full collocation method, and the state and input trajectories are parametrized in terms of B-spline coefficients. The resulting problem is solved using a Non-Linear Programming (NLP) solver. Interior-point solver IPOPT and Sequential Quadratic Programming (SQP) solver SNOPT are compared on various small problems. For this application IPOPT appears to be superior over SNOPT. The first order derivative information of the constraints required for IPOPT is approximated using sparse-finite differences, and the cost function gradient is calculated analytically. The precision of

the method is assessed in a study of maneuver time dependency on mass. It appears that precision is mainly affected by convergence of the solver to various local minima. As such, the use of distance-dependent constraints and warm-start are employed for improving precision.

The optimal trajectory for a hairpin with various radii is studied in detail. Special attention is paid to tire friction potential utilization and vehicle stability according the Lyapunov's First Method. For the given parameters it is shown that the optimal solution involves instances of overdriving either the front or rear axle. It is also shown that the vehicle is open-loop locally unstable on intervals along the optimal trajectory.

In another simulation study, the reaction of the control inputs to temporary reductions in tire-road friction and perturbations to the yaw rate and body slip angle on turn-exit are evaluated. The most important result of this study is that the longitudinal control was found to be the primary means for rejecting such disturbances. The study also showed that steering angle changes are used as additional means for disturbance rejection if the perturbation is large enough to saturate the reduction of longitudinal control.

The sensitivity of maneuver time and optimal trajectory to vehicle mass is studied by the use of so-called sensitivity differentials. This is done using a well-developed theoretical framework for parametric sensitivity for barrier methods, implemented in the software package sIPOPT. The sensitivity study can be seen as a proof of concept of the sensitivity differential approach for the race car MTM application.

Table of Contents

List of Figures

List of Tables

Acknowledgements

First of all, I would like to thank my supervisor Tamás Keviczky for his useful input during both the real-life and Skype meetings. The critical feedback on intermediate work and help with fundamental insight have been of great value. Furthermore, the assistance during the writing of this thesis is greatly appreciated and hereby acknowledged.

In addition, I would like to thank Christopher Zinke, for the interesting discussions on optimal driving. Furthermore, the critical questions to both planning and content have been of great value.

Thank you as well to Martin Kalkofen for the useful suggestions and discussions on methodological level. I would also like to thank Timo Völkl for his helicopter view, helping to maintain the big picture during the longer periods of methodological development. Furthermore, I would like to thank Audi Sport for giving me the opportunity to spend my time working on this fascinating topic in an inspiring environment.

Finally, I would like to thank Michael Geary for proofreading the thesis.

Delft, University of Technology   S. van Koutrik
March 19, 2015

Chapter 1

Introduction

The aim in motorsport is to win races. One of the main development goals for achieving this, is traveling a prescribed distance in minimal time. This distance is usually a lap around a given circuit. The problem is constrained by the physical boundaries of the race track, and by the restrictions on car layout as defined by a rule book. Within the limits of these rules, teams and constructors develop cars to minimize lap time. During this process, simulations are used to predict the effect of vehicle setup and design parameter changes on vehicle performance.

1-1   Background and goals

Historically, race car requirements have been expressed in terms of accelerations. An important statement concerning time optimal driving is made by Peter G. Wright, former technical director of Formula 1 team Lotus, and quoted in [1]:

"Driving a car as fast as possible (in a race) is all about maintaining the highest possible acceleration level in the appropriate direction"

This quote is illustrated in Figure 1-1. It shows a simple 90° turn, a vehicle, and its acceleration vector at several instances. As can be seen, the initial acceleration vector is pointing rearwards, as the vehicle is decelerating. In the middle of the turn, the car is driving in a curved path, requiring a centripetal acceleration. On the last point, the car is accelerating forward. Between these points the car is subject to a combination of longitudinal and lateral acceleration.
Indeed, the shortest time is achieved for maximal average corner speed, requiring high lateral acceleration. The time to this point is minimized by braking as late as possible using the vehicle's maximum deceleration potential. Finally, at the end of the corner maximum forward acceleration is desired.

One of the main limitations on vehicle accelerations is the force that the tires can exert to the road. It appears that for tires delivering a combined longitudinal and lateral force, the
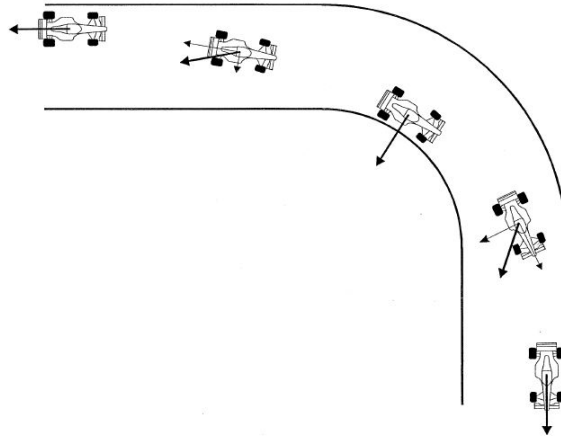
Figure 1-1: Illustration of the vehicle acceleration vector in a typical 90 degree turn. Figure adopted from [2].

magnitude of the vector sum of the two forces is nearly constant [1]. This has led to the concept of the "g-g" diagram. The "g-g" diagram represents the bounds of the vehicle on the $A_x - A_y$ plane, where A_x and A_y denote the longitudinal and lateral acceleration respectively. Milliken & Milliken state the following about the requirements of a car with the goal of minimizing lap time:

- It should provide the largest "g-g" maneuvering areas throughout the range of operating conditions

- It should provide vehicle stability and control characteristics that enable a skilled driver to operate at or near these acceleration limits.

Development in race car design is most often based on the improvement of either of these two points. Area's of development include generation of aerodynamic down-force, improvement of tire friction and improvement of suspension characteristics. In decision making, engineers make use of simulations to quantify the influence of such parameter variations on lap time. In one class of methods, the vehicle is approximated by a point mass, which has accelerations limits represented in a "g-g" diagram, possibly dependent on velocity. The method calculates the optimal velocity profile on a curvature defined by the user. Essentially, the assumption is made that all states are constant for short discrete periods of time. The driving line is divided in short segments of constant radius and on each segment a constant yaw rate, constant velocity and constant longitudinal and lateral acceleration are assumed. This assumption is justified by the fact that circuit driving is known to be smooth, resulting in low yaw accelerations [3]. In literature, these methods are referred to as Quasi-Steady State (QSS) methods [3]. A more detailed explanation can be found in [3] and [4].

The disadvantages of QSS methods are the assumption of a fixed driving line (although in [5] a method of line optimization using "g-g" diagrams is presented), and the omission of transients. The latter is illustrated in Figure 1-2. The figure shows a left-right combination of turns. As
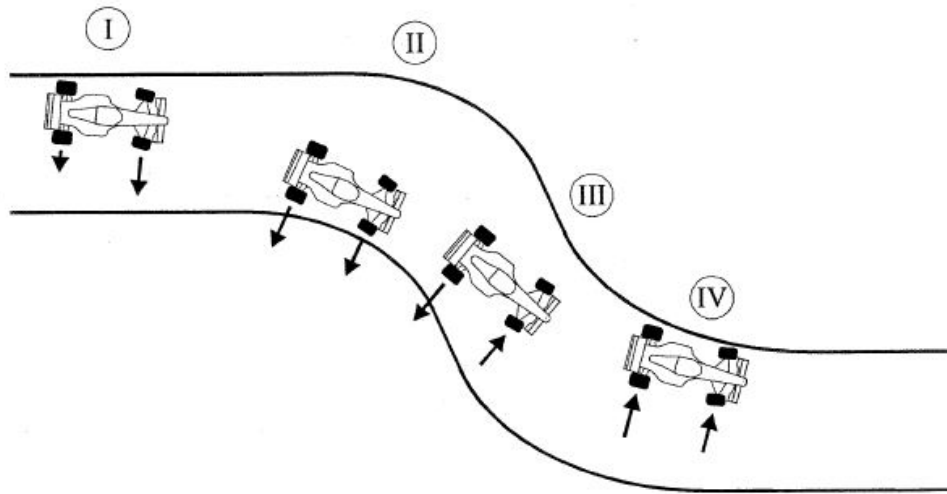
Figure 1-2: Illustration of a typical lane-change maneuver, including a lateral tire force representation. Figure adopted from [2]

can be seen the yaw rate of the car is in clockwise direction in the middle of the first turn. In the second turn, the yaw rate is in counter-clockwise direction. The transition between the two requires a yawing moment, and thus requires unbalanced forces (situation III in the Figure 1-2). As a result, the car cannot achieve an acceleration as given by steady-state "g-g" diagram at this point in time. In general, neglecting the dynamics will make the theoretical optimum found from a QSS method unobtainable in reality [3].

This leads to the problem of finding the so-called control inputs which make use of the transient dynamics in an optimal fashion. The control inputs are typically the front wheel steering angle and accelerating and braking torque on the wheels. The problem of finding the optimal inputs can be seen as an optimal trajectory planning problem. The question we are aiming to answer is: What is the sequence of control inputs and vehicle states leading to the shortest possible maneuver time? In literature describing optimal control methods this problem is referred to as the Minimal Time Maneuvering (MTM) problem. We will adopt this terminology from this point on.

1-1-1   Motivation for optimal trajectory generation for short maneuvers

First, a relevant topic in motorsport engineering is the performance of the drivers themselves. Many books have been written on expert race driver techniques. Yet, drivers at the top level of motorsport exhibit different styles of driving, as the experience of Audi Sport in the Le Mans Prototype 1 (LMP1) racing class has shown. A large difference in lateral tire slip during the first part of turns is observed, accompanied by minor differences in driving path. In order to follow their own preference in trajectory, the drivers demand a different vehicle set-up, making an optimal strategy for all drivers difficult to identify. Better understanding of the theoretically optimal trajectory can lead to the right driver instructions, and corresponding vehicle adjustments.

A second motivation of optimal trajectory planning lies in the technology allowed in certain race classes. In the LMP1 class, drivers are allowed to be assisted by so-called Traction Control (TC) systems. These systems receive the driver's throttle pedal input, and adjust the torque delivered to the driven wheels. As a result, part of the control inputs influencing the maneuver time are decided by a semi-automated system. Brayshaw [3] states two functions of TC:

- Ensure lateral/directional stability

- Provide effective force transmission of the tractive forces to the road surface

These two represent a trade-off, since tire longitudinal force may be sacrificed to maintain lateral vehicle stability. The criterion for stability is however not completely defined by the vehicle-traction control combination; the control of the lateral dynamics of the car is shared with the driver, using front wheel steering as a control input. It remains a question if a traction controller that renders the car stable for open loop steering inputs, will in fact increase the minimal maneuver time compared to a traction controller which requires steering control in the stabilization of the lateral dynamics of the car. For that reason, it is believed that knowing the optimal trajectory leads to useful understanding for the development of TC systems.

1-1-2 Main goal

The objective of this thesis is to develop a method using optimal control for minimum time maneuvering of a racing car. The method and model are tailored for investigating the optimal cooperation between the human race driver and the semi-automated traction control system. This goal poses a set of requirements to the method. First of all, the model should include all effects that are relevant to the qualitative control of vehicle dynamics. Furthermore, the method should be precise. Specifically, small variations in parameters should lead to a correspondingly small change in trajectory and maneuver time. Finally, as a rapid prototyping method, it should be flexible to allow variations to the vehicle model and to the problem formulation.

1-2 Previous work and contributions

Several authors have applied optimal control to the race car MTM before. Casanova [2] used a direct multiple shooting approach for transcribing the problem defined over an entire lap into a nonlinear program. The model proposed [2] uses a two-track vehicle model with nonlinear tires and aerodynamic downforce. The method was successfully used to describe the influence of vehicle center-of-gravity location and yaw inertia [6] on minimum maneuver time. The CPU-time for a full lap was said to be on the order of magnitude of hours. Kelly [7] used a single shooting approach for short maneuvers. The method does not require full access to the state vector, and as such is suitable for application to black-box models. The single shooting approach was applied successfully to the nonlinear, possibly unstable system by the usage of stability constraints on regular intervals of the maneuver. The method was

extended to longer maneuvers using a receding horizon approach and it was shown to be able to handle a model including suspension dynamics. The author reports a CPU-time of eight hours for solving an entire lap on the Circuit of Jerez.

Perantoni et al. have recently produced a series of publications on optimal control for Formula 1 cars [8], [9], [10]. In [8] a full collocation approach was applied to the simultaneous optimization of trajectory and vehicle parameters. The CPU-time for one lap on the race track of Barcelona with a discretization interval of 2m was said to be around 15 minutes. In [9] a direct orthogonal collocation method implemented in the software package GPOPS-II [11] was implemented for the conjunction of the race car MTM problem and the energy strategy in the presence of hybrid and fuel energy consumption limitations. Finally, in [10] the method was extended to solve optimal control problems for maneuvers defined on a three-dimensional surface, taking into account race track elevations and banking.

Rucco et al. produced a series of papers [12], [13], [14], in the development of a method using optimal control for a rigid two-track model with load-transfer [15]. A projection operator nonlinear optimal control technique [16] was used in this work, which was shown to be suitable for both long maneuvers and a fine mesh grid. The computation time for a test lap with a 10cm discretization interval, leading to problem size of 251000 variables was said to be solved with a CPU time of less than 35 minutes. An interesting feature of the method is that it produces feasible iterates at every optimization step. All intermediate steps therefore satisfy the system dynamics, giving an interesting impression of how the virtual driver converges to an optimum.

Closely related to the race car MTM problem is the work published on real-time Nonlinear Model Predictive Control (NMPC) for autonomous driving. Diehl et al. [17] apply an NMPC method to an advanced vehicle model, using Bock's multiple shooting method based on [18], and [19] for obstacle avoidance. Verschueren et al. [20] address the real-time control of autonomous vehicles by a minimal-time formulation of the problem. In order to be able to make use of efficient algorithms which rely on least-squares formulations and the generalized Gauss-Newton method, the objective function was reformulated into a least-square form. The method was applied to a miniature race-car setup, and real-world experiments were conducted. For this work, a single-track model without tire slip was used. The author reports that for future work a higher-fidelity vehicle model including slip is needed.

Contributions   In this thesis a method is developed that is suitable for the qualitative analysis of control for short maneuvers. A direct collocation method is used to transcribe the optimal control problem into a nonlinear program. The state and input trajectories are represented by B-splines, of which the control points are the decision variables for the nonlinear program. The contributions of this thesis are listed below:

- Different modeling alternatives are compared based on their influence on steady-state acceleration potential and linearized planar dynamics. The study has led to the incorporation of lateral and longitudinal load transfer, aerodynamic downforce and a limited-slip differential in the two-track model.

- Contrary to definitions found in other MTM literature, the wheel rotational velocities are omitted from the model. To incorporate the limitations that wheel dynamic stability places on tire force, additional constraints are defined which exclude unstable wheel dynamics from the solution space. This approach is validated in a numerical study, by a comparison with a reference model which uses wheel rotational velocities.

- For solving the Non-Linear Programming (NLP) a Sequential Quadratic Programming (SQP) method and an interior-point method are compared in a simulation study with different maneuvers.

- The nominal solution of a hairpin maneuver at three different velocities is studied in detail. Some properties of optimal driving relevant for TC at a hairpin with three different turn radii are highlighted. Tire friction utilization and normalized tire slip for the different wheels during the maneuver are studied. In relation to this, the stability of the vehicle along the optimal trajectory is assessed by the application of Lyapunov's First Method to a reduced system. The time-minimal trajectory of the steering angle is related to the zeros of the this linearized reduced system along the trajectory.

- A perturbation analysis is presented, in which the state and available tire-road friction coefficient is disturbed and the relative magnitude of the steering angle and longitudinal control in the time-minimal rejection of the disturbance are compared.

- The precision of the method in predicting the maneuver time as a function of vehicle mass is assessed.

- A proof of concept for performing parametric sensitivity studies by the calculation of sensitivity differentials is presented.

1-3 Thesis structure

Chapter 2 describes different modeling alternatives, and compares them on steady-state acceleration limits and linearized dynamics. From this, the model for the remainder of the thesis is deducted. In addition, the maneuver model and related curvilinear coordinate system are presented in this chapter.

Chapter 3 presents the formulation of the race car MTM problem in the optimal control framework. The reformulation of the time-based dynamics to spatial dynamics is described. Furthermore, this chapter handles the incorporation of some model properties via algebraic constraints. In addition to the formulation of the system dynamics without wheel rotational velocities, a reference model including them is presented as well. Non-smooth model characteristics are approximated by smooth functions, to render the formulation suitable for the application of NLP techniques.

Chapter 4 focuses on the transcription of the optimal control problem into an NLP using a full collocation approach. This includes the approximation of the integration of the differential equations, and the representation of state and input trajectories using B-splines.

The computation of the derivative information needed by the NLP is described as well. A simulation study is presented, in which the SQP solver SNOPT and the interior-point solver IPOPT are compared based on their suitability for this application. Finally, the required discretization interval is determined in another numerical study.

Chapter 5 contains three different simulation studies. First, the modeling choice to neglect wheel rotational velocity is validated by the comparison with a reference model. In the second study, the optimal control solution for a hairpin at three different radii is studied in detail. Some questions related to the design of a time-optimal TC system are answered. Furthermore, the stability of the solution along the optimal trajectory is assessed using Lyapunov's First Method. In the third study, the optimal reaction of the control inputs to a disturbance to the vehicle state and the tire-road friction coefficient is described.

Chapter 6 assesses the precision of the race car MTM method in describing the relation of maneuver time, trajectory and vehicle mass. Two methods for improving the precision are described and implemented. Furthermore a parametric sensitivity study using sensitivity differentials is performed. A brief overview of the theoretic framework behind the method is given, as well as some first results of the sensitivity of the solution with respect to vehicle mass.

Chapter 7 summarizes the conclusions and contributions and lists the recommendations for future work.

Appendix A and **B** list the vehicle model equations and baseline model parameters.

Chapter 2

Vehicle and maneuver modeling

Models for simulation of high performance racing vehicles have been described in [3], [7], [21]. In many race car simulations, as many details as possible are incorporated, with the limit decided by simulation robustness and computation time [21]. However, our purpose is not give a very precise representation of the vehicle, since the target is not to do give an accurate prediction of the maneuver time for a specified vehicle. Instead, it is important to incorporate the dynamics and non-linear aspects of the vehicle that qualitatively influence vehicle control and stability. For this reason, different modeling alternatives are considered and compared in two different studies. As a measure of performance, modeling alternatives are compared on their acceleration potential for combined longitudinal and lateral acceleration. This is done in Section 2-3. Section 2-4 describes a second second study, where the modeling alternatives are compared on vehicle stability characteristics.

The vehicle model for the study of this thesis is roughly based on a Le Mans Prototype 1 (LMP1) vehicle. The baseline parameters used for the examples are shown in Table B-1. Based on the study and the requirements of the Minimal Time Maneuvering (MTM) method, a vehicle model is composed. The modeling of the maneuver and coordinate system are described in Section 2-6.

2-1   Main vehicle model

Vehicle modeling is subdivided into the following aspects:

- Planar vehicle dynamics

- Tire model

- Differential

- Wheel loads

In MTM and general vehicle dynamics simulation literature, different models for the elements are described. This section describes the most common model from other MTM work, and some alternatives from literature for some of its elements. Afterwards, the effect of these alternatives on steady-state acceleration limits and stability are studied for the parameters in Table B-1.

2-1-1   Planar vehicle dynamics

One of the most simple, if not the simplest model of the planar vehicle dynamics is a point mass in the Cartesian two-dimensional space. The point mass has acceleration limits in x and y direction, representing the friction limits of the tires. The point mass model is used in e.g. [5] for optimal driving path generation. The largest disadvantage however is its inability to represent the yaw dynamics of the vehicle.

An alternative which does allow this, is the single-track (or bicycle) model [1], [22]. It has obtained its name from the fact that it has only one track, resulting in one tire per axle. The vehicle has two translational and one rotational degree of freedom. The forces accelerating the vehicle in x, y and rotational direction are supplied by the tires and imposed by tire slip. Several variants of the bicycle model are published in literature. Milliken [1] assumes that the tire forces are linearly dependent on slip. This proves to be useful in the analysis of vehicle yaw dynamics and stability, but is not suitable for investigating vehicle behavior on its acceleration limits. On the other hand, [22] and [23] include a non-linear tire model, including force saturation at higher tire slips. The equations of motion for the bicycle model were derived in e.g. [24], and are presented in Appendix A-2.

An alternative representation of the vehicle with a higher fidelity is the two-track model (Figure 2-1), used in [7], [3], [2], [8]. The model features a different slip condition for all four tires, as well as the possibility to include wheel load distribution changes with acceleration. Furthermore, it allows for the modeling of a mechanical differential providing a coupling between rotation of different wheels. The equations of motion for the two-track model are given in Appendix A-3.

2-1-2   Tire forces

The tire forces in the planar vehicle model are often modeled as a function of slip and vertical force:

$$(F_x, F_y) = F(s_y, s_x, F_z) \tag{2-1}$$

Where F_x and F_y denote the tractive and lateral force in the tire reference frame. s_x and s_y represent longitudinal and lateral slip, given by:
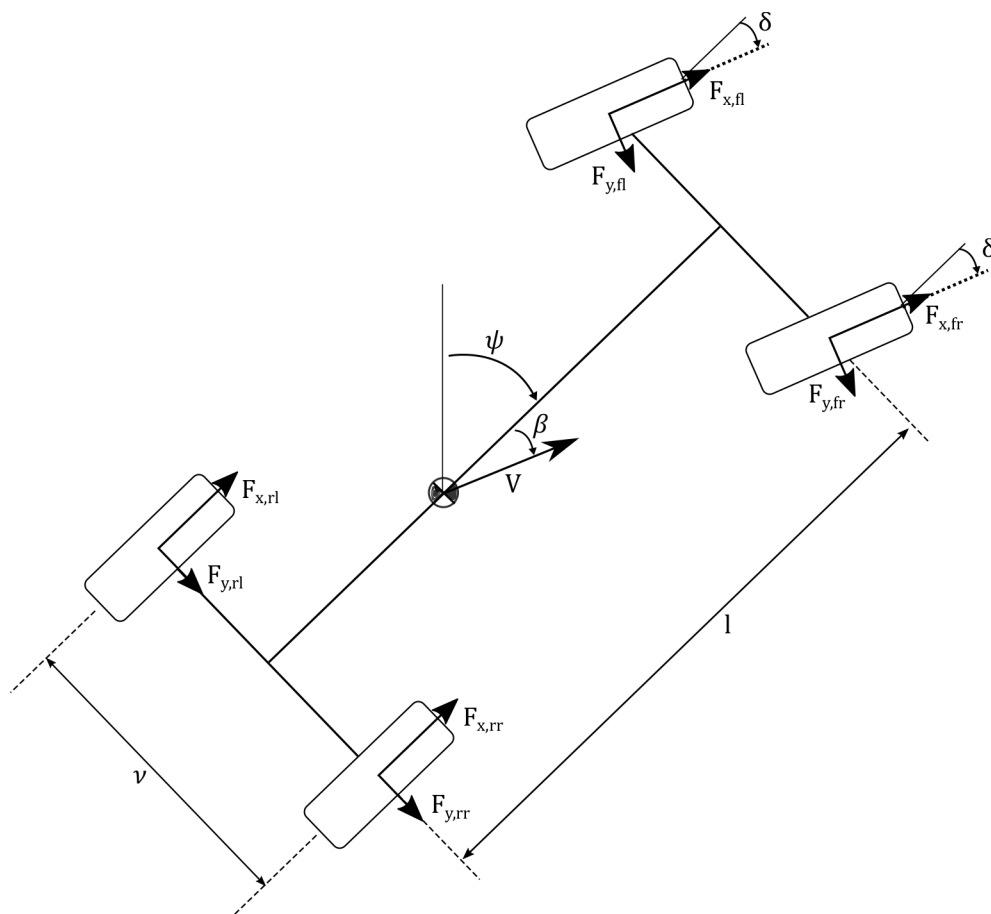
Figure 2-1: Two-track model
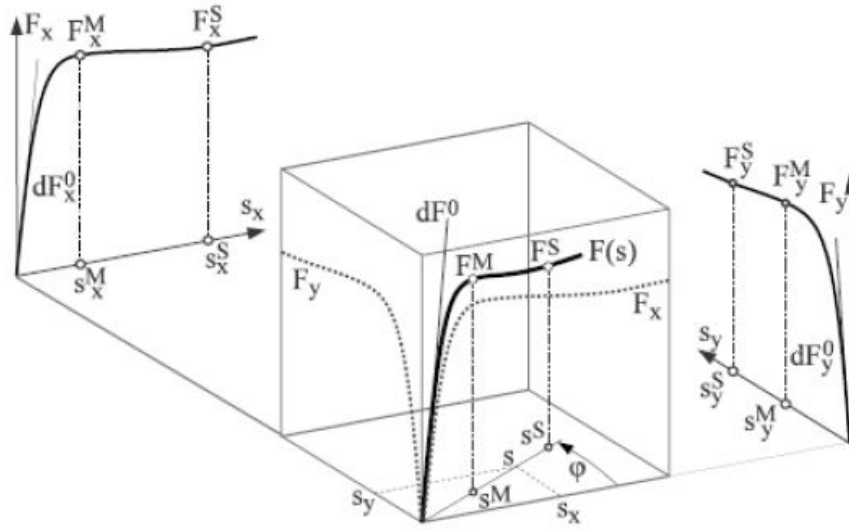
Figure 2-2: Example of typical tire force characteristics. As can be seen, there is a clear interaction between longitudinal and lateral tire force. Figure adopted from [25]

$$s_y = \frac{v_y}{\omega R_{\text{eff}}} \tag{2-2}$$

$$s_x = \frac{\omega R_{\text{eff}} - v_x}{\omega R_{\text{eff}}} \tag{2-3}$$

Where R_{eff} and ω are the effective rolling radius and wheel angular velocity respectively. For describing relation (2-1), the TMeasy tire model is used [25]. The model is characterized by three points, shown in Figure 2-2:

- Cornering stiffness dF^0, which defines the slope of the force-slip curve around the origin

- Maximum tire force F^M and corresponding slip s^M.

- Pure sliding force F^S and corresponding slip s^S.

These parameters are defined for two different vertical loads, making the tire characteristics load dependent. Furthermore, longitudinal and lateral characteristics can be defined independently. Although the model is simple, it captures the relevant characteristics of a racing car tire and is therefore a good alternative for the models used in [8] and [2]. The equations describing relation (2-1) are given in [25], p59.

2-2   Modeling alternatives

As mentioned before, this work is not about prediction of performance differences for small parameter variations, but rather for a qualitative study of control for minimum time maneu-

vering. Therefore, only the model effects influencing system dynamics and control qualitatively are relevant. For computational efficiency, all other effects are simplified as much as possible. In this section we consider some effects which have been modeled in various ways in available literature.

2-2-1 Mechanical differential

If a two-track model is used, a differential model can be included. Race cars are often equipped with a torque transferring rear differential, which provides a coupling between the rotation of the two wheels and the engine [1]. This coupling influences both the yaw dynamics and the capability of the rear axle to provide effective force transmission of tractive forces to the road surface [3]. In handling simulation, roughly four differential configurations are used: open, locked, viscous and limited slip.

An open differential can be modeled as follows:

$$T_{rl} = T_{rr} = \frac{T_E}{2} \tag{2-4}$$

Where T_{rl} and T_{rr} represent the torque on the left and right wheel, and T_E the torque from the drivetrain.

Locked The locked differential is the other extreme, since it assumes the two wheels to be on one single rigid body [7], [1]. Hence,

$$\omega_{rl} = \omega_{rr} \tag{2-5}$$
$$T_{rr} + T_{rl} = T_E \tag{2-6}$$

As a result, the distribution between T_{rl} and T_{rr} is decided by the slip and vertical load conditions on the two tires.

Limited slip differential A limited slip differential is designed to incorporate the advantages of the open and the locked configuration [1]. On the one hand it allows for different wheel speeds when the engine torque is small, to not cause the inside wheel to drag along the track during sharp turns. On the other hand the coupling between the wheels is increased with engine torque, allowing for torque transfer from a spinning wheel to a wheel with superior traction. In [7], a clutch model with a combination of Coulomb and viscous friction is used to represent a limited slip differential. In [8] the differential is modeled as a viscous clutch, hence the torque transfer between the two wheels is proportional to the speed difference between them. In [2] and [3] the limited slip differential is modeled as pure Coulomb friction, with the value of the Coulomb friction dependent on the engine output torque. Although not reported in MTM literature, this configuration can be expected to cause difficulties in gradient-based optimization, due to the sharp transition in torque transfer around the origin. This problem is handled in Section 3-6. A graphical representation of the viscous, Coulomb and combined differential friction models is shown in Figure 2-3.
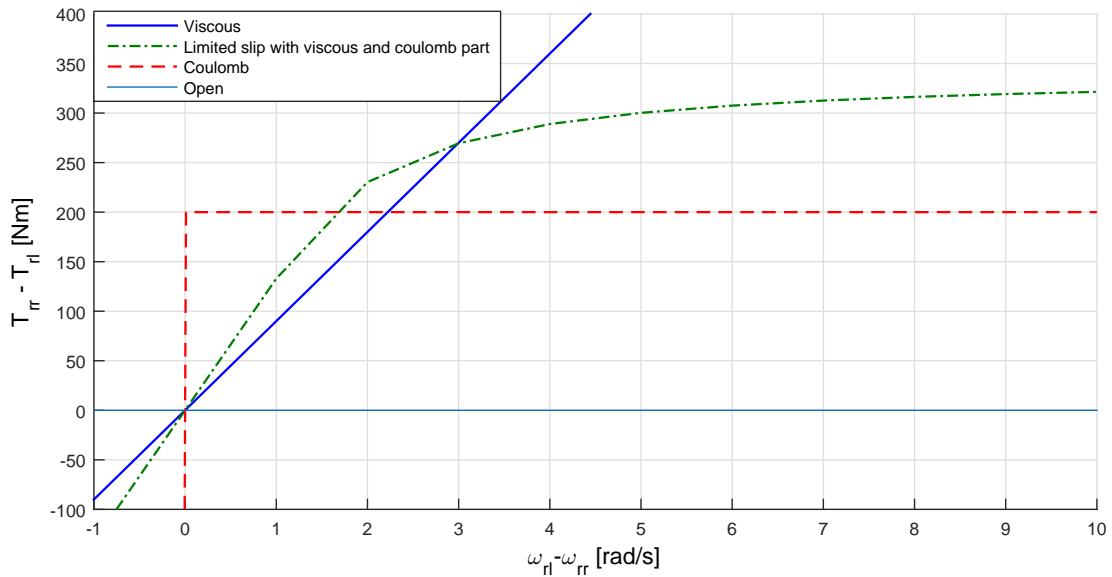
Figure 2-3: Graphical representation of various differential configurations. Note that the actual values on the vertical axis are not fixed, and in case of the non-viscous differentials dependent on the maximum locking torque

Approach   Summarizing, it can be said that the open differential and the locked differential form two ends of the spectrum, and that the limited slip differential is used to combine the advantages of both. In Section 2-3 and 2-4 the open differential and locked differential are compared in various cases, leading to the eventual choice of differential model.

2-2-2   Wheel load distribution

The planar tire forces F_x and F_y are a function of the wheel loads F_z. In reality, many effects influence the distribution of wheel loads on the vehicle, and therefore the planar vehicle dynamics. In race car MTM literature, the effects of aerodynamic forces and wheel load changes due to planar acceleration is included. In the following, we will describe briefly how this is modeled.

Aerodynamic loads   Racing cars make use of aerodynamic effects on its body to improve the performance. Besides a drag force, which is often modeled as a longitudinal force in the center of gravity [4], [2], [26] an aerodynamic force in downwards direction is generated. This improves the performance of the car by allowing the tires to generate higher forces, increasing vehicle acceleration limits. In [26],[2],[7],[8] this so-called downforce is modeled as follows:

$$F_d = 0.5\rho C_d A V^2 \tag{2-7}$$
$$F_l = 0.5\rho C_l A (V\cos\beta)^2 \tag{2-8}$$
$$\tag{2-9}$$

Where ρ is the air density, and C_dA and C_lA the frag and lift coefficient times the frontal area respectively. The downforce F_l is distributed over the front and rear axle in a constant ratio. Note that the drag force is assumed to be in the exact opposite direction of the velocity vector V. More sophisticated full vehicle simulation methods map the down-force, drag and distribution as function of ride height, vehicle attitude, steering angle, and yaw rate [4]. Most current MTM methods in literature ignore these effects for the sake of simplicity. However, [10] includes the influence by mapping the aerodynamic downforce and its distribution over the two axles as a function of vehicle velocity.

Since the addition of aerodynamic wheel loads introduces additional complexity, it is worth to investigate its influence on steady-state acceleration limits and stability properties to judge its added value. This is described in Section 2-3 and 2-4.

Wheel load distribution changes due to acceleration   Horizontal tire forces accelerating the vehicle are reacted in the vehicle's center of gravity. This reaction is not in the same line as the forces on the tires. As a result, a moment acts on the vehicle, which is reacted by angular accelerations of the vehicle body in roll and pitch direction and by a change in distribution of wheel loads transmitted through the suspension, referred to as load transfer [1].

In [7],[2] and [8] the body is assumed to be rigid, without the presence of an elastic suspension. As a result, the rolling and pitching moment are directly reacted by changes in wheel load distribution. The assumption of a rigid body is often justified (e.g. in [7]) by the fact that circuit driving is known to be smooth. Hence, the frequency content of the driver's control inputs is assumed low enough to not excite the suspension dynamics. This assumption is strengthened by the fact that the suspension stiffness of high downforce racing cars is designed mainly to keep the variations in ride height and pitch angle small under the entire range of downforce levels and vehicle accelerations. As a result, the natural frequencies of the sprung body in roll in pitch direction are rather high. A second consequence of the rigid model is that road irregularities cannot be taken into account in a realistic way.
To avoid the need to include extra model states related to suspension movement, and based on the statements above, it is chosen to follow the approach from [7], [2] and [8]. This results in the following equations for wheel loads:

$$0 = F_{z,fl} + F_{z,fr} + F_{z,rl} + F_{z,rr} + mg + F_l \tag{2-10}$$
$$0 = \nu(F_{z,fl} - F_{z,fr} + F_{z,rl} - F_{z,rr}) + F_y h_{\text{cg}} \tag{2-11}$$
$$0 = l(F_{z,fl} + F_{z,fr} - F_{z,rl} - F_{z,rr}) + F_x h_{\text{cg}} + mgl(d_m - 0.5) + F_l l(d_l - 0.5) \tag{2-12}$$

Where ν, l and h_{cg} denote the track width, wheel base and center of gravity height. d_m and d_l denote the weight and downforce distribution over the axles. Note that the vehicle is assumed symmetric in the $x - z$ plane, such that the center of gravity is in the middle between the left and right tires. As can be seen, this model is statically undetermined. In steady-state, some elastic and kinematic properties of the vehicle suspension define how the vertical force difference is distributed between the front and rear axle. Due to the assumption of $x - z$ symmetry, this ratio exists only in case of a lateral force, and is determined by the

term often referred to as roll moment distribution. An explanation of the terms influencing the roll moment distribution can be found in [1]. The resulting expression is:

$$F_{z,fl} - F_{z,fr} = d_{\mathrm{LT}}(F_{z,fl} - F_{z,fr} + F_{z,rl} - F_{z,rr}) \tag{2-13}$$

With $d_{\mathrm{LT}} \in [0,1]$. In Section 2-3 the influence of lateral and longitudinal load transfer on steady-state acceleration potential is shown. Furthermore, in Section 2-4 we show the influence of longitudinal load transfer on yaw dynamics.

2-2-3   Wheel dynamics

In [7], [8] and [2] four degrees of freedom are included to represent wheel rotations. The longitudinal control inputs are driving or braking torques on the wheels, with the distribution over the wheels following from the brake balance and the mechanical differential model. A free body diagram of the wheel rotational dynamics shown in Figure 2-4. The force F_x is the tire-road longitudinal force, where the torque T_w is the torque applied to the wheel, from either the brake system or the powertrain. The rotational acceleration of a single wheel is given by the following equation:

$$\dot{\omega} I_w = T_w - F_x R_L \tag{2-14}$$

Where R_L denotes the so-called loaded radius of the tire. I_w is the polar moment of inertia of the wheel. This first order system is stable if the inequality $\dfrac{\partial \dot{\omega}}{\partial \omega} < 0$ holds. The relation between F_x and ω is given by combining (2-1) and (2-3):

$$F_x = f(s_y, s_x, F_z)$$
$$s_x = \frac{\omega R_{\mathrm{eff}} - V_x}{\omega R_{\mathrm{eff}}}$$

When assuming V is constant the partial derivative $\dfrac{\partial \dot{\omega}}{\partial \omega}$ can be calculated as follows:

$$\frac{\partial \dot{\omega}}{\partial \omega} = \frac{\partial \dot{\omega}}{\partial F_x} \frac{\partial F_x}{\partial \omega} \tag{2-15}$$

$$= -R_L \frac{\partial F_x}{\partial \omega} \tag{2-16}$$

$$= -R_L \frac{\partial F_x}{\partial s_x} \frac{\partial s_x}{\partial \omega} \tag{2-17}$$

$$= -\frac{R_L}{R_{\mathrm{eff}}} \frac{V}{\omega^2} \frac{\partial F_x}{\partial s_x} \tag{2-18}$$

Since under all relevant driving conditions the first term $\frac{R_L}{R_{\mathrm{eff}}} \frac{V}{\omega^2}$ is always positive, the stability depends solely on the sign of the partial derivative $\dfrac{\partial F_x}{\partial s_x}$. That is, if the longitudinal slip of
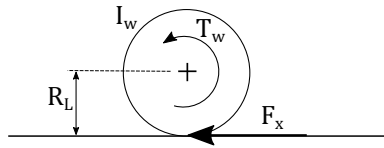
Figure 2-4: Free body diagram of wheel rotational dynamics

the tire has exceeded its slip $s_{x,M}$ for peak longitudinal force, the wheel dynamics become unstable. If this happens under negative longitudinal force, this effect is referred to as wheel lock [1]. To prevent this, modern passenger cars are equipped with ABS (Anti-lock braking system). However, in most racing categories the use of such systems is not allowed, leaving the control of longitudinal slip to the race driver. The need for avoiding wheel lock places constraints on maximum longitudinal deceleration, especially under combined lateral and negative longitudinal acceleration. The hydraulic brake system applies an equal brake torque to both wheels on an axle. Hence, if the potential for transferring longitudinal force for the two tires on an axle is unequal, the full force potential of one of the tires will not be used. The disadvantage when neglecting the wheel dynamics may be that the algorithm converges to an unrealistic solution, due to the absence of the additional bound on longitudinal deceleration.

Including the wheel rotational degree of freedom in the model has two major disadvantages. First of all, the number of states increases by four, which is a disadvantage for computational efficiency. Second, the fast wheel dynamics make that a short discretization interval is required, to limit the error in integrating the system dynamics. This again decreases computational efficiency, and possibly places bounds on the maximum problem size.

Concluding, it can be said that it is unfavorable to include the wheel rotational dynamics. To still incorporate the effect of stability, we limit the longitudinal slip of the tires to the stable region. This approach is explained in Section 3-3-3. In Section 5-2, this approach is validated by a comparison between a formulation with and without wheel dynamics.

2-2-4 Overview of modeling alternatives

In this chapter some modeling alternatives have been presented. Both the single-track and the two-track model have been shown and explained. The main difference between the two versions is that the two-track model includes the possibility of including lateral load transfer and it allows for the modeling of a mechanical differential providing a coupling between rotation of different wheels. Load transfer is assumed to have a static relation to vehicle acceleration. Furthermore, three different models of representing the mechanical differential have been shown.

In the coming sections the influence of incorporating lateral load transfer and different mechanical configurations on steady-state acceleration limits and stability is investigated. The choice between the single-track and two-track model is made based on these results. In addition, we show the influence of aerodynamic downforce and longitudinal load transfer as well.

2-3 Steady-state acceleration limits of modeling alternatives

As was stated in the introduction, minimum time maneuvering involves maximizing acceleration in the appropriate direction. Since race car driving in general is smooth, it is popular to analyze the vehicle's maximal steady-state lateral acceleration $A_{y,\text{ssmax}}$ [1]. In [1] and [3], the steady state analysis is extended to a nonzero longitudinal acceleration. Since this means that the longitudinal velocity is changing, this state cannot exist for an infinite time. However, when assuming that the longitudinal dynamics are slow compared to the other dynamics the metric provides a useful snapshot of the potential of the car on a certain instant in time.

The maximization of the lateral force provided by the two axles does not necessarily lead to a yaw moment equilibrium. Hence, for achieving a net yaw moment of zero, one of the two axles in general has to deliver a lateral force lower than the maximum possible force. We define the potential yaw moment M_{zp} as the moment around the vertical axis, that would be generated if both axles would be on their maximal lateral force. The magnitude and direction of this term can be related to control and stability of the vehicle. If M_{zp} is such that the front tires can deliver more force, the driver can still increase the path curvature off the vehicle by increasing the front wheel steering angle. If only the rear axle has unused force potential, the ability of the driver to increase yaw moment and lateral force has disappeared. On the other hand, the potential yaw moment from the rear tires has a stabilizing effect in case of disturbances, for example caused by imperfections in the road [1].

This section describes the assumptions and method for steady-state analysis. Finding $A_{y,\text{ssmax}}$ for momentary steady-state conditions involves solving a Non-Linear Programming (NLP) problem, which is described as well. Finally, the results and conclusions on desired model fidelity is presented.

2-3-1 Method and assumptions

The goal is to find the maximum steady-state lateral acceleration $A_{y,\text{ssmax}}$ for a given longitudinal acceleration. The other metric that is looked at is the potential yawing moment M_{zp} at maximum state state lateral acceleration.

The method to calculate $A_{y,\text{ssmax}}$ and M_{zp} is based on the method for generating 'g-g-speed' diagrams in [3]. The two-track model from Appendix A-3 is used. For a momentary steady-state condition, the following equations have to be satisfied:

$$\dot{V} = \frac{F_x \cos\beta + F_y \sin\beta - F_d}{m} \tag{2-19}$$

$$\dot{\beta} = \ddot{\psi} = \dot{\omega}_{fl} = \dot{\omega}_{fr} = \dot{\omega}_{rl} = \dot{\omega}_{rr} = 0 \tag{2-20}$$

Modeling details As can be seen from the equations in Appendix A-3, the two-track model contains two algebraic loops. The tire forces F_x and F_y are calculated using (2-1). Due to

the way the load transfer is modeled, the wheel loads F_z in this equation are a function of F_x and F_y. Hence, the tire forces cannot be calculated explicitly from the states.

This issue is addressed by adding an additional algebraic variable Γ_y, denoting lateral load transfer. In (A-74) - (A-77) the term $\frac{F_y h_{\mathrm{cg}}}{T}$ is then substituted by Γ_y. Finally, the relation is satisfied via an additional equality constraint:

$$\Gamma_y = \frac{F_y h_{\mathrm{cg}}}{T} \tag{2-21}$$

The total longitudinal force is already fixed by (2-19). Hence, the longitudinal load transfer is known and no additional variable needs to be included.

The distribution of drive torque T_r over the rear axle is decided by the mechanical differential. When an open differential is considered, (2-4) is used. In case of using the locked differential, (2-5) and (2-6) are used.

Optimization problem   To find the maximal steady-state acceleration, the following optimization problem is solved:

$$\max_{z} \quad F_y \tag{2-22}$$
$$\text{s.t.} \quad (2\text{-}19)$$
$$(2\text{-}20)$$
$$(2\text{-}21)$$

With $A_{y,\mathrm{ssmax}} = \frac{F_y}{m}$. The vector of optimization variables z is given by:

$$z = \begin{pmatrix} x & u & \Gamma_y \end{pmatrix}^{\top} \tag{2-23}$$

The potential yaw moment M_{zp} is found by solving the same optimization problem, without the yaw moment equilibrium constraint $\ddot{\psi} = 0$. The potential yaw moment is then calculated from this solution as:

$$M_{\mathrm{zp}} = \ddot{\psi} I_{zz} \tag{2-24}$$

Where I_{zz} denotes the yaw moment of inertia of the vehicle. Both optimization problems are solved using the Sequential Quadratic Programming (SQP) algorithm from the function `fmincon`, which is part of the MATLAB Optimization Toolbox.

2-3-2   Results steady state analysis

The parameters of the baseline vehicle are shown in Table B-1. The baseline model for all models includes lateral and longitudinal load transfer, has a locked rear differential and no aerodynamic downforce. Four comparisons are done, with the following changes to the baseline configuration:

1. Open instead of locked differential

2. Lateral load transfer is neglected

3. Longitudinal load transfer is neglected

4. Aerodynamic downforce is included

The second comparison is done both with an open and a locked differential, to map the crossplay between the two effects. For all four comparisons the influence on M_{zp} and $A_{y,\mathrm{ssmax}}$ is shown graphically. A positive value for M_{zp} indicates that the front axle is limiting for $A_{y,\mathrm{ssmax}}$, while the rear axle has some potential left. A negative value on the other hand means that the front axle has so-called unused cornering potential.

Locked versus open rear differential Figure 2-5 Shows the difference between a locked and open rear differential at three different velocities. As can be seen, the influence of torque transfer by the differential is stronger at low speeds. This has two causes. First of all, for an equal lateral acceleration, the yaw rate $\dot\psi$ is higher for a lower velocity, following from (A-38). This increases the speed difference on the left and right side of the car, following from (A-52) and (A-53). Second, the influence of a speed difference on the two sides of the vehicle has a larger influence on longitudinal slip for a low velocity, following from the same equations. Informally speaking, the radius of a turn for equal lateral acceleration is smaller for a lower speed, resulting in a relatively high speed difference between the wheels on an axle. The following can be observed from the figure:

- For $A_x > 2$ m/s^2 the open differential decreases $A_{y,\mathrm{ssmax}}$. From M_{zp} it can be seen that this is caused by a decrease in rear axle potential.

- For $A_x < 0$ the open differential increases $A_{y,\mathrm{ssmax}}$ and decreases M_{zp}, indicating that the rear axle is closer to its friction limit.

Lateral load transfer Figure 2-6 shows the influence of neglecting lateral load transfer. The result is shown a locked as well as an open differential. The velocity is 20 m/s. The following can be observed:

- For $A_x = 0$ and an open differential, $A_{y,\mathrm{ssmax}}$ is higher without lateral load transfer. This is caused by the vertical load sensitivity of the tire [1]. Although this effect is important for detailed parametric studies, it is of less relevance to the quality of the optimal control solution.

- For $|A_x| > 0$ and an open differential $A_{y,\mathrm{ssmax}}$ is increased up to about 45% when neglecting lateral load transfer.

- For $|A_x| > 0$ and a locked differential, $A_{y,\mathrm{ssmax}}$ is increased up to about 30% when neglecting lateral load transfer. Furthermore, the influence on M_{zp} is large as well, leading to a sign change for a large portion of the A_x range.
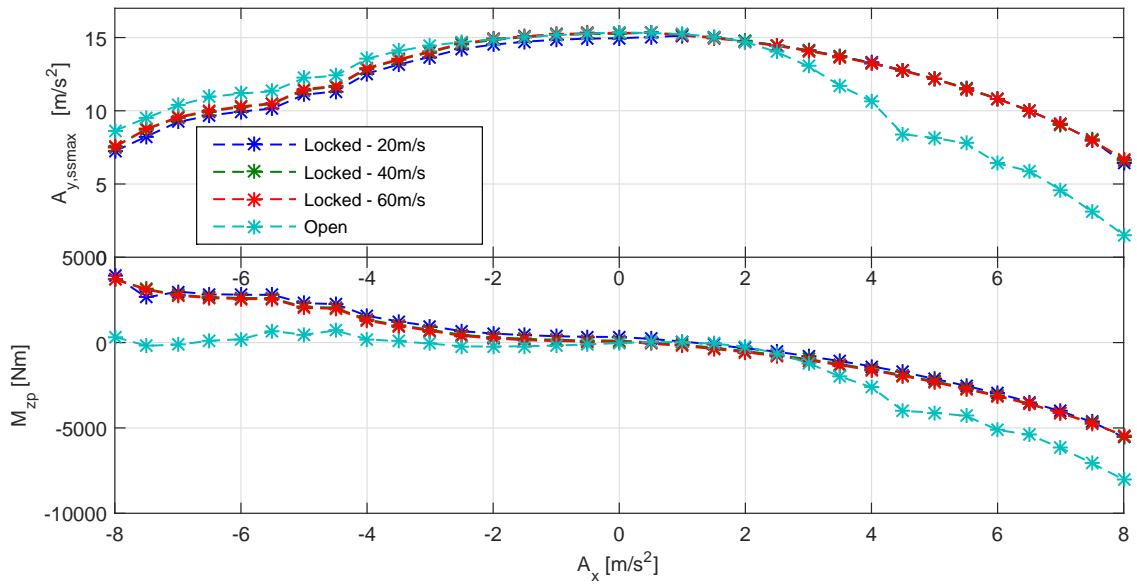
Figure 2-5: Influence of rear differential configuration on steady state characteristics
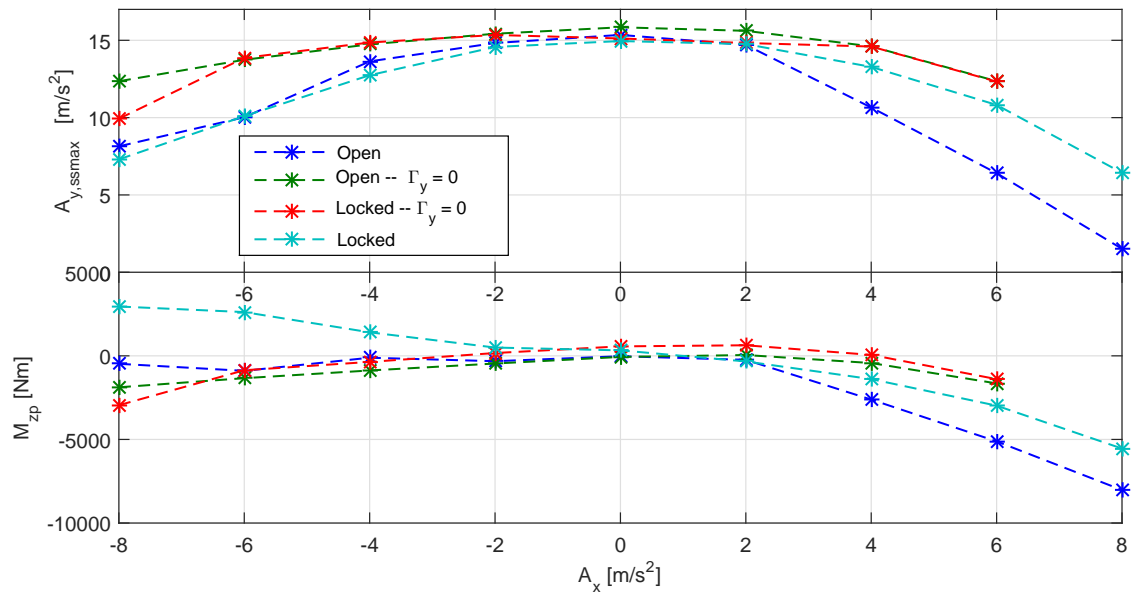
Figure 2-6: Influence of lateral load transfer on steady state characteristics
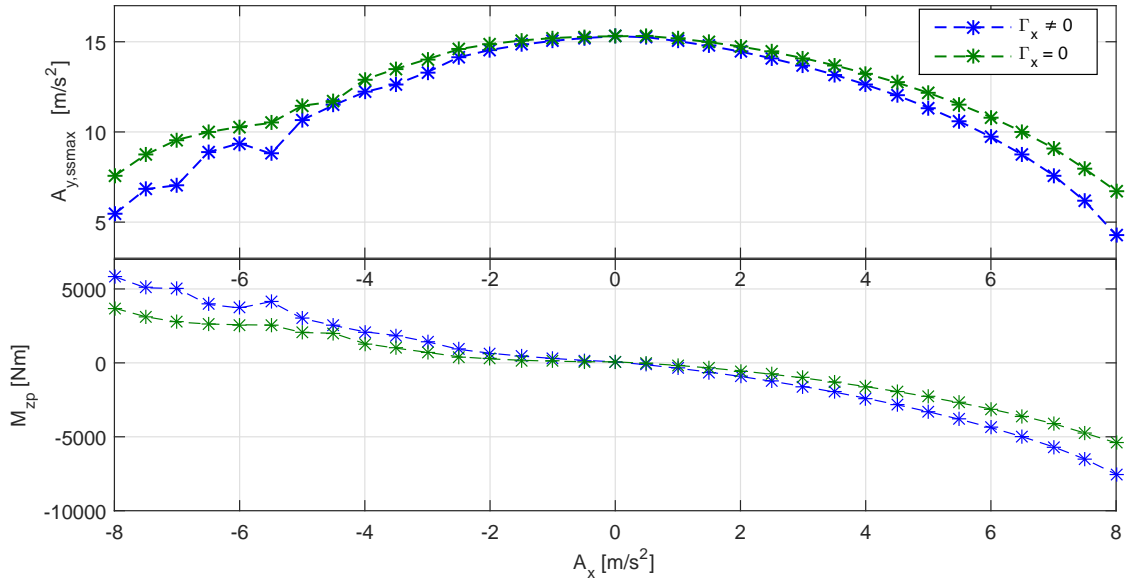
Figure 2-7: Influence of longitudinal load transfer on steady state characteristics

Longitudinal load transfer   Figure 2-7 shows the influence of neglecting longitudinal load transfer. The velocity is 50 m/s. The following differences are observed:

- For $A_x < 0$ neglecting longitudinal load transfer increases M_{zp}, and for $A_x > 0$ neglecting it decreases M_{zp}. The effect is close to proportional to A_x, and in this case causes a difference of approximately 30%.

- For all $|A_x| > 0$, neglecting longitudinal load transfer leads to a reduction in $A_{y,\text{ssmax}}$. For $A_x > 0$, this can be explained by the fact that only the rear wheels are driven. Hence, the rear axle is limiting $A_{y,\text{ssmax}}$, indicated by a negative M_{zp}. For $A_x < 0$, the combination of brake torque distribution, weight distribution and the negative yaw moment imposed by the locked differential make the front axle limiting. Transferring load to this axle under negative A_x thus increases $A_{y,\text{ssmax}}$.

Aerodynamic downforce   Figure 2-8 shows the difference in $A_{y,\text{ssmax}}$ and M_{zp} for a lift coefficient $C_l A$ of 0, 2 and 4. The velocity is again 50 m/s. The following can be observed:

- $A_{y,\text{ssmax}}$ increases substantially if aerodynamic downforce is included, which corresponds to what is known (e.g. [1]).

- M_{zp} Decreases for higher $C_l A$. This can be explained by the fact that an equal longitudinal load transfer is a smaller part of the total wheel load, due to the additional downforce. However, it should be noted that the longitudinal acceleration potential increases as well as a result of an increase in $C_l A$. A more relevant graph would have the normalized longitudinal acceleration $A_x/A_{m,\text{max}}$ as independent variable.
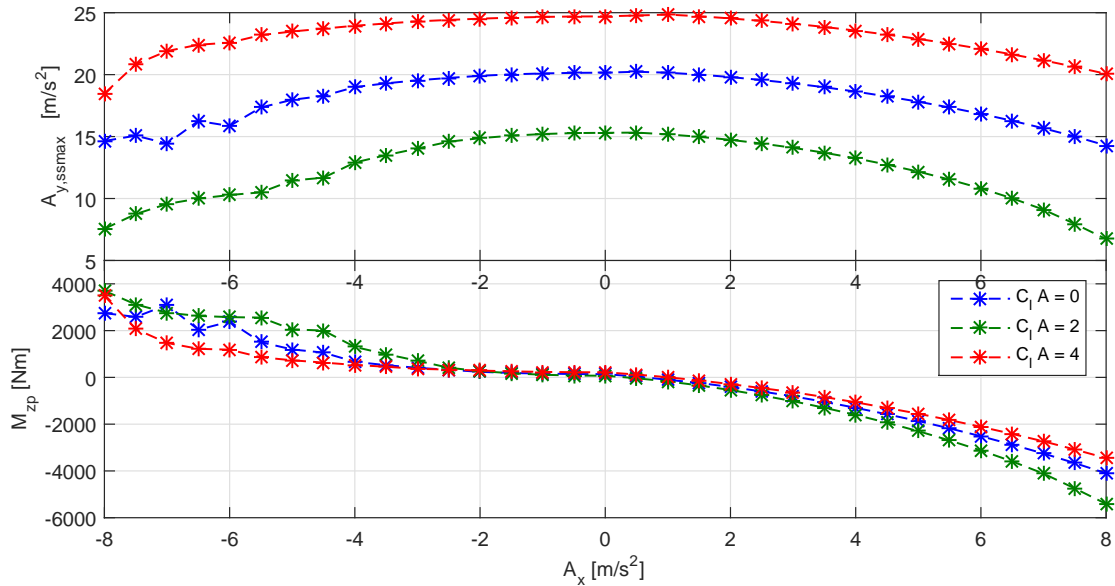
Figure 2-8: Influence of aerodynamic downforce on steady state characteristics, for a distribution over the axles of $d_L = 0.50$

2-3-3   Conclusions steady-state acceleration limit study

From the influence of the four modeling alternatives on $A_{y,\mathrm{ssmax}}$ and M_{zp}, the following can be concluded:

- A locked rear differential influences both $A_{y,\mathrm{ssmax}}$ and M_{zp} for positive A_x up to 40%. This indicates that it is important to model differential locking for positive accelerations. Furthermore, for low velocities the decrease in maximum $A_{y,\mathrm{ssmax}}$ as a result of the yawing moment of the locked differential is up to 5%. This indicates that modeling an open differential for lower $|A_x|$ is required. Hence, it can be concluded that a limited slip differential is required to achieve a realistic vehicle behavior for the entire A_x range.

- Lateral load transfer has a substantial influence on the relation between A_x and $A_{y,\mathrm{ssmax}}$. In case of a locked differential, for both negative and positive longitudinal accelerations it influences the potential yaw moment by up to 50%. Therefor, it can be expected that it has a significant qualitative influence on the optimal control solution.

- Longitudinal load transfer influences M_{zp} by approximately 30%. Furthermore, it is has a significant influence on the combined longitudinal and lateral acceleration potential for $A_x > 0$, and should therefore have a qualitative influence on the optimal input trajectory. It makes sense to include it in the model.

- Aerodynamic downforce has a large influence on the quantitative acceleration potential of the vehicle. However, the outcome of this analysis does not show a qualitative difference in the ratio of longitudinal and lateral potential of the vehicle, or the potential yaw moment. It should be noted that this outcome may change if the power limit of

the engine is included in the analysis, especially for high velocities which show a large influence of downforce on maximum A_y and aerodynamic drag on A_x.

2-4   Linearized open-loop dynamics of modeling alternatives

In addition to the analysis of steady-state acceleration potential, the influence of modeling alternatives on the vehicle dynamics is studied. This is done by comparing the eigenvalues of the linearized lateral dynamics of the vehicle at several longitudinal accelerations. The linearized lateral dynamics in state-space form are given by [1]:

$$\begin{bmatrix} \ddot{\psi} \\ \dot{\beta} \end{bmatrix} = \begin{bmatrix} a_1 & a_2 \\ \\ a_3 & a_4 \end{bmatrix} \begin{bmatrix} \dot{\psi} \\ \beta \end{bmatrix} \tag{2-25}$$

$$a_1 = \frac{1}{I_{zz}} \left(\frac{l_f^2 c_{y,f}}{V} + \frac{l_r^2 c_{y,r}}{V} \right) - c_{\text{diff},r} \tag{2-26}$$

$$a_2 = \frac{1}{I_{zz}} \left(l_f c_{y,f} - l_r c_{y,r} \right) \tag{2-27}$$

$$a_3 = -1 + \frac{1}{mV} \left(\frac{l_f c_{y,f}}{V} - \frac{l_r c_{y,r}}{V} \right) \tag{2-28}$$

$$a_4 = \frac{1}{mV} \left(c_{y,f} + c_{y,r} \right) \tag{2-29}$$

Where the state vector consists of yaw rate $\dot{\psi}$ and body slip angle β. l_f and l_r represent the distance from the center of gravity to the front and rear axle respectively, calculated from the weight distribution as follows:

$$\begin{bmatrix} l_f \\ l_r \end{bmatrix} = l \begin{bmatrix} (1 - d_w) \\ d_w \end{bmatrix} \tag{2-30}$$

Based on the assumption that the longitudinal dynamics of the vehicle are much slower than the lateral dynamics, the velocity is assumed a constant paramater [1]. Note the additional terms in a_1, representing the yaw damping as a result of a locked differential:

$$c_{\text{diff},r} = \frac{\nu^2 c_{x,r}}{2 V I_{zz}} \tag{2-31}$$

Where ν represents the track width. This effect is caused by the longitudinal velocity component of the yaw rate at wheel level, and the resulting difference on longitudinal slip. The cornering stiffness c_f and longitudinal slip stiffness c_x per axle are determined by linearization of the TMeasy tire model:

$$c_y = \frac{\partial F_y}{\partial s_y} = F(F_z, s_x, s_y) \tag{2-32}$$

$$c_x = \frac{\partial F_x}{\partial s_x} = F(F_z, s_x, s_y) \tag{2-33}$$

Note that we linearize around $s_y = 0$, since we consider straight line stability. The vertical force F_z and longitudinal force F_x are calculated using the vehicle model equations and the fixed longitudinal acceleration. The longitudinal slips $s_{x,f}$ and $s_{x,r}$ are then determined by solving the following equations:

$$(F_{x,f}, F_{y,f}) = F(s_{y,f}, s_{x,f}, F_{z,f}) \tag{2-34}$$

$$(F_{x,r}, F_{y,r}) = F(s_{y,r}, s_{x,r}, F_{z,r}) \tag{2-35}$$

$$s_{y,f} = 0 \tag{2-36}$$

$$s_{y,r} = 0 \tag{2-37}$$

Where F denotes the TMeasy tire model. Note that in general these equations may have two solutions for $s_{x,f}$ and $s_{x,r}$. However, we restrict the analysis to the stable range of the wheel dynamics, hence the lowest absolute solution for s_x is used.

The parameters for the study used are the same as in the previous Section. The effect of three different modeling alternatives on stability is judged:

- Locked versus open rear differential

- With versus without longitudinal load transfer

- With versus without aerodynamic downforce

Note that lateral load transfer is not included in the study, since we consider straight-line stability only.

Influence of locked versus open rear differential   The eigenvalues for both a locked and open differential for two different velocities are shown in Figure 2-9. It shows the longitudinal acceleration A_x on the x-axis, and the real and imaginary part of the two eigenvalues on the y-axis. The following is observed:

- For high positive and negative A_x the dominant eigenvalue moves closer to the imaginary axis. This is caused by a decrease in cornering stiffness of the tires in the presence of longitudinal force [1]. For a velocity of 60 m/s the real part even exceeds 0 at 13 m/s² braking, indicating unstable lateral dynamics.

- A higher velocity has a destabilizing effect on the yaw dynamics, indicated by the 'upwards shift' of the real part for 60 m/s. Furthermore, for modest positive longitudinal acceleration the system is oscillatory, indicated by the complex eigenvalues.

- The locked rear differential increases stability, reducing the dominant eigenvalues by about 10%.
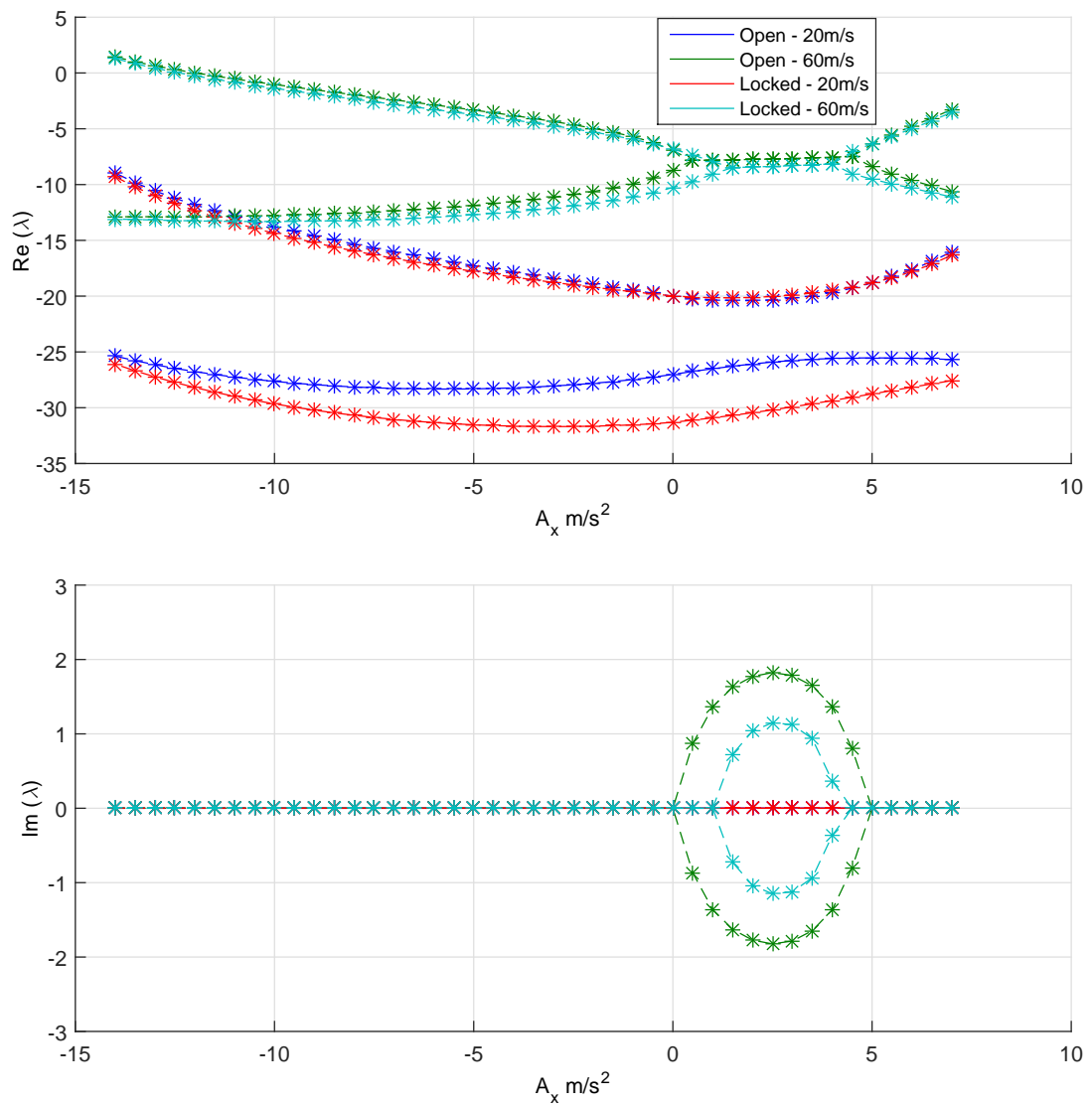
Figure 2-9: Eigenvalues of the linearized lateral dynamics for different velocities and rear differential configurations. The upper and lower graph show the real and imaginary part of the eigenvalues as a function of longitudinal acceleration respectively.

Influence of longitudinal load transfer   The influence on stability of including longitudinal load transfer is shown in Figure 2-10. The following conclusions can be drawn:

- For $A_x < 0$, including longitudinal load transfer decreases the stability, caused by the reduced cornering stiffness at the rear axle compared to the front axle [1].

- For the same reason, including longitudinal load transfer increases the stability for $A_x > 0$ significantly.

Influence of aerodynamic downforce   The influence on stability of aerodynamic downforce is shown in Figure 2-11. The main observation is that aerodynamic downforce increases the lateral stability significantly, indicated by a reduction of the real part of the dominant eigenvalue.

2-5   Final vehicle model for simulation studies

In the previous section the different modeling alternatives have been compared on their influence on steady-state acceleration limits and lateral dynamics. The analysis has shown that incorporating a two-track model is necessary, because of the large influence of load transfer and a mechanical differential on combined acceleration performance and potential yaw moment. Aerodynamic downforce is shown to have a large quantitative influence on acceleration potential, as well as on stability. Especially for comparing vehicle stability at different velocities, it is therefore important to incorporate aerodynamic downforce in the model. Longitudinal load transfer greatly influences acceleration limits as well as stability and control for combined longitudinal and lateral acceleration. The effect of lateral load transfer is less pronounced than longitudinal, but still has a significant influence on steady-state acceleration potential, especially when modeled in combination with a torque transferring mechanical differential. A locked differential appears to be a good and simple representation in case of combined longitudinal and lateral acceleration. However, it has a significant and incorrect influence on potential yaw moment for situations with low speed and low longitudinal acceleration, in practice occurring in the middle of 'low-speed' turns. As a result, it is required to incorporate a limited-slip differential to have a realistic representation throughout the longitudinal acceleration range.

The eventual vehicle model is the one described in Appendix A-3. The relation between rear axle torque T_r and rear wheel torques T_{rl} and T_{rr} is described using Coulomb friction, where the maximum torque transfer depends on engine torque, locking ratio and preload. The equations are given in Appendix A-4.

2-6   Maneuver modeling and coordinate system

The main constraints defining the maneuver are the edges of the race track. As regulations prescribe, the car should remain between the white lines marking the race track. All cur-
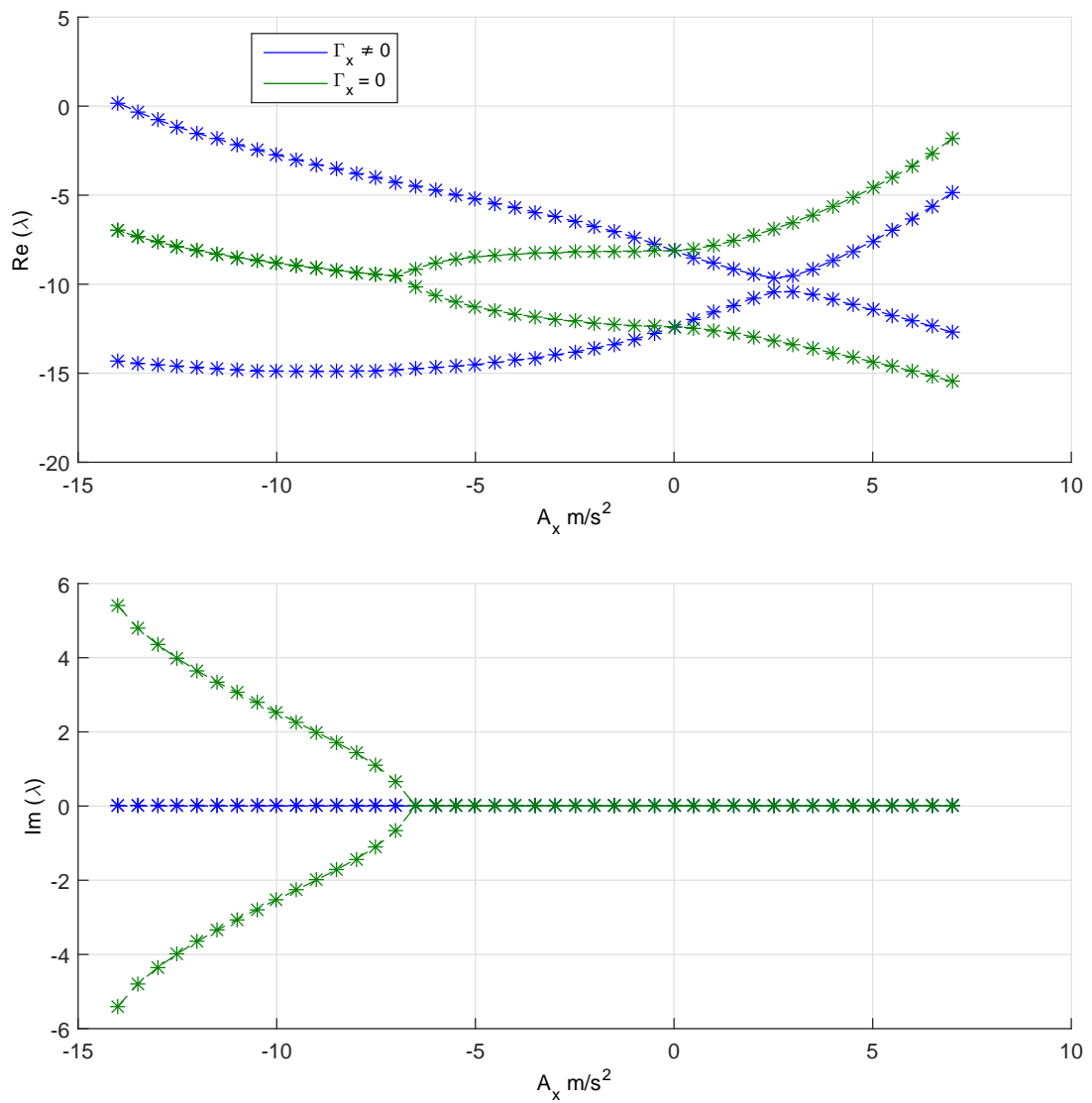
Figure 2-10: Eigenvalues of the linearized lateral dynamics with and without longitudinal load transfer. The upper and lower graph show the real and imaginary part of the eigenvalues as a function of longitudinal acceleration respectively.
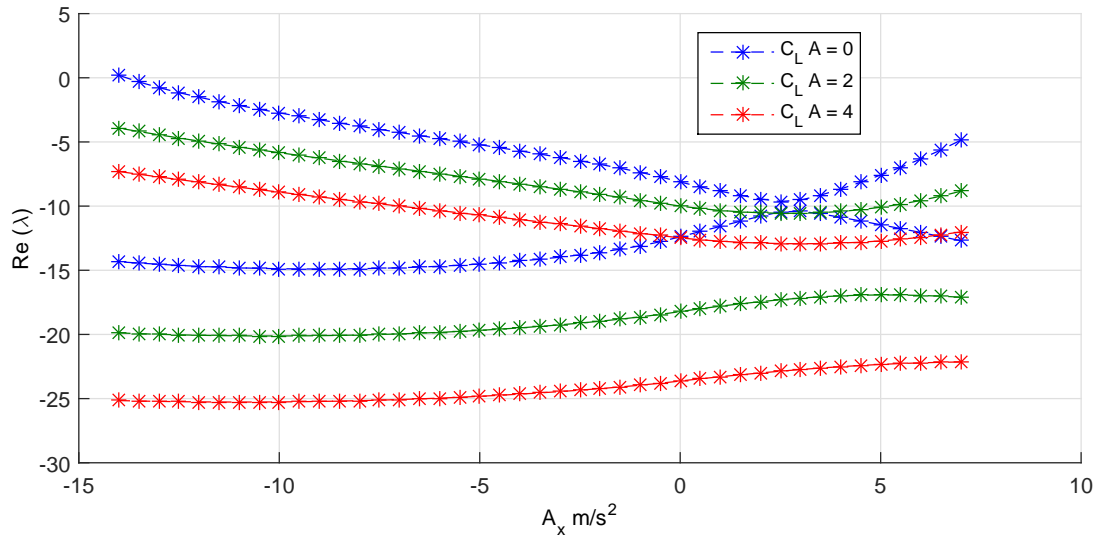
Figure 2-11: Eigenvalues of the linearized lateral dynamics for different values of lift coefficient $C_L A$. The Imaginary part is always zero

vatures of the maneuvers used in the examples of this thesis are not obtained from existing maneuvers, but are generated manually.

2-6-1 Coordinate system

Our track is defined by its start and end-line and two lines marking its edges. In [8], [2] and [17] the track is described using the center-line arc length as abscissa. The track is now defined by its curvature as a function of the center-line distance. The lines marking the edge of the track are parameterized by their distance perpendicular to the track center-line. This representation of the track is shown in Figure 2-12. The relation of curvature and radius is given by $C = 1/R$. The distance from the center-line to the track edges is given by $\mathcal{N}$.

In addition, Figure 2-12 shows the transformation of the vehicle to the track coordinate system. Instead of the Cartesian coordinates and Euler angle, the position and orientation of the vehicle are expressed as distance along center-line s, distance perpendicular to center-line n, and angle relative to center-line angle ξ. A derivation of the coordinate transformation can be found in i.e. [8], [17] or [2]. The resulting relation between local vehicle frame and global curvilinear coordinates is given by:
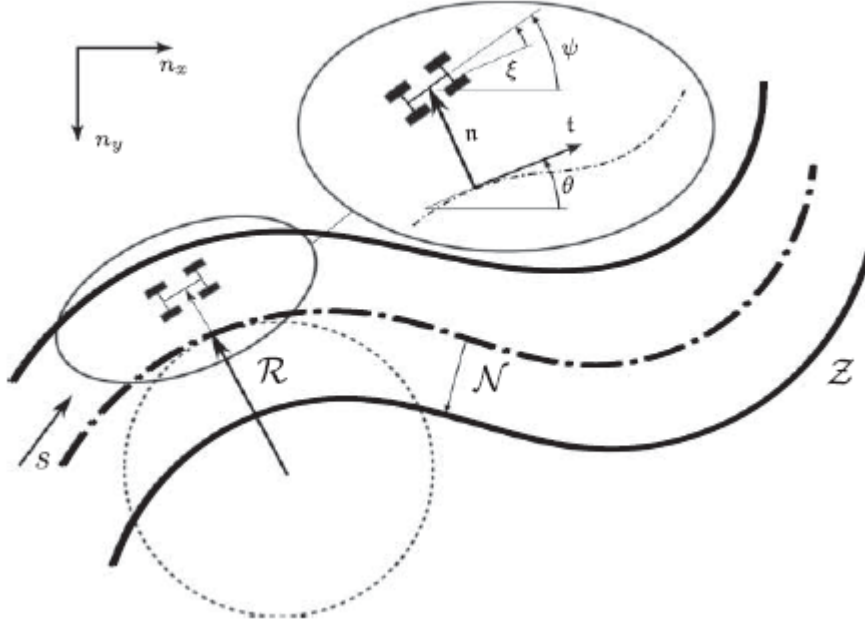
Figure 2-12: Representation of a track segment and the curvilinear coordinate transformation. Figure adopted from [8]

$$\dot{s} = \frac{v_x \cos \xi - v_y \sin \xi}{1 - nC}$$
$$= \frac{V \cos(\beta + \xi)}{1 - nC} \tag{2-38}$$
$$\dot{n} = v_x \sin \xi - v_y \cos \xi$$
$$= V \sin(\xi - \beta) \tag{2-39}$$
$$\dot{\xi} = \dot{\psi} - C\dot{s} \tag{2-40}$$

Where v_x and v_y denote the longitudinal and lateral velocity in local vehicle coordinates. The yaw rate is represented by $\dot{\psi}$. V and β denote the absolute vehicle velocity and body slip angle.

Two advantages of this system in comparison to a Cartesian coordinate system are simplicity in defining the track edges as constraints on n, as well as the possibility to define distance dependent parameters as a function of s.

2-7 Conclusion

In this chapter, the vehicle and maneuver model have been described. Different modeling alternatives have been compared on their influence on steady-state acceleration potential and lateral dynamics. Based on this it was concluded that load transfer, aerodynamic forces and a limited slip differential must be included in the vehicle model for adequate model fidelity.

It is preferable to exclude wheel dynamics from the model, because of the requirements this poses on the discretization interval. The disadvantage is the loss of information about wheel stability. This problem is addressed in Section 3-3-3. In Section 5-2 this approach is validated in a simulation study.

The maneuvers are described by a curvature-distance profile. The edge of the track is described in by its perpendicular distance to the center-line. The global coordinate system for the system dynamics is related to the maneuver description. The coordinates for describing the position and orientation in the 2D-plane are distance along center-line s, distance perpendicular to center-line n and angle relative to center-line angle ξ.

In the upcoming chapter the described model will be used for the formulation of the race car MTM problem as an optimal control problem. The system dynamics will be shaped in the form of constraints. Furthermore, all non-smooth aspects of the model will be approximated by a smooth alternative, which is required for applying a numerical optimization method for solving the optimal control problem.

Chapter 3

Formulation of the optimal control problem

The main function of a race car driver is to deliver the control inputs which drive the race car around the track. The driver is aiming to minimize his maneuver time, and in doing so approaches the bounds of the race tracks and the limitations the vehicle's dynamics. The three main control inputs for the driver are the steering wheel, accelerator and brake pedal. Strictly speaking, the set of control inputs also includes the gear selection, the clutch pedal and even settings in the engine and vehicle control systems. Aside from this the driver may be assisted by control systems, such as traction control which directly influences the engine torque delivered to the driven wheels. In this thesis we assume only two control inputs, which are a steering wheel angle and a longitudinal control input. The longitudinal control input can be either torque applied to the driven wheels, or a braking torque applied to all wheels. Note that this assumes that the throttle and brake pedal are never actuated at the same time. Practical experience with high-downforce racing cars shows that this is indeed the case.

In this chapter a formal formulation for the race car Minimal Time Maneuvering (MTM) problem as an Optimal Control Problem (OCP) is presented. In Section 3-2 the transformation of independent variable from time to distance along track center-line is given. Afterwards, the performance index is formulated, and the system dynamics and maneuver limitations are transformed into equality and inequality constraints. Two different versions of the system dynamics are described, of which the solution is compared in Chapter 5. The first does not incorporate wheel rotational dynamics, and takes the longitudinal tire slips as control inputs. In the second formulation the wheel rotational velocities are included as states, and control input is linked to the wheel torque. Finally, in Section 3-7 the definitions are summarized and formed into the optimal control problem formulation.

3-1   Generic optimal control problem formulation

The objective in race car MTM is to find the control inputs minimizing the time needed to travel from one point to another. In doing this, the driver aims to operate on the boundaries of the dynamics of the vehicle. This includes actuator limits, such as the maximum power that can be delivered by the powertrain or a maximum steering angle of the front wheels, as well as physical limitations incorporated in the vehicle model, such as the maximum transmittable tire force. In addition, the vehicle has to stay within the edges of the track.
What is phrased above in words, can be formulated as a generic optimal control problem:

$$\min_{u} \quad T_m = \int_{t_0}^{t_F} dt \tag{3-1}$$

$$\text{s.t.} \quad \frac{dx}{dt} = f(x(t), u(t)) \tag{3-2}$$

$$g(x(t), u(t)) \leq 0 \tag{3-3}$$

$$q(x(t), u(t)) = 0 \tag{3-4}$$

$$u_L \leq u(t) \leq u_U \tag{3-5}$$

$$\tag{3-6}$$

The problem is defined for $t_0 \leq t \leq t_F$, where maneuver time T_m is the only variable in the performance index. The nonlinear inequality and equality constraints $g(x(t), u(t)) \leq 0$ and $q(x(t), u(t)) = 0$ include the track boundaries and system limitations. The independent variable transformation, the system dynamics and g and q are specified in the coming sections.

3-2   Performance index and transformation to spatial dynamics

The conventional independent variable for simulating dynamics is time. The race car MTM problem however is parameterized mainly in terms of position. That is, maneuver start and end, lane curvature, lane width and other effects can be expressed directly in terms of center-line distance. Furthermore, we assume that no parameters are directly influenced by time. This motivates using distance along track center-line s as independent variable. By doing this, s can be removed from the state vector, reducing the problem size. Note that this transformation is allowed if a unique relation between s and t can be found, which is the case if the vehicle only travels in positive s direction. The transformation was applied in [17], [20], [8] and [7] as well. The conversion factor for the transformation is the inverse speed along the center-line from (2-38):

$$S_f = \left(\frac{ds}{dt}\right)^{-1} = \frac{1 - nC}{V \cos(\beta + \xi)} \tag{3-7}$$

The spatial dependent dynamics are now simply obtained by dividing the dynamic equations by $\dot{s}$, hence:

$$\frac{dx}{ds} = S_f \frac{dx}{dt} = f(x(s), u(s), C(s)) \tag{3-8}$$

The performance index can then be calculated as follows:

$$J = \int_{t_0}^{t_F} dt = \int_{s_0}^{s_F} \frac{dt}{ds}ds = \int_{s_0}^{s_F} S_f ds \tag{3-9}$$

Where $s_0 = s(t_0)$ and $s_F = s(t_F)$ are the distance at the start and end of the maneuver respectively.

3-3   System dynamics

The vehicle model was described in Chapter 2. An overview of the modeled states and control inputs is given in Table 3-1. The time derivatives for x_3, x_4 and x_5 are described in Appendix A-3. These are transformed to distance derivatives $\frac{dx}{ds}$ using (3-8). The distance derivatives for x_1 and x_2 are derived from (2-39) and (2-40):

$$\begin{aligned}
\frac{dn}{ds} &= S_f \dot{n} \\
&= S_f V \sin(\xi - \beta) \tag{3-10} \\
\frac{d\xi}{ds} &= S_f \dot{\xi} \\
&= S_f(\dot{\psi} - C\dot{s}) \\
&= S_f \dot{\psi} - C \tag{3-11}
\end{aligned}$$

Where C is the curvature of the center-line and S_f the time-to-distance scaling factor given by (3-7).

As described in Chapter 2 the wheel dynamics are not included in the formulation. The variables representing longitudinal control are the longitudinal slip s_x at each wheel. As stated in the introduction we assume only one degree of freedom defining the longitudinal control input. In accordance with this assumption, in Section 3-3-2 we define three additional independent equality constraints on the longitudinal force distribution. These constraints represent the hydraulic brake system and mechanical differential. Furthermore, it can be seen that longitudinal and lateral load transfer Γ_x and Γ_y are incorporated as control inputs. In Section 3-3-1 this will be explained.

3-3-1   Wheel load distribution

As was already mentioned in Section 2-3-1, the model includes two algebraic loops. That is, the wheel load distribution cannot be calculated directly from the states, but has to be solved instead. Substituting the control inputs for load transfer in Equations (A-74) to (A-77) results in the following equations for the wheel loads:

Table 3-1: Overview of the states and control inputs

	Type	Name	Physical symbol	unit
u_1	control input	steering angle	δ	rad
u_2	control input	longitudinal slip front left	$s_{x,fl}$	-
u_3	control input	longitudinal slip front right	$s_{x,fr}$	-
u_4	control input	longitudinal slip rear left	$s_{x,rl}$	-
u_5	control input	longitudinal slip rear right	$s_{x,rr}$	-
u_6	control input	normalized longitudinal load transfer	Γ_x	-
u_7	control input	normalized lateral load transfer	Γ_y	-
x_1	state	Distance perpendicular to center line	n	m
x_2	state	Angle relative to center line angle	ξ	rad
x_3	state	Velocity	V	m/s
x_4	state	Body slip angle	β	rad
x_5	state	Yaw rate	$\dot{\psi}$	rad/s

$$F_{z,fl} = \frac{1}{2}mgd_m - \Gamma_x\frac{1}{2} + \Gamma_y d_{\mathrm{LT}} + \frac{1}{2}F_l d_l \tag{3-12}$$

$$F_{z,fr} = \frac{1}{2}mgd_m - \Gamma_x\frac{1}{2} - \Gamma_y d_{\mathrm{LT}} + \frac{1}{2}F_l d_l \tag{3-13}$$

$$F_{z,rl} = \frac{1}{2}mg(1-d_m) + \Gamma_x\frac{1}{2} + \Gamma_y(1-d_{\mathrm{LT}}) + \frac{1}{2}F_l(1-d_l) \tag{3-14}$$

$$F_{z,rr} = \frac{1}{2}mg(1-d_m) + \Gamma_x\frac{1}{2} - \Gamma_y(1-d_{\mathrm{LT}}) + \frac{1}{2}F_l(1-d_l) \tag{3-15}$$

Where m denotes vehicle mass. The weight, aerodynamic downforce and lateral load transfer are distributed over the axles by d_m, d_l and d_{LT}. Note that the longitudinal and lateral load transfer Γ_x and Γ_y are normalized by the vehicle weight mg, which has been done for scaling purposes. Relations (3-12) to (3-15) are satisfied by the following equality constraints, applied to the entire maneuver:

$$q_1 = \frac{F_x h_{\mathrm{cg}}}{lmg} - \Gamma_x = 0 \tag{3-16}$$

$$q_2 = \frac{F_y h_{\mathrm{cg}}}{\nu mg} - \Gamma_y = 0 \tag{3-17}$$

Where l, ν and h_{cg} denote the wheel base, track width and center of gravity height respectively.

3-3-2   Wheel torque distribution

The distribution of torque over the four wheels has to satisfy the following conditions:

- Positive torque is only exerted by the rear axle.

- Negative torque exerted by the brake system is distributed over the two axles by a constant brake balance d_T.

- The engine exerts a drag power to the rear axle, which should be excluded from the brake balance calculation.

- The torque at the front left tire and front right tire is equal, as dictated by the hydraulic brake system

- The distribution of torque between the rear left and rear right tire is dictated by the model of the mechanical differential, of which the friction characteristics depend on the engine torque.

With the introduction of longitudinal slips s_x as inputs, these conditions are not automatically applied through the equations of motion. Instead, we satisfy them through the following equality constraints:

$$q_3 = T_{fl} - T_{fr} = 0 \tag{3-18}$$

$$q_4 = \Delta T_d - (T_{rl} - T_{rr}) = 0 \tag{3-19}$$

$$q_5 = \begin{cases} T_f - (T_f + T_r - T_{\mathrm{E,drg}})d_T = 0 & \text{if} \quad T_f \geqslant 0 \\ T_f = 0 & \text{otherwise} \end{cases} \tag{3-20}$$

Note that the brake balance and rear wheel drive constraint are combined in (3-20). Furthermore, the engine drag torque is excluded from the brake balance calculation. The relevant torques can be calculated easily when neglecting the wheel dynamics in (2-14):

$$T_i = F_{x,i} R_L \tag{3-21}$$

For $i = fl, fr, rl, rr$. The maximum possible torque that can be transferred by the differential T_d is given by (A-83) and (A-83). As the wheel rotational velocities are not part of the state vector any more, they are calculated from the longitudinal slips s_x using (2-3). The engine torque acting on the mechanical differential is calculated using relation (A-85).

Powertrain limitations The maximum torque provided to the rear axle is limited by the power of the powertrain. We neglect the effects of changing gears, hence the powertrain is assumed to have an equal power for the entire velocity range. The corresponding constraint is formulated as:

$$g_1 = T_E \frac{\omega_{rl} + \omega_{rr}}{2} \leq P_E \tag{3-22}$$

Where P_E denotes the constant maximum engine power.

3-3-3   Constraints on wheel dynamics representing stability boundaries

As described in Section 2-2-3, stability of the wheel dynamics is decided by the factor $\dfrac{\partial F_x}{\partial s_x}$. Although wheel rotational velocity is not included in the problem formulation, we still want to prevent the driver from exploiting the control inputs in a way that would lead to unstable wheel dynamics (lock) in a realistic situation. Therefore, the following inequality constraints are included to the problem formulation:

$$g_2 = -\frac{\partial F_{x,fl}}{\partial s_{x,fl}} \leq 0 \tag{3-23}$$

$$g_3 = -\frac{\partial F_{x,fr}}{\partial s_{x,fr}} \leq 0 \tag{3-24}$$

As can be seen the constraints are only applied to the front wheels. On the rear axle, the expression for stability is more complex, due to the coupling between the two wheels by the mechanical differential. However, due to this coupling the tendency of the optimal control solution to misuse this effect is smaller. Therefore, we focus solely on the front axle in this thesis.

3-4   Alternative formulation of system dynamics including wheel rotational velocity

As a reference for validation of the choice to neglect wheel dynamics (5-2), a representation of the system dynamics including wheel dynamics is given here. The constraints are:

$$q_1 = \frac{F_x h}{lmg} - \Gamma_x = 0 \tag{3-25}$$

$$q_2 = \frac{F_y h}{\nu mg} - \Gamma_y = 0 \tag{3-26}$$

$$g_1 = T_E \frac{\omega_{rl} + \omega_{rr}}{2} \leq P_E \tag{3-27}$$

Constraints q_3, q_4 and q_5 from the original formulation have been dropped, since they are satisfied implicitly by the equations of motion. The wheel stability constraints g_2 and g_3 are superfluous for this model, because the actual dynamics are included.

3-5   Maneuver boundaries and initial conditions

In addition to the constraints defining the limitations of the vehicle, the path is limited by the edges of the race track. In reality, the position of the vehicle might be bounded at a certain instant by the position of its one of its tires, or by contact between its bodywork

Table 3-2: Overview of the states and control inputs for formulation including wheel speeds

	Type	Name	Physical symbol	unit
u_1	control input	steering angle	δ	rad
u_2	control input	total wheel torque	T	Nm
u_3	control input	longitudinal load transfer	Γ_x	-
u_4	control input	lateral load transfer	Γ_y	-
x_1	state	Distance perpendicular to center line	n	m
x_2	state	Angle relative to center line angle	ξ	rad
x_3	state	Velocity	V	m/s
x_4	state	Body slip angle	β	rad
x_5	state	Yaw rate	$\dot{\psi}$	rad/s
x_6	state	relative wheel speed front left	Vw, rel, fl	-
x_7	state	relative wheel speed front right	Vw, rel, fr	-
x_8	state	relative wheel speed rear left	Vw, rel, rl	-
x_9	state	relative wheel speed rear right	Vw, rel, rr	-

and walls marking the track edge. For the sake of simplicity, we apply the bound to the center of gravity of the vehicle, rather than incorporating complex geometrical relations. With the introduction of the curvilinear coordinate system, these bounds reduce to the linear constraints on the distance perpendicular to the center-line n:

$$\mathcal{N}_l(s) < n(s) < \mathcal{N}_r(s) \tag{3-28}$$

Where $\mathcal{N}_l(s)$ and $\mathcal{N}_r(s)$ denote the distance dependent maximum offset from the center-line. Finally, the initial condition of the vehicle is defined as:

$$x(s_0) = x_0 \tag{3-29}$$

3-6   Smoothing functions

(3-20), (A-83), and (A-85) have a discontinuous character. We solve the race car MTM problem using a Non-Linear Programming (NLP) method, which assumes continuous and differentiable objective functions. When presenting discontinuities, the linear and quadratic models used by NLP methods are no longer appropriate [27]. Moreover, if a discontinuity is present close to the solution, the Karush-Kuhn-Tucker (KKT) necessary conditions for optimality do not apply. To address this issue, we approximate non-smooth model characteristics by at least twice differentiable functions. (A-83), describing the torque transfer from the left to right wheel by the mechanical differential is approximated by the following function:

$$\Delta T_d = \frac{2}{\pi} \arctan(\eta_1(\omega_{rl} - \omega_{rr}))T_{d,\max} \tag{3-30}$$

Where η_1 is the parameter deciding the smoothness of the approximation. Note that with this approximation the model of the differential becomes equivalent to the one used in [7],
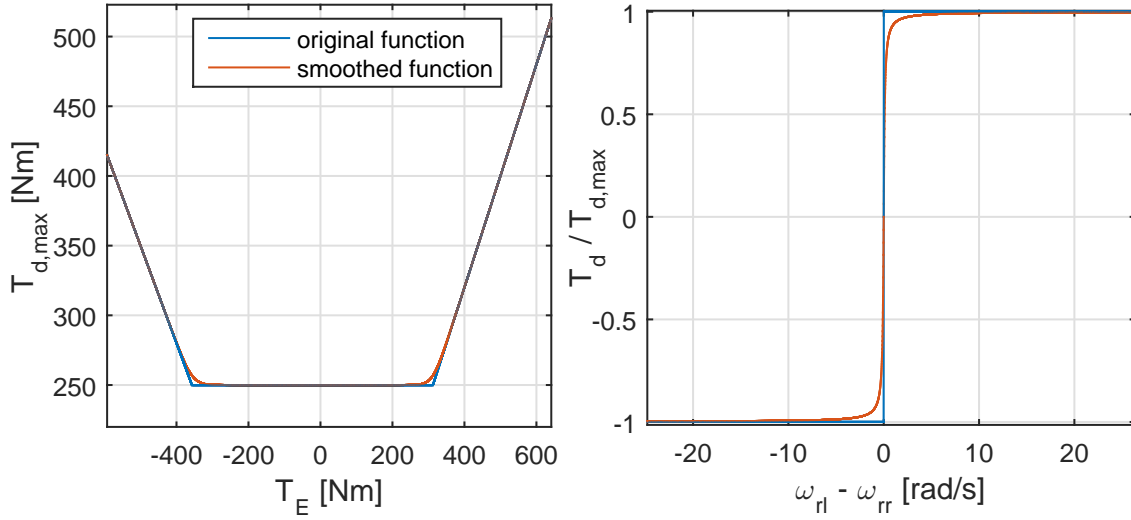
Figure 3-1: Graphical representation of smoothed mechanical differential characteristics.
$\eta_1 = 10$, $\eta_4 = 0.1$, $T_0 = 250$, $G_{\text{drv}} = 0.8$, $G_{\text{brk}} = 0.7$

featuring a viscous part. A graphical representation is shown in Figure 3-1. (3-20) and (A-85) are approximated by an arctan function as well:

$$q_5 = T_f - (T_f + T_r - T_{\text{E,drg}})d_T\left(\frac{\arctan(-\eta_2 T_f)}{\pi} + 1\right) \tag{3-31}$$

$$T_E = \sum T\left(\frac{\arctan(\eta_3(\sum T - T_{\text{E,drg}}))}{\pi} + 1\right) - T_{\text{E,drg}} \tag{3-32}$$

The max function in (A-84) is replaced by a smooth alternative, resulting in:

$$T_{d,\max} = \frac{\ln(e^{\eta_4 G_{\text{drv}} T_E} + e^{\eta_4 T_0} + e^{-\eta_4 G_{\text{brk}} T_E})}{\eta_4} \tag{3-33}$$

The graphical representation of this is shown in Figure 3-1 as well.

3-7   Final optimal control problem formulation

The description of the performance index and the constraints representing the system dynamics and maneuver boundaries can be combined in the following optimal control problem:

$$\min_{u} \quad J = \int_{s_0}^{s_F} \frac{1 - n(s)C(s)}{V(s)\cos(\beta + \xi)} ds \tag{3-34}$$

$$\text{s.t.} \quad \frac{dx}{ds} = f(x(s), u(s)) \tag{3-35}$$

$$
\begin{aligned}
x(s_0) &= x_0 \\
q_1(s) &= 0 \\
q_2(s) &= 0 \\
q_3(s) &= 0 \\
q_4(s) &= 0 \\
q_5(s) &= 0 \\
g_1(s) &\leq 0 \\
g_2(s) &\leq 0 \\
g_3(s) &\leq 0 \\
u_L \leq \quad u(s) &\leq \quad u_U \\
\mathcal{N}_l(s) < \quad n(s) &< \quad \mathcal{N}_r(s)
\end{aligned}
\tag{3-36}
$$

Where $f : \mathbb{R}^n \times \mathbb{R}^m \longrightarrow \mathbb{R}^n$. The state vector x and input vector u are given by:

$$x = \begin{pmatrix} n & \xi & V & \beta & \dot{\psi} \end{pmatrix}^\top \tag{3-37}$$

$$u = \begin{pmatrix} \delta & s_{x,fl} & s_{x,fr} & s_{x,rl} & s_{x,rr} & \Gamma_x & \Gamma_y \end{pmatrix}^\top \tag{3-38}$$

The alternative formulation including wheel rotational velocities can be composed in the same manner, using the description of Section 3-4.

3-8 Conclusion

In this Section the race car MTM was formulated as an OCP. The transformation of time to distance along the track's center-line as independent variable is described. The system dynamics are incorporated as equality constraints for the problem. The control inputs corresponding to the brake and throttle pedal are longitudinal tire slips. Algebraic constraints representing wheel torque distribution properties are included, resulting in only one degree of freedom for the longitudinal control input. Wheel load distribution changes due to vehicle planar accelerations are incorporated as well, by including two additional states and algebraic equality constraints. We have included inequality constraints that bound the derivative of longitudinal force to longitudinal slip on the front tires individually. This constraint is used to incorporate the effect that wheel dynamics have on the admissible longitudinal control input. The track limitations are incorporated as simple bounds on the lateral position. As a reference for the validation in Chapter 5, an additional formulation including wheel rotational velocities was given.

In the next chapter the optimal control problem will be transcribed into an NLP problem, using direct collocation. Furthermore, two different solvers are compared on their suitability for this OCP.

Chapter 4

Direct collocation and solution using NLP

In the previous chapter the race car Minimal Time Maneuvering (MTM) problem was formulated as an optimal control problem. For solving such problems, a large body of literature is available [27], [28]. The two main strategies available are the so-called direct and indirect method. The indirect method makes use of Pontryagin's minimum principle, which states that optimal control corresponds to the admissible control inputs that minimize the Hamiltonian. Subsequently, these conditions are solved directly by minimizing the Hamiltonian.

The method is known to have a superior accuracy [28] but literature also reports some important drawbacks. First of all, deriving the necessary conditions for optimality may be difficult and impractical. Second, solving using the indirect method requires a relatively close initial guess of the trajectory of the controls, adjoint variables and active set at the optimum. This requires sufficient knowledge of the problem to be optimized and hurts flexibility in the problem setup. Furthermore, giving an estimate of the active set along the trajectory may be difficult in the presence of many differential and algebraic inequality constraints. For the race car MTM, using the indirect method would imply that an estimate is needed for which sections are constrained by track boundaries. A similar estimate will be needed to identify the arcs on which the power and wheel stability constraints are active. This would be difficult, and furthermore the complexity of the problem formulation in Section 3-7 does not encourage the derivation of the necessary conditions for optimality.

Alternatively, the direct method is based on a discretization of the problem, resulting in a finite number of optimization variables. The cost function is minimized directly by a suitable Non-Linear Programming (NLP) method. A large body of literature exists for discretizing the problem into an NLP, and the availability of many NLP solvers makes the direct method often preferred over the indirect method [27],[28].

In this work, we solve the Optimal Control Problem (OCP) using the direct method. For transcribing the problem into an NLP, the direct collocation approach is employed. This approach is described in Section 4-1. Section 4-3 describes the parameterization of the state and control input trajectories in terms of B-splines, of which the coefficients are presented to the NLP solver as decision variables. The scaling of optimization variables, cost function and constraint functions is important for the convergence of the problem, and is described in Section 4-7.

For solving the resulting large-scale NLP, two solvers are considered. The first one is the open-source interior-point solver IPOPT. The second one is the Sequential Quadratic Programming (SQP)-based solver SNOPT. The two solvers are compared in a simulation study. Furthermore, Section 4-8-2 presents an accuracy study, used to determine a suitable discretization interval.

4-1   Discretization and direct collocation

For transcribing the optimal control problem into an NLP problem several transcription methods exist. Two main directions are direct shooting and full collocation. In direct shooting, the control history $u(s)$ is discretized into a finite number of variables $(u_1, u_2, ..., u_n)$. The performance index and constraints are calculated by propagating through the differential equations. Since only the control inputs are considered as optimization variables, this approach results in relatively small-scale problems. The disadvantage however is the chance of numerical difficulties for the applied solver, as a result of the large difference in sensitivity to early and late controls. This effect is even stronger for nonlinear and unstable systems. Multiple shooting methods address this problem by dividing the problem in multiple shooting segments. Each segment is treated as a direct shooting segment, and the segments are connected by defect constraints. As such, the problem is partially decoupled, leading to better conditioning of Jacobian.

In the full collocation approach, the shooting segment has exactly the length of one discretization interval. Since the states at each segment are connected, this means that not only the control inputs, but also the discretized state trajectory $(x_1, x_2, ..., x_n)$ is included in the set of decision variables. The dynamics of the system are satisfied by residual constraints, connecting the discretization intervals by a certain integration rule. The full collocation approach leads to maximal decoupling. Although the resulting problems are large, the Jacobian is therefore very sparse as well. This allows for making use of existing NLP Solvers with the ability to handle large-sparse problems very efficiently. Furthermore, gradient information required for the NLP can be calculated efficiently if sparsity information is used [27].

Although there is no ever-working flow-chart for choosing one or the other method, some general rules are described in [28],[19]. Problems with a moderate number of states in the dynamics but a high number of discretization intervals and very nonlinear dynamics are often transcribed using full collocation. Typically, shooting methods are used for problems with a high amount of states, since applying full collocation simply would lead to a too large problem. Since the race car MTM has strong nonlinear and possibly unstable characteristics (2-4), in this work the full collocation approach is used.

As described in the previous section, the independent variable is distance along the track center-line. The distance interval $[s_0 \quad s_F]$ is divided into N parts: $s_0 = s[1] < ... < s[N] = s_F$. The discretization interval $h[i]$ for $i = 1 \quad ... \quad N - 1$ is given by:

$$h[i] = s[i + 1] - s[i] \tag{4-1}$$

Where $h[i]$ is not necessarily equal for all i. The path constraints are satisfied on each of discretization points:

$$\tilde{q} = (q[1] \quad \cdots \quad q[N]) = 0 \tag{4-2}$$
$$\tilde{g} = (g[1] \quad \cdots \quad g[N]) \leq 0 \tag{4-3}$$

Where $\tilde{q} \in \mathbb{R}^w$ and $\tilde{g} \in \mathbb{R}^v$ denote the augmented constraint vectors, with w and v the number of equality and inequality constraints respectively, as defined in Equation (3-35). The initial condition constraint (3-29) is transformed into an NLP constraint as follows:

$$\Upsilon = x[1] - x_0 = 0 \qquad\qquad x_o \in \mathbb{R}^n \tag{4-4}$$

The inequality constraints representing the maneuver boundaries (3-28) are represented as follows:

$$\tilde{b}_l \quad < \quad \tilde{n} \quad < \quad \tilde{b}_r \tag{4-5}$$

Where the distance-dependent maximum center-line offset to the left and right side $\tilde{b}_l$ and $\tilde{b}_r$, and the center-line distance $\tilde{n}$ along the maneuver are defined as:

$$\tilde{n} = (n[1] \quad \cdots \quad n[N])^\top$$
$$\tilde{b}_l = (b_l[1] \quad \cdots \quad b_l[N])^\top$$
$$\tilde{b}_r = (b_r[1] \quad \cdots \quad b_r[N])^\top$$

4-2 Quadrature method and residual constraints

When using the full collocation method, the system dynamics from Equation (3-35) are represented by a set of collocation defects, brought to below a certain tolerance by the NLP method. The exact formulation of the constraint depends on the quadrature rule used. The general form (adopted from [29]) is:

$$\int_{s_0}^{s_F} g(s)ds = \sum_{i=0}^{N} \mu_i g(s[i]) \tag{4-6}$$

Where the weights μ_i and these collocation points are determined in advance. In this thesis we will implement the trapezoidal method. The collocation defects for the trapezoidal method are given by:

$$\Phi[i] = x[i+1] - x[i] - \frac{h[i]}{2}(x'[i] + x'[i+1]) \tag{4-7}$$

For $i = 1 \dots N - 1$. The required discretization interval is found in Section 4-8-2 by looking at the influence of sampling rate on maneuver time and state and input trajectory.

4-3 Representation of optimization variables in terms of B-spline coefficients

In order to be able to impose certain smoothness criteria to the state and input trajectory, we represent them by B-splines. Furthermore, it is known that the application of B-splines can prevent oscillatory solutions on constraint arcs [30]. For the implementation the methodology described in [29] was followed. We start with a short introduction to B-splines, after which the implementation in the optimal control context is described.

The interpolated curve for a single output $z(t)$ is given by:

$$z = \sum_{i=1}^{n} B_{i,k}(t)C_i \tag{4-8}$$

$$n = l(k - m) + m \tag{4-9}$$

$$B_{i,0} = \begin{cases} 1 & \text{if} \quad t_i \leq t < t_{i+1} \\ 0 & \text{otherwise} \end{cases} \tag{4-10}$$

$$B_{i,k}(t) = \frac{t - t_i}{t_{i+k+1} - t_i}B_{i,k-1}(t) + \frac{t_{i+k} - t}{t_{i+k} - ti + 1}B_{i+1,k-1}(t) \tag{4-11}$$

The splines are constructed by joining Bezier curves together. A characteristic for these curves is that they have a user defined order k. The curves are glued together on breakpoints, of which the smoothness is defined by the difference between the order k and the multiplicity m of breakpoints per coefficient C_i. The functions $B_{i,k}(t)$ are connected by the recursion formula (4-11). Finally, the variables defining the curve with given order and multiplicity are the coefficients C_i, called control points. In case of representing optimal input and state trajectories using B-splines, these control points are the decision variables for the optimization.

An important property is that the smoothness of the curves can be defined by parameters m and k, making the spline $C^{k_i - m_i - 1}$ times continuously differentiable. Furthermore, it can be seen that outside the interval $[t_i, t_{i+k}]$ the basis function $B_{i,k}$ is zero, which is referred to as the local support property. In case of application to optimal control problem with direct collocation this preserves Jacobian sparsity.

4-3-1 Implementation of B-splines

As described in Section 4-1, the discretization points are defined by $s_0 = s[1] < ... < s[N] = s_F$. The path constraints and residuals related to integration errors are evaluated on these collocation points for $x[i]$ and $u[i]$. These points form the collocation points for the B-spline curves. The value of $x[i]$ and $u[i]$ at these points depend linearly on the spline coefficients as follows:

$$x_j = L_x c_{x,j} \tag{4-12}$$
$$u_w = L_u c_{u,w} \tag{4-13}$$

For $j = 1, ..., n$ and $w = 1, ..., o$, with n and o the number of states and inputs of the system respectively. L_x and L_u represent the collocation matrices, such that the B-splines with coefficients $c_{x,j} \in \mathbb{R}^{N+k_x-m_x}$ and $c_{u,w} \in \mathbb{R}^{N+k_u-m_u}$ have collocation points $x_j \in \mathbb{R}^N$ and $u_w \in \mathbb{R}^N$. The splines have knot multiplicity m_x and m_u and order k_x and k_u. The choice for B-spline order and knot multiplicity is described in Sections 4-3-2 and 4-3-3.

In case of the trapezoidal method, we define augmented state and control vectors $\tilde{x}, \tilde{u}$ and augmented spline coefficient vectors $\tilde{c}_x$ and $\tilde{c}_u$ as follows:

$$\tilde{x} = (x[1] \quad \cdots \quad x[N])^\top \qquad\qquad x \in \mathbb{R}^n \tag{4-14}$$
$$\tilde{u} = (u[1] \quad \cdots \quad u[N])^\top \qquad\qquad u \in \mathbb{R}^m \tag{4-15}$$
$$\tilde{c}_x = (c_x[1] \quad \cdots \quad c_x(N + k_x - m_x))^\top \qquad c_x \in \mathbb{R}^n \tag{4-16}$$
$$\tilde{c}_u = (c_u[1] \quad \cdots \quad c_u(N + k_x - m_x))^\top \qquad c_u \in \mathbb{R}^m \tag{4-17}$$

The vector of NLP decision variables $\tilde{c}$ is then composed of $\tilde{c}_x$ and $\tilde{c}_u$:

$$\tilde{c} = \begin{bmatrix} \tilde{c}_x \\ \tilde{c}_u \end{bmatrix} \tag{4-18}$$

We define Λ_x and Λ_u as follows:

$$\Lambda_x = L_x \otimes I_n \tag{4-19}$$
$$\Lambda_u = L_u \otimes I_o \tag{4-20}$$

Where $I_n \in \mathbb{R}^{n \times n}$ and $I_o \in \mathbb{R}^{o \times o}$ denote the Identity matrix and $\otimes$ is the Kronecker product. The augmented state and input vector $\tilde{x}$ and $\tilde{u}$ can be calculated from $\tilde{c}$ as follows:

$$\tilde{x} = \Lambda_x \tilde{c}_x \tag{4-21}$$
$$\tilde{u} = \Lambda_u \tilde{c}_u \tag{4-22}$$

4-3-2   Knot multiplicity

A knot multiplicity $m > 1$ could be used to reduce the freedom of the optimization problem. This can be attractive if high-frequent control activity is undesirable, but if at the same time a small discretization interval is required for maintaining a small integration error. However, in this thesis, a knot multiplicity of $m = 1$ was selected for all splines. For the state trajectories x a higher multiplicity leads to an unfeasible problem, since the number of defect constraints then exceeds the number of optimization variables describing the state trajectory. A higher multiplicity for the input trajectory results in the same issue with equality constraints $q \in \mathbb{R}^5$. However, this can be avoided by satisfying $q[i] = 0$ only for $i = \begin{bmatrix} m & 2m & \cdots & N \end{bmatrix}$. For the application in this work, this approach is unnecessary, since enough control over the continuity of the control input trajectory is obtained through the smoothness conditions implied by the B-spline order.

4-3-3   B-spline order

The B-spline order k_u for the input trajectory should be based on the expected optimal input trajectory, and on required smoothness. A too high order may reduce the integration accuracy, and furthermore slows down the optimization process [30]. Furthermore, a too high order may put unrealistic restrictions on the solution. An example is a problem in which the control input appears linearly in the cost function [31]. In such a case, bang-bang control is optimal, which cannot be represented by a B-spline order higher than zero.
In general, it can be expected that a higher B-spline order is suitable for approximating the state trajectory than for the control input trajectory, due to the integration steps in between. However, a too high spline order may imply additional conditions on the input trajectory, which is unwanted too. Therefor it is assumed that $k_x - k_u$ should be not higher than one.
Combining the statements above, it was chosen to use an as low as possible spline order for the control inputs, while maintaining robust convergence. Furthermore, the spline order for the state trajectory was chosen one order higher. This has lead to a quadratic B-spline for the control input trajectory, and a cubic B-spline for the state trajectory, hence $k_u = 3$, $k_x = 4$.

4-4   NLP problem formulation

Based on the information from the previous sections, we can compose the NLP formulation for solving the race car MTM problem. For the trapezoidal integration method, the formulation is as follows:

$$\min_{\tilde{c}} \quad J = \sum_{i=1}^{N-1} \frac{h[i]}{2} (S_f[i] + S_f[i+1])$$

$$\begin{aligned}
\text{s.t.} \qquad \tilde{\Phi} &= 0 \\
\Upsilon &= 0 \\
\tilde{q} &= 0 \\
\tilde{g} &\leq 0 \\
u_L \leq \tilde{u} &\leq u_U \\
\tilde{b}_l < \tilde{n} &< \tilde{b}_r
\end{aligned} \qquad (4\text{-}23)$$

Where the augmented state and control input vector are calculated from the vector of decision variables as follows:

$$\begin{bmatrix} \tilde{x} \\ \tilde{u} \end{bmatrix} = \begin{bmatrix} \Lambda_x & \Lambda_u \end{bmatrix} \tilde{c} \qquad (4\text{-}24)$$

4-5 Choice of NLP solver

For solving problem (4-23), several NLP methods exist [32]. The methods can be distinguished based on ao. the way of inequality constraint handling, globalization techniques and software interfaces. In [33] an overview of several solvers and their corresponding principles is given. There is no single superior method, outperforming every other method on each NLP. Instead, the suitability for a method to problem depends on the problem size, the number of constraints and its nonlinearity [32]. Our problem has the following characteristics:

- Number of decision variables up to 12.000, corresponding to roughly 1000 discretization points.

- Relative small number of free variables, i.e for 12 decision variables we have 10 equality constraints per discretization point.

- Highly nonlinear equality and inequality constraints resulting from the system dynamics.

The problem size suggests a need for large-scale sparse NLP methods. In the inventory of NLP solvers, two main available classes of methods are SQP and interior-point methods. In [32] it is stated that SQP methods are very effective for solving NLP problems, especially in the presence of nonlinear constraints. They are most efficient if the number of free variables is small, and are relatively robust for poorly scaled problems. On the other hand, it is stated that interior-point algorithms for NLP are very suitable for large-scale applications, in which they often outperform SQP methods.

As it is difficult to find a clear consensus in literature to which method is most suitable, it is decided to implement both an SQP method, and an interior-point method to problem (4-23) and compare their performance. In the following sections we will briefly describe the main differences between the methods and the solvers that we apply for both methods. In Section 4-8-1 the performance of two methods on the race car MTM problem is compared.

4-5-1   SQP methods

As the name suggests, in SQP a sequence of quadratic subproblems is solved to find the optimum. At each iterate, the NLP is approximated by a quadratic problem. Assume the following NLP:

$$
\begin{aligned}
\min_{x} \quad & f(x) && \text{(4-25)} \\
\text{s.t.} \quad & c(x) = 0 \\
& g(x) \leq 0
\end{aligned}
$$

With nonlinear cost function $f(x)$, and nonlinear equality and inequality constraint functions $c(x)$ and $g(x)$. The quadratic subproblem is given by a quadratic approximation of the cost function, and a linear approximation of the constraint functions.

$$
\begin{aligned}
\min_{p} \quad & f_k + \nabla F_k^\top p + \frac{1}{2}\nabla_{xx}^2 L_k p && \text{(4-26)} \\
\text{s.t.} \quad & \nabla c_k^\top p + c_k = 0 \\
& \nabla g_k^\top p + g_k \leq 0
\end{aligned}
$$

Here, f_k, c_k, g_k L_k denote the value of the cost and constraint functions and the Lagrangian at the current point. Where the minimizer p and corresponding lagrange multipliers λ_{k+1} of the quadratic subproblem are the basis for the NLP step. In addition, global convergence strategies such as line search and thrust region methods may be used to alter the direction or magnitude of the step that is taken. More elaborate descriptions of SQP and its details can be found in e.g. [32] or [34].

For the comparison in Section 4-8-1 we use SNOPT (Sparse Nonlinear OPTimizer) [34]. SNOPT is an implementation of an SQP algorithm exploiting sparsity in the constraint Jacobian. It uses line-search as globalization method, and has the ability to approximate the Hessian of the Lagrangian by a limited-memory BFGS update [32]. SNOPT is implemented in *FORTRAN77*, but has a MATLAB interface as well. For more details the reader is referred to [34].

4-5-2   Interior-point methods for NLP

Interior-point methods for NLP approximate inequality constrained problem (4-25) by a barrier problem, and use that as the subproblem for determining the NLP step:

$$
\begin{aligned}
\min_{x,s} \quad & f(x) - \mu \sum_{i=1}^{m} \ln s && \text{(4-27)} \\
\text{s.t.} \quad & c(x) = 0 \\
& g(x) - s = 0
\end{aligned}
$$

With positive barrier parameter μ and positive slack variable s. The interior-point method for NLP involves solving this subproblem several times, driving the barrier parameter μ to zero, such that the resulting solution coincides with the solution of the original problem [32]. As with SQP methods, different mechanisms are used for accepting and adjusting the step, including line-search, thrust region and filter methods. A more detailed description can be found in [32].

For the comparison in Section 4-8-1 we use the open-source solver IPOPT (Interior-Point OPTimizer) [35]. IPOPT solves the NLP by successive solution of a barrier problem, in which the barrier parameter is driven to 0. The subproblems are solved by an SQP method which uses a line search-filter method. As SNOPT, it includes the possibility to approximate the Hessian of the Lagrangian by a limited-memory BFGS update. IPOPT is written in C++ and is available in a MATLAB interface as well. For the mathematical details of the algorithm, the reader is referred to [36], [37], [38],[39], [35].

4-6 Calculation of derivative information

All NLP solvers require first- and second order derivative information for solving the problem. This means that the Jacobian and Hessian have to be calculated. Both IPOPT and SNOPT include the option to apply a limited-memory Broyden-Fletcher-Goldfarb-Shannon (BFGS) Hessian update. In this operation, the inverse Hessian is approximated by a few vectors that contain the information for the approximation. As such, this section only describes the calculation of the cost and constraint Jacobian.

Several methods exist for calculating derivative information. The most precise information is obtained if an analytical expression for the derivative of the cost and constraint function is used. However, for complex systems such an analytical expression might be difficult to obtain. An efficient alternative to this is the use of automatic differentiation, where the gradients are calculated by repeated application of the chain rule to the underlying model equations used by the differential equation solver [2]. The most simple way is to approximate the derivatives by using finite-differences. In the following, we will describe the calculation of the constraint Jacobian by sparse finite-differences, and the analytic expression for the cost function gradient.

4-6-1 Constraint Jacobian

For calculating the constraint Jacobian, the approach from [27] for making use of Jacobian sparsity was followed. The constraint function is composed of four components:

$$\Pi = \begin{bmatrix} \Upsilon \\ \tilde{\Phi} \\ \tilde{q} \\ \tilde{g} \end{bmatrix} \tag{4-28}$$

Where Υ is the initial boundary condition, $\tilde{q}$ and $\tilde{g}$ contain the path constraints, and $\tilde{\Phi}$ the augmented vector of residuals:

$$\tilde{\Phi} = (\Phi[1] \quad \Phi[2] \quad \cdots \quad \Phi[N-1])^\top \qquad \Phi[i] \in \mathbb{R}^n \qquad (4\text{-}29)$$

First we define the vector $\tilde{z}$:

$$\tilde{z} = \begin{bmatrix} \tilde{x} \\ \tilde{u} \end{bmatrix} \qquad (4\text{-}30)$$

Remember that $\tilde{x}$ and $\tilde{u}$ are calculated from the NLP decision variables by Equations (4-21) and (4-22). The derivative of Π to $\tilde{z}$ is then:

$$\frac{\partial \Pi}{\partial \tilde{z}} = \begin{bmatrix} \dfrac{\partial \Upsilon}{\partial \tilde{x}} & \dfrac{\partial \Upsilon}{\partial \tilde{u}} \\[1.5ex] \dfrac{\partial \tilde{\Phi}}{\partial \tilde{x}} & \dfrac{\partial \tilde{\Phi}}{\partial \tilde{u}} \\[1.5ex] \dfrac{\partial \tilde{q}}{\partial \tilde{x}} & \dfrac{\partial \tilde{q}}{\partial \tilde{u}} \\[1.5ex] \dfrac{\partial \tilde{g}}{\partial \tilde{x}} & \dfrac{\partial \tilde{g}}{\partial \tilde{u}} \end{bmatrix} \qquad (4\text{-}31)$$

The different partial derivatives in this equation will be described in the remainder of the section. $\tilde{\Phi}$ can be divided into a linear and nonlinear part.

$$\tilde{\Phi} = A\tilde{x} + B\varphi(\tilde{x}, \tilde{u}) \qquad (4\text{-}32)$$

Where all nonlinear relations are isolated in the vector $\varphi(\tilde{x}, \tilde{u})$, given by:

$$\varphi(X, U) = (f(x[1], u[1]) \quad f(x[2], u[2]) \quad \cdots \quad f(x[N-1], u[N-1])^\top \qquad (4\text{-}33)$$

The constant matrices $A \in \mathbb{R}^{(n \times N-1) \times (n \times N-1)}$ and $B \in \mathbb{R}^{(n \times N-1) \times (n \times N-1)}$ are dependent on the quadrature rule. For the trapezoidal method, A and B are defined as follows:

$$A = \begin{bmatrix} -I_n & I_n & & \\ & -I_n & I_n & \\ & & \ddots & \\ & & -I_n & I_n \end{bmatrix} \qquad (4\text{-}34)$$

$$B = -\frac{1}{2} \begin{bmatrix} h[1]I_n & h[1]I_n & & \\ & h[2]I_n & h[2]I_n & \\ & & \ddots & \\ & & h[N-1]I_n & h[N-1]I_n \end{bmatrix} \qquad (4\text{-}35)$$

Where $I_n \in \mathbb{R}^n$ denotes the identity matrix. The derivative of the residuals $\tilde{\Phi}$ to $\tilde{x}$ and $\tilde{u}$ is then given by:

$$\frac{\partial \tilde{\Phi}}{\partial \tilde{x}} = A + B \frac{\partial \varphi}{\partial \tilde{x}} \tag{4-36}$$

$$\frac{\partial \tilde{\Phi}}{\partial \tilde{u}} = B \frac{\partial \varphi}{\partial \tilde{u}} \tag{4-37}$$

Since $\dfrac{\partial f(x[i], u[i])}{\partial x(j)} = 0$ and $\dfrac{\partial f(x[i], u[i])}{\partial u(j)} = 0$ for all $i \neq j$, the matrices $\dfrac{\partial \varphi}{\partial \tilde{x}}$ and $\dfrac{\partial \varphi}{\partial \tilde{u}}$ turn out to be block-diagonal:

$$\frac{\partial \varphi}{\partial \tilde{x}} = \begin{bmatrix} \frac{\partial f(x[1], u[1])}{\partial x[1]} & & & \\ & \frac{\partial f(x[2], u[2])}{\partial x[2]} & & \\ & & \ddots & \\ & & & \frac{\partial f(x[N], u[N])}{\partial x[N]} \end{bmatrix} \tag{4-38}$$

$$\frac{\partial \varphi}{\partial \tilde{u}} = \begin{bmatrix} \frac{\partial f(x[1], u[1])}{\partial u[1]} & & & \\ & \frac{\partial f(x[2], u[2])}{\partial u[2]} & & \\ & & \ddots & \\ & & & \frac{\partial f(x[N], u[N])}{\partial u[N]} \end{bmatrix} \tag{4-39}$$

For the path constraints $\tilde{g}$ and $\tilde{q}$ the same applies:

$$\frac{\partial g(x[i], u[i])}{\partial x(j)} = 0 \tag{4-40}$$

$$\frac{\partial g(x[i], u[i])}{\partial u(j)} = 0 \tag{4-41}$$

$$\frac{\partial q(x[i], u[i])}{\partial x(j)} = 0 \tag{4-42}$$

$$\frac{\partial q(x[i], u[i])}{\partial u(j)} = 0 \tag{4-43}$$

For all $i \neq j$. This leads to the following equations for the partial derivatives of $\tilde{g}$ and $\tilde{q}$:

$$\frac{\partial \tilde{g}}{\partial \tilde{x}} = \begin{bmatrix} \dfrac{\partial g(x[1], u[1])}{\partial x[1]} & & & \\ & \dfrac{\partial g(x[2], u[2])}{\partial x[2]} & & \\ & & \ddots & \\ & & & \dfrac{\partial g(x[N], u[N])}{\partial x[N]} \end{bmatrix} \qquad (4\text{-}44)$$

$$\frac{\partial \tilde{g}}{\partial \tilde{u}} = \begin{bmatrix} \dfrac{\partial g(x[1], u[1])}{\partial u[1]} & & & \\ & \dfrac{\partial g(x[2], u[2])}{\partial u[2]} & & \\ & & \ddots & \\ & & & \dfrac{\partial g(x[N], u[N])}{\partial u[N]} \end{bmatrix} \qquad (4\text{-}45)$$

$$\frac{\partial \tilde{q}}{\partial \tilde{x}} = \begin{bmatrix} \dfrac{\partial q(x[1], u[1])}{\partial x[1]} & & & \\ & \dfrac{\partial q(x[2], u[2])}{\partial x[2]} & & \\ & & \ddots & \\ & & & \dfrac{\partial q(x[N], u[N])}{\partial x[N]} \end{bmatrix} \qquad (4\text{-}46)$$

$$\frac{\partial \tilde{q}}{\partial \tilde{u}} = \begin{bmatrix} \dfrac{\partial q(x[1], u[1])}{\partial u[1]} & & & \\ & \dfrac{\partial q(x[2], u[2])}{\partial u[2]} & & \\ & & \ddots & \\ & & & \dfrac{\partial q(x[N], u[N])}{\partial u[N]} \end{bmatrix} \qquad (4\text{-}47)$$

The elements on the diagonals of $\dfrac{\partial \tilde{\Phi}}{\partial \tilde{z}}$, $\dfrac{\partial tlg}{\partial \tilde{z}}$ and $\dfrac{\partial tlq}{\partial \tilde{z}}$ can be calculated either analytically or by using finite-differences. As described in Chapter 2, the equations of motion consist of analytic functions only. Hence, an analytic expression for the constraints could be obtained. This however means that a change in vehicle model requires new analytic expressions for the derivative. It is expected that the used vehicle model is depending on the problem to be analyzed. The need for finding new analytical derivatives thereby reduces the flexibility of the method, which is undesired. Therefore it was chosen to approximate the derivatives by finite-differences. Note that due to the use of the sparse Jacobian structure, one evaluation of $\dfrac{\partial \tilde{\Phi}}{\partial \tilde{z}}$ only requires $(n + o) \times N$ equations-of-motion evaluations. For the calculation of $\dfrac{\partial \tilde{g}}{\partial \tilde{z}}$ and $\dfrac{\partial \tilde{q}}{\partial \tilde{z}}$ a small amount of additional calculations is needed ((3-16)-(3-16), (3-22)-(3-24)).

Finally, the gradient of Υ is given by:

$$\frac{\partial \Upsilon}{\partial \tilde{x}} = (I_n \quad 0 \quad \cdots \quad 0)^\top \tag{4-48}$$

$$\frac{\partial \Upsilon}{\partial \tilde{u}} = (0 \quad \cdots \quad 0)^\top \tag{4-49}$$

$$\tag{4-50}$$

Formulate Jacobian based on B-spline coefficients As described in Section 4-3 the NLP decision variables are the B-spline coefficients $\tilde{c}_x$ and $\tilde{c}_u$. Using (4-21), (4-22), (4-31) and the chain rule, we obtain the following relation for the Jacobian:

$$\frac{\partial \Pi}{\partial \tilde{c}} = \frac{\partial \Pi}{\partial \tilde{z}} \frac{\partial \tilde{z}}{\partial \tilde{c}}$$

$$= \begin{bmatrix} \dfrac{\partial \Upsilon}{\partial \tilde{x}} & \dfrac{\partial \Upsilon}{\partial \tilde{u}} \\[2mm] \dfrac{\partial \tilde{\Phi}}{\partial \tilde{x}} & \dfrac{\partial \tilde{\Phi}}{\partial \tilde{u}} \\[2mm] \dfrac{\partial \tilde{q}}{\partial \tilde{x}} & \dfrac{\partial \tilde{q}}{\partial \tilde{u}} \\[2mm] \dfrac{\partial \tilde{g}}{\partial \tilde{x}} & \dfrac{\partial \tilde{g}}{\partial \tilde{u}} \end{bmatrix} \begin{bmatrix} \Lambda_x \\[1mm] \Lambda_u \end{bmatrix} \tag{4-51}$$

4-6-2   Cost function gradient

As can be seen from (4-23), the cost function only depends on S_f and h. It turns out that the relation is relatively simple, therefor the cost function gradient is calculated analytically. First of all, it can be seen that S_f does not depend on u at all, hence $\dfrac{\partial J}{\partial \tilde{c}_u} = 0$. Using the chain rule, the cost gradient can be written as:

$$\frac{\partial J}{\partial \tilde{c}_x} = \frac{\partial J}{\partial \tilde{S}_f} \frac{\partial \tilde{S}_f}{\partial \tilde{x}} \frac{\partial \tilde{x}}{\partial \tilde{c}_x} \tag{4-52}$$

$$= \frac{\partial J}{\partial \tilde{S}_f} \frac{\partial \tilde{S}_f}{\partial \tilde{x}} \Lambda_x \tag{4-53}$$

Where $\tilde{S}_f$ is the augmented time to distance scaling factor, given by:

$$\tilde{S}_f = (S_f[1] \quad S_f[2] \quad \cdots \quad S_f[N])^\top \tag{4-54}$$

The first term in (4-52) can be obtained by deriving the cost term in (4-23). For the trapezoidal rule this results in:

$$\frac{\partial J}{\partial \tilde{S}_f} = (0.5h[1] \quad 1h[2] \quad 1h[2] \quad ... \quad 1 \quad 1 \quad 0.5h[N-1]) \tag{4-55}$$

The partial derivative of S_f to the state vector x is given by deriving Equation (3-7) analytically, resulting in the following expressions:

$$\frac{\partial S_f}{\partial n} = \frac{C}{V\cos(\beta+\xi)} \tag{4-56}$$

$$\frac{\partial S_f}{\partial \xi} = -\frac{V\sin(\beta-\xi)(Cn-1)}{(V\cos(\beta+\xi))^2} \tag{4-57}$$

$$\frac{\partial S_f}{\partial V} = \frac{\cos(\beta+\xi)(Cn-1)}{(V\cos(\beta+\xi))^2} \tag{4-58}$$

$$\frac{\partial S_f}{\partial \beta} = -\frac{V\sin(\beta-\xi)(Cn-1}{(V\cos(\beta+\xi))^2} \tag{4-59}$$

$$\frac{\partial S_f}{\partial \dot{\psi}} = 0 \tag{4-60}$$

4-7   Problem scaling

As stated in [27] and [32], scaling is important for robust and rapid convergence of an NLP. For scaling of the NLP decision variables and constraints, the procedure described in [27], p. 166 was followed. Briefly summarized, the following rules were applied:

- The scaling for each state and input is kept constant over all discretization points

- The states and inputs are normalized by their expected extreme values, either based on their upper and lower bounds or knowledge about the physical system

- The constraints related to integration defects are scaled such that the defect gradients are normalized

- The path constraints are scaled such that their elements in the Jacobian are normalized

The scaling of the cost function remains as a tuning parameter for the user. To maintain robust and rapid convergence for different discretization intervals, the following rule was applied for cost function scaling:

$$\varrho_J = \frac{a}{\bar{h}} \tag{4-61}$$

Where ϱ_J denotes the cost function scaling, a the user tuning parameter, and $\bar{h}$ the mean discretization interval, given by:

$$\bar{h} = \frac{1}{N-1} \sum_{i=1}^{N-1} s[i+1] - s[i] \tag{4-62}$$

In this way, the magnitude of the elements in the scaled cost gradient is roughly independent from the chosen discretization interval.

Table 4-1: Maneuvers for NLP solver comparison

Name	Distance [m]	Description of turn sequence
Single hairpin	196	50m straight - 180deg turn - 50m straight
Double hairpin	391	Maneuver 1, twice
Triple hairpin	587	Maneuver 1, three times
Simple turn	116	50m straight - 180deg turn - 20m straight

4-8   Comparison of NLP formulation choices through simulation

Although there is a large amount of literature available with NLP applications of optimal control, the exact performance is still hard to predict. This section therefore contains some short simulation studies about choices made during the process. First of all, a comparison of applicability of the SNOPT and IPOPT to the race car MTM problem is done. Then, the influence of the sampling interval on accuracy for a simple problem is investigated.

4-8-1   Comparison between SNOPT and IPOPT

For solving NLP problem (4-23), two different solvers are compared. The first one is the SQP-based solver SNOPT, and the second one is the interior-point based solver IPOPT. For the comparison, four different maneuvers are considered. The methods are compared on the following criteria:

- Convergence (yes/no)

- Cost J at optimal solution, to see whether the methods have the tendency to converge to the same local optimum.

- Number of iterations *Iter*.

- Total computation time T_{comp}.

For making the results comparable, the same constraint and cost tolerance is used for both methods. The maneuvers for comparison are described in Table 4-1. Figure 4-1 shows a graphical representation of the coordinates of the track boundaries in the 2D Cartesian frame. The first basic maneuver is the so-called hairpin, which we define as a turn where the center-line makes a rotation of 180 degrees. The solvers are compared on this maneuver for various discretization intervals h. For comparing the solvers on longer maneuvers, the maneuver is simply augmented by itself, hence the hairpin is executed multiple times. The second maneuver is a 90-degree right-hand turn, followed by a very short straight line section. This maneuver was included to compare the performance of the two solvers in case of a relatively simple, but highly dynamic maneuver.

Table 4-2: Results of NLP solver comparison. All blue numbers correspond to IPOPT, all red numbers to SNOPT.

Maneuver	h [m]	Size	T_{comp} [Min]	*Iter*	J [s]
Triple hairpin	1	8850	2.68 / -	1507/-	20.081 / -
Double hairpin	1	5910	0.87 / 25.67	741 /298	13.388 / 13.389
Single hairpin	1	2970	0.38 / 2.66	632 /165	6.679 / 6.679
Single hairpin	2	1500	0.23 / 0.80	637 /172	6.659 / 6.673
Single hairpin	4	765	0.14 / 0.19	540 /145	6.605 / 6.606
Simple turn	2	915	0.17 / 0.17	625 /80	3.685 / 3.685

Results   The results of the comparison are shown in Table 4-2. All IPOPT and SNOPT results are shown in blue and red respectively. The column named *Size* lists the total number of decision variables for each problem. Looking at the quality of the solution, it can be seen that in most cases the two methods converged to the same solution. Only in case of the single hairpin discretized with a $2m$ interval, the two methods converged to a different local minimum. In this case, the solution found by SNOPT corresponds has a slightly higher cost. The second observation is that SNOPT requires less iterations to converge to the solution. This difference becomes apparent especially for the simplest maneuver, where SNOPT requires only 80 iterations, in contrast to IPOPT which needs 625.

In terms of computation time, IPOPT and SNOPT are very similar for the two smallest problems. However, for the larger problems the computation time for SNOPT is multiple times longer than for IPOPT. For the largest problem of the study, SNOPT does not converge at all. The largest problem that we were able to solve with SNOPT had about 6000 variables, but with small changes in parameters often SNOPT already fails to converge for problem sizes larger than 2000. In these situations, it is observed that the number of *minor iterations* needed for solving the Quadratic Programming (QP) subproblem explodes. Hence, the solver appears to have difficulties in solving the QP subproblem for larger problem sizes.

Discussion   Summarizing the results, it can be said that SNOPT and IPOPT perform similar in terms of computation time for very small problems. In these cases, SNOPT requires considerably less iterations. For larger problems IPOPT performs considerably better. SNOPT does not meet the requirement stated in Section 4-5.

The outcome corresponds to the statement in [32] that interior-point methods often outperform SQP methods for large problems. An alternative SQP method that could be tried however is WORHP (We Optimize Really Huge Problems). This is another SQP-based NLP solver, which is said to be succesfully applied for very large problems [40]. Unfortunately, time did not allow for trying this solver in this work. Instead, IPOPT was selected as solver for the problems described in the remaining sections.

4-8-2   Influence of sampling interval on accuracy

In discretizing the problem, a trade-off has to be made between problem size and accuracy. On the one hand, a reduction in discretization interval leads to a smaller error in approximat-
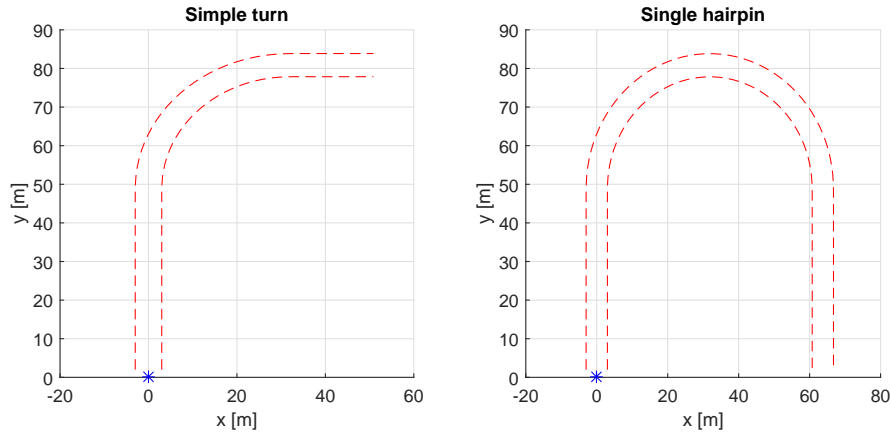
Figure 4-1: Maneuvers for NLP solver comparison. The red dashed lines mark the track edges. The blue asterisk marks the start point of the maneuver.

ing the solution of the differential equations. On the other hand, this increases the problem size, leading to longer computation times and an increase in required memory.

To determine the required sampling interval, a small accuracy study is done. A simple problem is optimized for various sampling intervals. In this case, the single 90 degree turn was used. As a measure for the accuracy, we look at the difference in maneuver time compared to the solution with the smallest discretization interval. It is expected that the benefits of an increase in mesh density will reduce for finer grids. Furthermore, the state and control input trajectory of the solutions with different sampling intervals are compared, to judge the differences qualitatively.

Results   The results are shown in Figure 4-2. Displayed is the maneuver time difference, compared to the benchmark which has a discretization interval of $0.25m$. In the right figure the relative maneuver time difference is shown. As can be seen, the difference stays close to 0 for $h \leq 1$. For larger discretization intervals the difference increases. The qualitative difference in control input and state trajectory for $h = 0.25m, 1m, 4m$ is shown in Figure 4-3 and 4-4. As can be seen, the $4m$ grid clearly introduces some loss in details. The qualitative difference between the solution with $h = 0.25m$ and $h = 1m$ however is very small.

Discussion   Although the maneuver time sensitivity to discretization interval is small, the qualitative differences for the solution are evident. In future work, it is recommended to asses the accuracy in a different way. Furthermore, it is expected that the required interval depends on the maneuver and model parameters. As such, for future application it would be practical to assess the required interval automatically. In [27] a way for estimating the local integration error is given. The same estimate is used in an automatic grid refinement step. In e.g.[41] and [42] other mesh refinement algorithms are given.
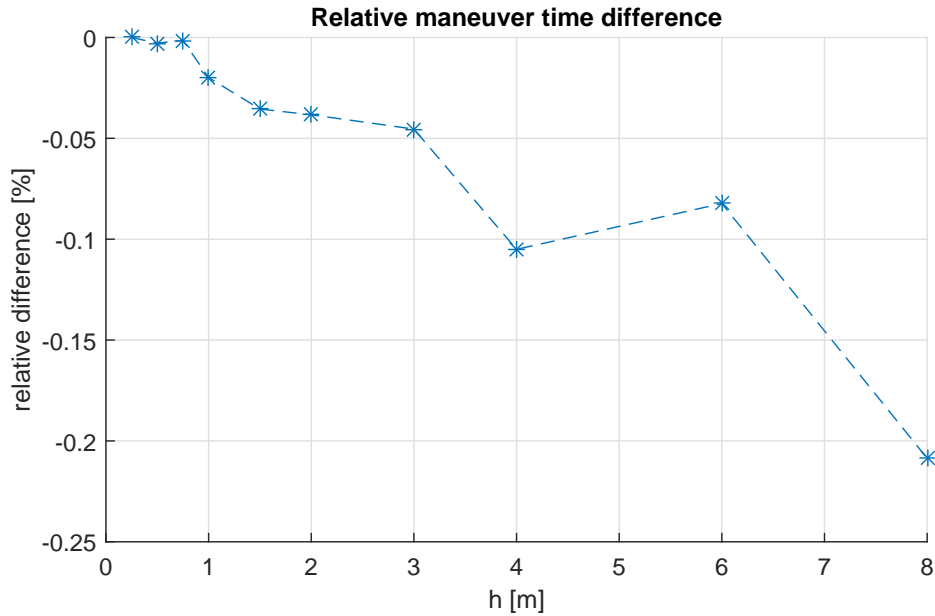
Figure 4-2: Relative maneuver time difference for difference mesh sizes.

4-9   Conclusion

This chapter described the transformation of the race car MTM problem into an NLP problem. The maneuver is discretized on a non-uniform grid $s_0 = s[1] < ... < s[N] = s_F$. The full collocation method is used for the transcription of the OCP into an NLP. As a result, the differential equations are solved by bringing the residuals related to the integration of the dynamics to zero. For this thesis, the trapezoidal rule is used for integrating the dynamics. To find the required discretization interval, a small study of the accuracy as a function of the discretization interval was performed. In this study, the mesh density is varied from $0.25m$ to $8m$ in 10 steps, where the accuracy is evaluated by the influence on maneuver time and the differences in state trajectory. For that particular maneuver, an increase of mesh density beyond $1m$ shows very little change in maneuver time. Furthermore, no visible qualitative differences in state trajectories are seen beyond this distance, leading to the conclusion that a finer grid than this is not needed.

For robust convergence and the ability to control the smoothness of the solution, the state and input trajectories are parameterized as B-spline coefficients. Hence, the variables that the NLP algorithm sees are the coefficients of the B-splines forming the state and input trajectories. With quadratic splines representing the input trajectory, and cubic splines for the state trajectory, robust convergence to a smooth solution is achieved.

To preserve flexibility in vehicle modeling, the constraint Jacobian is approximated using finite-differences. The knowledge of the sparsity of the Jacobian is used to construct the Jacobian with a minimal number of equation of motion evaluations. The cost gradient is calculated using analytic expressions, which were derived in Section 4-6-2.
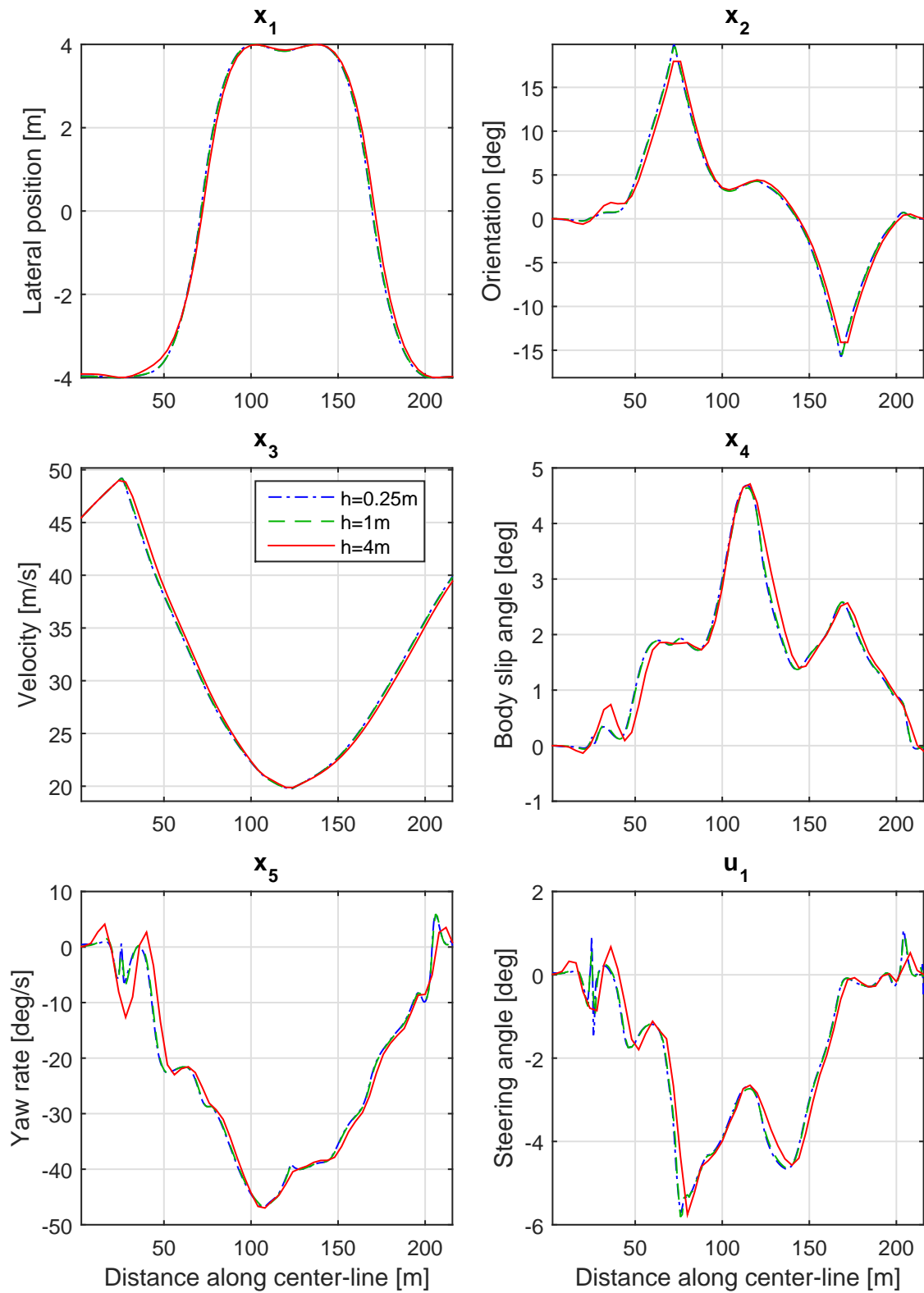
Figure 4-3: Qualitative difference between solutions with different mesh sizes. x_1 to x_5 and u_1.
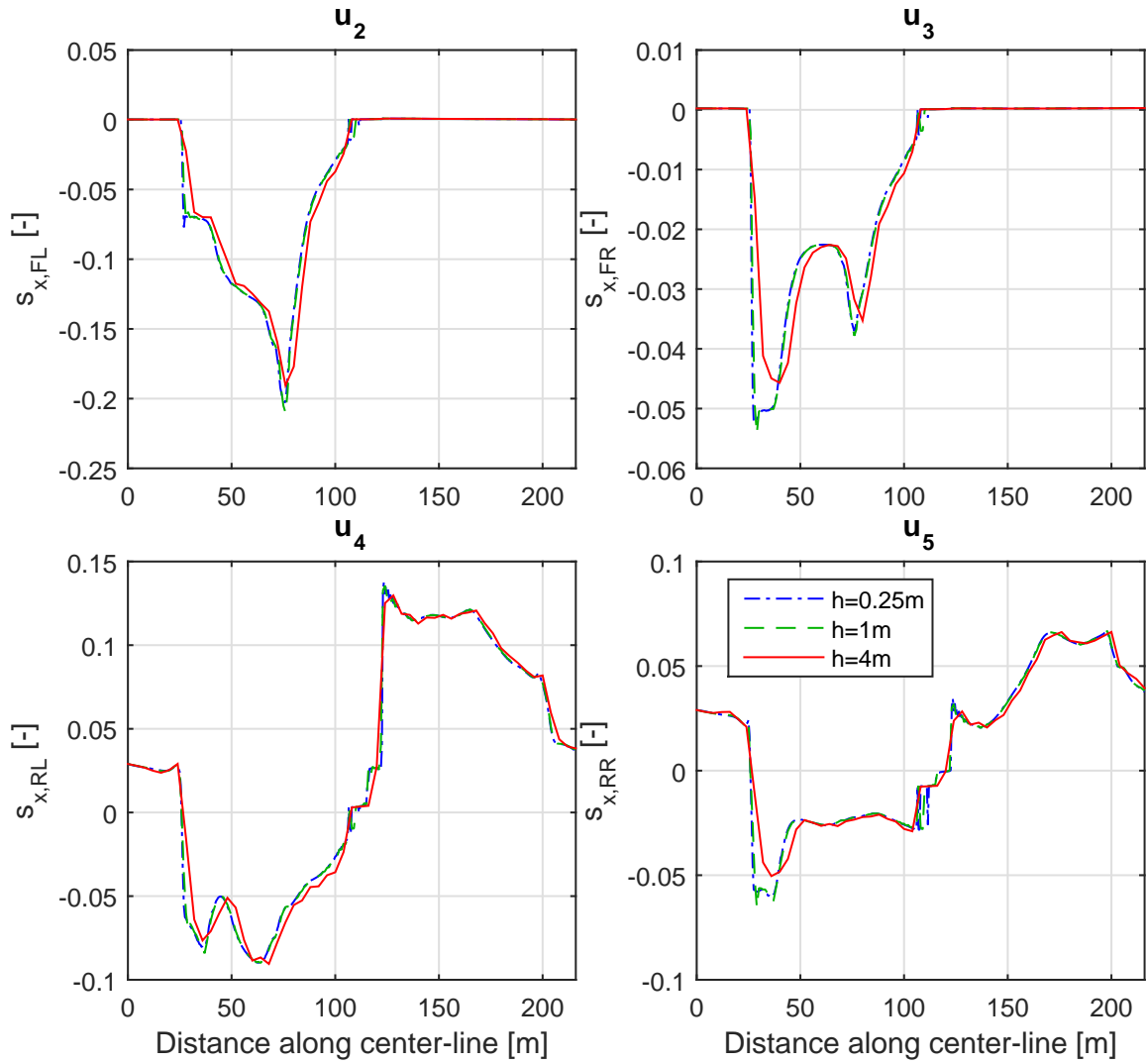
Figure 4-4: Qualitative difference between solutions with different mesh sizes. u_2 to u_5.

Two main classes of solvers for NLP problems are SQP and Interior-point methods. In Section 4-8-1, the SQP solver SNOPT is compared to the interior-point solver IPOPT by its performance on the race car MTM. For various problems, the two solvers are compared on their convergence, total computation time and the value of the cost function at the solution. The solution quality for both methods appears to be equal for these problems; the same solution was reached in all but one case. Where for problems with less than 1000 variables the two methods perform similarly, for larger problems IPOPT is clearly superior for this application. For a problem with 5910 variables, corresponding to a maneuver with length 391m on a 1m grid, the computation time of SNOPT is about 30 times longer than that of IPOPT. For even larger problems, SNOPT fails to converge. This finding is in line with NLP literature, where it is stated that for large-scale problems interior-point methods often outperform SQP. Though not included in this thesis, future studies using the large-scale WORHP solver would be of interest for exploiting the benefits that SQP methods offer.

Simulation studies

Part of the motivation for a trajectory planning method for race car simulation is the possibility to simulate highly dynamic maneuvers where the control inputs are highly dependent on the vehicle parameters. Furthermore, the method can be used to detect active performance limitations in different stages of maneuvers. In Section 5-1 some notions for race car driving are defined to facilitate description and comparison of results. In the first simulation study in Section 5-2, the choice to neglect wheel rotational dynamics in the model is validated by a comparison with a reference model through simulation. Additionally the method is applied for two studies closely related to the design of Traction Control (TC) systems.

First, the optimal control solution for a hairpin maneuver at three different radii is studied in Section 5-3. The tire utilization and normalized tire slips on the optimal solution are evaluated, and the stability and control properties of the vehicle along the optimal trajectory are assessed using a linearized reduced system at each discretization point.

Second, a perturbation analysis is performed. In the real-life control task some uncertainty in both the driving path and parameters exists. The driver might cause small deviations in trajectory, the tire-road friction could be reduced locally as a result of moisture, sand or unevenness and other disturbances such as wind may act on the car. In Section 5-4, the optimal reaction of control inputs to a local variation in tire-road friction and perturbations to the state vector is studied. We evaluate to what extent the longitudinal control reaction is based on preview of road-friction and knowledge about the lateral position and orientation of the vehicle. The reaction of the control inputs to disturbances in the state vector is studied qualitatively and related to the dynamics along the trajectory of the nominal solution.

5-1 Definitions

In this section some notions related to race car driving are defined, for convenience in describing the results in the following sections.

Braking point   The braking point is defined as the instant in distance on which the front longitudinal tire force $F_{x,f}$ changes from 0 into a negative value:

$$\left\{ \min_i s[i] \quad | \quad F_{x,f} < 0 \right\} \tag{5-1}$$

Usually one single turn includes one single braking point.

Braking zone   The braking zone is defined as the distance interval:

$$\{\forall s \quad | \quad F_{x,f} < 0\} \tag{5-2}$$

Usually, the braking zone consists of one closed interval for each turn.

Throttle point   The throttle point is defined as the following instant in distance:

$$\left\{ \min_i s[i] \quad | \quad T_E > T_{E,\mathrm{drg}} \right\} \tag{5-3}$$

Hence, the instant at which a positive longitudinal control input is added to the engine drag torque.

Turn entry   For defining turn entry, the definition of path curvature is needed:

$$\kappa = \frac{F_y}{mV^2} \tag{5-4}$$

Turn entry is defined as the following distance interval:

$$\left\{ \forall s \quad | \quad 0.1 < \frac{\|\kappa\|}{\|\kappa_M\|} < 0.9, \quad F_{x,f} \leq 0 \right\} \tag{5-5}$$

Where $\|\kappa_M\|$ is the maximum path curvature experienced during the maneuver. Hence, it is the distance interval on which the path curvature is increased, which is usually a sub-interval of the braking zone.

Turn exit   We define turn exit as the following interval:

$$\{\forall s \quad | \quad T_{E,\mathrm{drg}} < T_E, \quad g_1 < 0\} \tag{5-6}$$

Hence, it is the interval in which positive longitudinal control is applied and on which the power constraint is strictly satisfied.

Overdriving   We define that a tire is overdriven under the following condition $\mathtt{s} > 1$. An axle is overdriven if this conditions applies to both tires on the axle.

Normalized root-mean-square deviation (NRMSD)   The NRMSD of two signals can be seen as the normalized standard deviation of the difference, and is given by:

$$\text{NRMSD} = \frac{\sqrt{\frac{\sum\limits_{i=1}^{N}(x_1-x_2)^2}{N}}}{x_{\max}-x_{\min}} \tag{5-7}$$

Where x_1 and x_2 are the signals to be compared and N the number of variables and $x_{\max}$ and $x_{\min}$ the maximum and minimum value of the states respectively.

5-2   Simulation study 1: Influence of neglecting wheel dynamics

In this Section the choice for neglecting wheel rotational dynamics is validated. This is done via a comparison with the reference model defined in Section 3-4, which does include the wheel rotational velocities in the state vector. The following two questions are answered:

1. What is the difference in state trajectory and maneuver time for the two formulations?

2. Is incorporating the wheel stability constraint described in Section 3-3-3 necessary?

For answering the first question three different maneuvers are used. A graphical representation of the track boundaries for all three maneuvers is shown in Figure 5-1. Maneuver 1 is a hairpin with a center-line radius of 30m. The initial conditions are set such that the maneuver both incorporates braking in a straight line, and combined braking and turning. Maneuver 2 has a right-hand turn with a center-line radius of 30m as well, but only rotates 90 degrees. Maneuver 3 includes a faster right-left combination, and a 30m radius right-hand hairpin. It is included because it is highly dynamic, with the braking point in the left-hand turn and a change in curvature direction during the braking zone. For all maneuvers a discretization interval of 1m is used.

Maneuver time and trajectory   The results of the study are shown in Table 5-1. As can be seen, the maneuver times are within 0.06% for all maneuvers. The largest relative difference is seen for maneuver 1. The state trajectory for both formulations is shown in Figure 5-2, together with the NRMSD. Visually the trajectories are close, and the maximum NRMSD for the states is equal to 1.5%. The maximum NRMSD is equal to 2.8%, but is should be noted that this is mainly caused by the phase difference around $s = 150$. For the studies in this thesis, the difference is accepted.

Wheel stability constraint   Remarkably enough, the wheel stability constraints are inactive throughout all maneuvers in Table 5-1. This induces the question whether the wheel stability constraints are really needed or not. Figure 5-3 shows a solution without wheel stability constraints. As can be seen, the stability constraint for the front-right tire would be violated at several instances (where it is negative). At these points the longitudinal slip jumps to
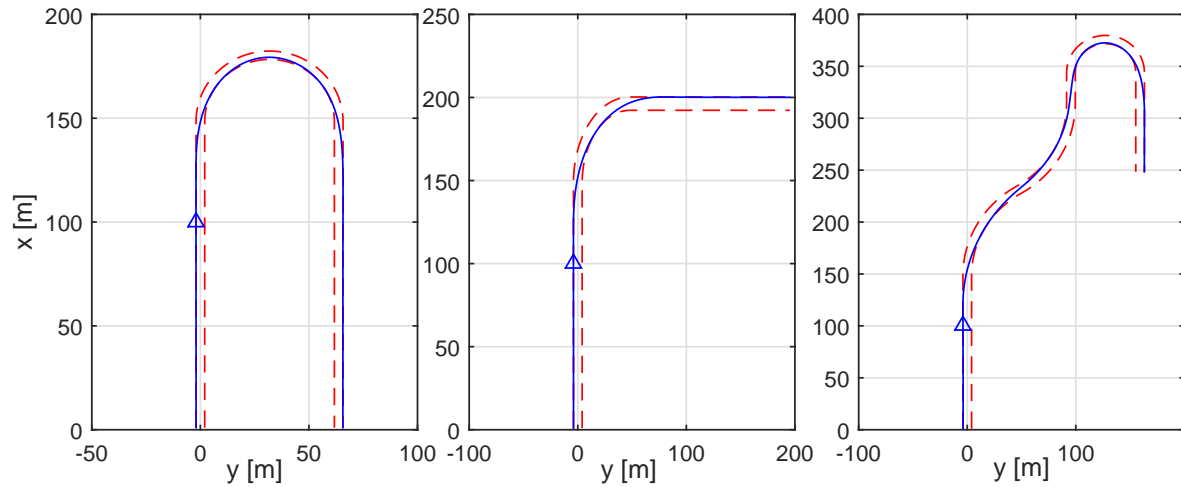
Figure 5-1: Maneuvers for simulation study 1

high negative values. The higher slip corresponds to the same longitudinal force, which is possible because the slip-force characteristic (2-1) is non-monotonically increasing. As such, constraint (3-18) saying that the left and right braking force should be equal is still satisfied. The maneuver time for this solution is 10.787s, which is higher than the solution including stability constraints. Apparently, the absence of the stability constraints does not lead to a misuse of the formulation in a positive manner, but rather makes it converge to a worse local minimum.

Table 5-1: Results of simulation study 1

Name	Simplified $J[s]$	Reference $J[s]$	Relative difference %
Maneuver 1	10.718	10.724	0.056
Maneuver 2	8.024	8.027	0.037
Maneuver 3	13.388	13.394	0.045
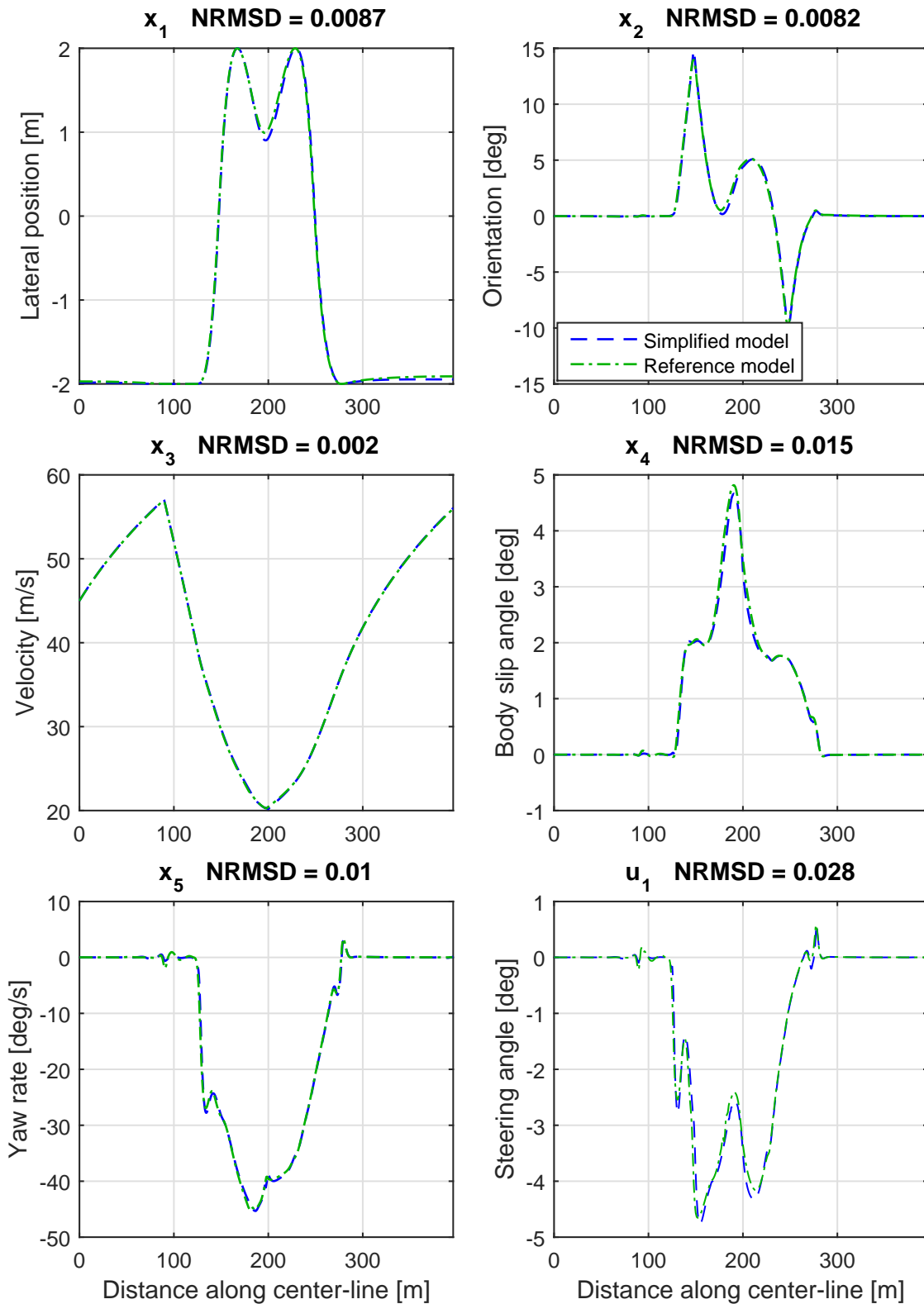
Figure 5-2: Comparison of state trajectory between the simplified model (blue) and the reference model with wheel rotational velocities (green) for the hairpin maneuver.
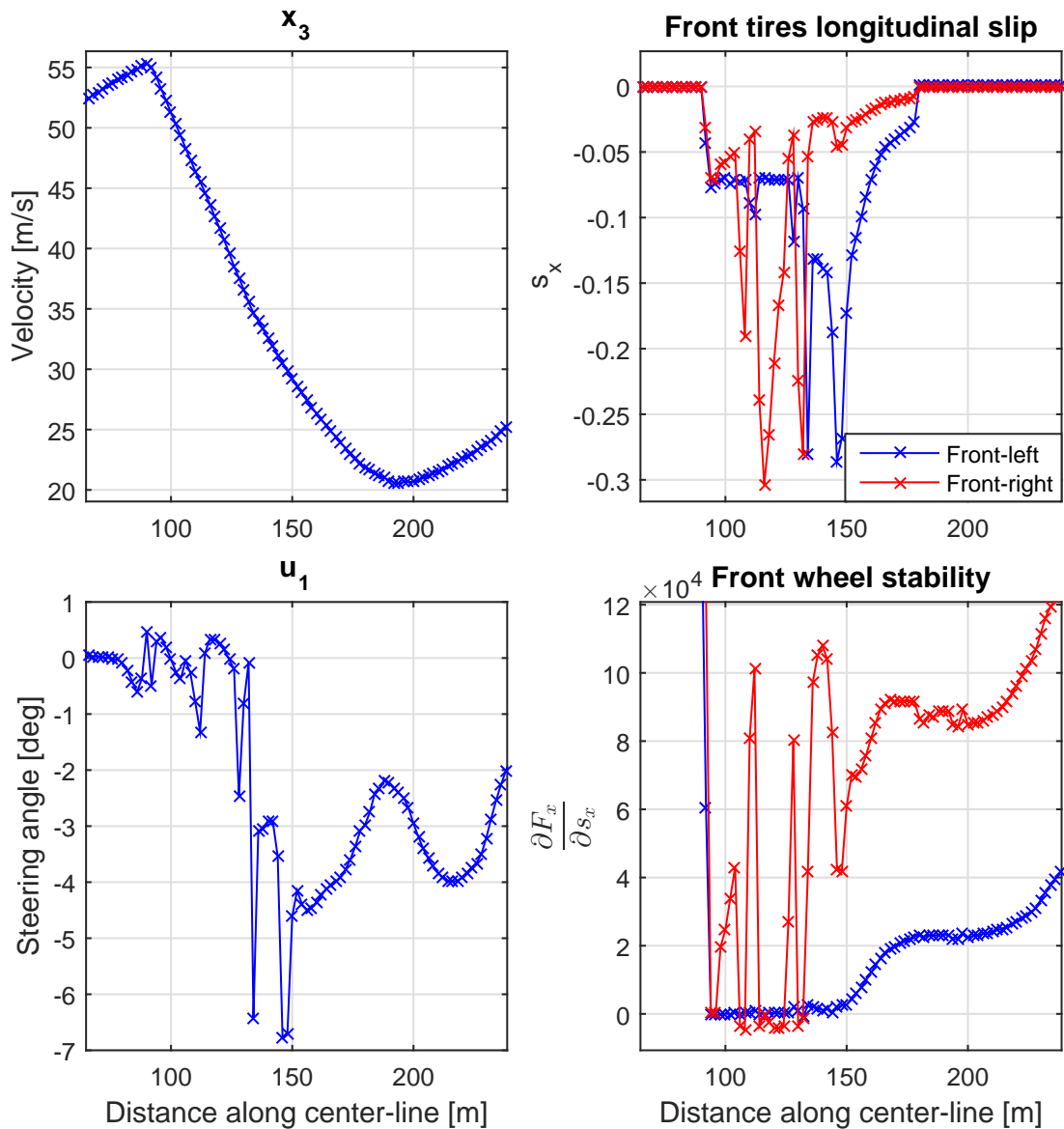
Figure 5-3: Solution without wheel stability constrained for the simplified formulation. The markers correspond to the values at the discretization points

5-3   Simulation study 2: Study of optimal solution

In this section we study the optimal solution more closely. Specifically, three different questions closely related to TC design are answered, from which some conclusions and new questions are deducted. The questions that are answered are introduced and listed below:

1. In [1] it is cited that time-optimal driving is all about keeping a maximum acceleration in the right direction. The forces accelerating the vehicle are transmitted through the tires. It is known that the transmittable tire force is limited, defined by a saturation

in force-slip characteristics. Does the optimal trajectory use the maximum tire friction force at all times?

2. Since the majority of the control inputs driving the vehicle come from the human driver, we are interested in the stability and control properties at the optimal trajectory. Although the system nonlinearity does not allow for a simple expression for global stability, information about local stability can be derived from the linearized system, following the first method of Lyapunov (as explained in e.g. [43]). The question that is answered reads: is the open-loop vehicle locally stable on the optimal trajectory?

3. As will appear, some zeros exist in the single input, single output (SISO) transfer functions from steering angle to linearized bicycle model outputs. We pose the question how these zeros evolve over the turn, and how they are dependent on maneuver speed.

Approach, setting and assumptions To keep the descriptions concise and clear, the study is limited to hairpin maneuvers. Since it is known that car dynamics change much over velocity [24], we perform the nominal study for three different turn radii which typically exist on a race track. The properties of the maneuvers are displayed in Table 5-2. The radii lead to velocity minima of roughly 70, 120 and 160 km/h respectively.

Table 5-2: Maneuvers for simulation study 2

Name	Turn radius [m]	Width [m]	Description of turn sequence
Low speed	35	10	150m straight - 180deg turn - 100m straight
Medium speed	70	10	150m straight - 180deg turn - 100m straight
High speed	105	10	150m straight - 180deg turn - 100m straight

5-3-1   Overview of considered quantities

In the following, some quantities are introduced that help to answer the posed questions. These quantities are displayed in the figures with results and will be used in the descriptions.

Normalized longitudinal control input The longitudinal control inputs as applied by the driver are the throttle and brake pedal. In this thesis these are defined as follows:

$$\text{Throttle} = \frac{T_E(\omega_{rl} + \omega_{rr})}{2P_E} \tag{5-8}$$

$$\text{Brake} = \begin{cases} \frac{F_{x,f}}{\min F_{x,f}} & \text{if} \quad F_{x,f} \leq 0 \\ 0 & \text{otherwise} \end{cases} \tag{5-9}$$

Note that Throttle with this definition represents normalized power, and Brake a normalized force. Although the actual longitudinal control inputs are the longitudinal slips at each tire, throttle and brake are more convenient for analyzing the solution.

Tire utilization The tire utilization $\mathcal{F} \in [0, 1]$ is defined as:

$$\mathcal{F}_i = \frac{\|F_i\|}{F_{M,i}} \tag{5-10}$$

For $i = fl, fr, rl, rr$. $\|F\|$ denotes the euclidean norm of the longitudinal and lateral tire force, and F_M the maximum tire force as defined in the tire model. We look at $\mathcal{F}$ for each individual tire, as a measure for the utilization of the tire's friction potential.

Normalized tire slip Closely related to the tire utilization are the lateral slip (A-65) to (A-68) and the normalized absolute slip $\mathbf{s} \in [0, +\infty)$:

$$\mathbf{s}_i = \frac{\|s_i\|}{s_{M,i}} \tag{5-11}$$

For $i = fl, fr, rl, rr$. $\|s\|$ denotes the euclidean norm of the longitudinal and lateral tire slip, and s_M the slip corresponding to maximum tire force as defined in the tire model. Our tire model given in Chapter 2 is parameterized such that $F_M > F_S$. Then, by definition for $\mathcal{F} = 1$, $\mathbf{s} = 1$. In addition we are interested to see whether s_M is exceeded in the solution or not.

Eigenvalues and zeros The nonlinear character of the vehicle model does not allow for a simple expression for global stability. As a measure for local stability of the full nonlinear system, the eigenvalues of the linearized system at each discretization interval are used, referred to as the first method of Lyapunov [43]. Furthermore, we are interested in the stability of the planar dynamics, without the effect of the (slow) longitudinal dynamics incorporated. Therefore, the state vector of the linearized system is reduced to $x = (\dot{\psi} \quad \beta)^\top$, as in e.g. [1], [22]. Note that the resulting system has the same form as described in (2-25). The eigenvalues are calculated using the local partial derivatives at each discretization interval, which can be extraced from the $\frac{\partial \varphi}{\partial \tilde{x}}$ and $\frac{\partial \varphi}{\partial \tilde{u}}$ vectors in the NLP Jacobian calculation described in Section 4-6.

Using the same information, the zeros of the following two SISO transfer functions are calculated:

$$H_1(s) = \frac{\dot{\psi}(s)}{\delta(s)} \tag{5-12}$$

$$H_2(s) = \frac{\beta(s)}{\delta(s)} \tag{5-13}$$

$$\tag{5-14}$$

The transfer functions of $s_{x,i}$ to β and $\dot{\psi}$ are not considered, since these are not independent control inputs. The zeros of the δ transfer function are displayed as an indication of input-output controllability of the respective outputs with steering angle. For more information on the interpretation of zeros and eigenvalues, the reader is referred to [43].

Yaw rate for constant body slip angle The final quantity referred to in the results is the yaw rate for constant body slip angle, defined as:

$$\dot{\psi}_{\dot{\beta}=0} = \frac{A_y}{V} \tag{5-15}$$

The quantity is displayed in the same graph as $\dot{\psi}$. It should be noted that the difference between the two is equal to the time derivative of β.

5-3-2 Results of nominal study at three different velocities

Figure 5-4 to Figure 5-9 show the results for the hairpin with center-line radius 35m, 70m and 105m. The questions are answered on the basis the quantities described previously and the plots.

1. Utilization of tire friction As can be seen the tire utilization $\mathcal{F}$ is not equal to one all the time. All deviations from this can be divided in roughly three categories:

- All four tires are not fully utilized.

- Both tires on one of the axles are not fully utilized.

- On one axle, only one of the tires has full friction utilization.

The **first deviation** is observed in the first and last section of the maneuver, at which the vehicle is driving in a straight line with the power limit $g_1 < 0$ active.

The **second deviation** shows the following stages:

1. $\mathcal{F}_f < 1$ and $\mathcal{F}_r \approx 1$ under initial braking, where the vehicle is braking in a straight line. This deviation is caused by the constant brake torque distribution, which does not allow to increase the front braking force without exceeding the slip for maximal rear longitudinal force.

2. $\mathcal{F}_f < 1$ and $\mathcal{F}_r \approx 1$ at initial turn-in while still braking

3. $\mathcal{F}_f \approx 1$ and $\mathcal{F}_r < 1$ for a large portion of the turn, at which first braking is decreased to zero, and afterwards throttle is increased.

4. $\mathcal{F}_f < 1$ and $\mathcal{F}_r \approx 1$ under combined positive longitudinal acceleration and turning in the final phase of the turn. For the high-speed maneuver, this stage is absent since the power constraint becomes active before this point is reached.

It can be said that subsequently the front and rear axle are utilized fully, with a small overlap on the transitions on which both axles are close to the condition $\mathcal{F} \approx 1$. Interestingly, from the normalized slip $\mathtt{s}$ it is observed that in stage 2 and 3, covering a large portion of the turn, the non-fully utilized axle has a higher than optimal slip, hence $\mathtt{s} > 1$.

The **third deviation** is observed in the following occasions:

- In the turn-in phase while braking, the right (outside) tires have lower friction utilization than the inside tires. The inside tires have a lower wheel load, due to lateral load transfer. The force on these tires is limited by wheel stability constraint g_2. Shortly after this, the situation is the opposite: the axles are overdriven mainly as a result of lateral slip, and the wheel load difference causes the inside tires to be further away from $\mathbf{s} = 1$ than the outside tires.

- On turn-exit, $\mathcal{F}_{rl} < \mathcal{F}_{rr}$ and $\mathbf{s}_{rl} > \mathbf{s}_{rr}$. The limited-slip differential places the two tires on a single rotating body. The axle torque and slip are mainly determined by the stability of the outside tire, which has more wheel load due to lateral load transfer. As a result, the inside tire is overdriven. It should be noted that the difference is smaller than for the first item.

In general it can be said that tire utilization differences on one axle are caused by different slip and load conditions on the tires on this axle, and that they are therefore unavoidable. The longitudinal force limit is then decided by the stability of one of the wheels, or by the stability of the combined body in case of a locked differential.

2. Open-loop stability of linearized lateral dynamics For all three velocities, it can be seen that there are two distance intervals in the maneuver where one of the eigenvalues is positive. The first interval is always under straight-line braking. This corresponds to the findings of Chapter 2. This unstable section is followed by a stable, underdamped arc, which corresponds to the segment where $\mathcal{F}_f < 1$ and $\mathbf{s}_f > 1$. Following on this is another unstable segment, on which can also be seen that $\mathbf{s}_r > 1$. The effect of the slow unstable pole is seen in the body slip angle trajectory. There is only a small change in the control inputs, yet the body slip angle grows exponentially towards the middle of the turn. The trajectory of the steering angle is such that it compensates for β and $\dot{\psi}$, keeping the front lateral slip on a close to constant value. As such, it does not act on the unstable dynamics.

For all three turn radii, the positive eigenvalue turns negative as soon as throttle is applied. This corresponds to the findings in Chapter 2 regarding the influence of longitudinal load transfer and a limited-slip differential. Furthermore, the eigenvalues turn into a complex pair on the largest segment of the turn exit. No significant oscillations due to this are observed though.

3. Input-output zeros of linearized lateral dynamics As can be seen, on the major part of the maneuver at all three radii there is a right-half plane (RHP) zero in $H_1(s)$. Hence, in controlling the body slip angle with steering angle, an inverse response is present. This effect can be explained on the basis of (A-38):

$$\dot{\beta} = \dot{\psi} + \frac{F_y \cos\beta - F_x \sin\beta}{mV}$$

As can be seen, $\dot{\beta}$ is nonzero in case of a difference between $\dot{\psi}$ and $\frac{A_y}{V}$. A change in steering angle leads to an opposite change in F_y and M_z. F_y acts directly on $\dot{\beta}$, but M_z only acts on

the derivative of $\dot{\psi}$, causing the opposite direction short- and long term response.

As can be seen, the RHP zero is closest to the imaginary axis for the small-radius turn. This can be explained by the inverse speed term in (A-38). In addition, transfer function $H_2(s)$ features one zero, which becomes slower towards the middle of the turn, and has a short positive interval. The short positive interval coincides with the interval on which $\mathbf{s}_f > 1$. Furthermore, around this interval the zeros in both transfer functions go to large positive and negative values in an inverse relation. This is caused by the small discrepancy in the point where $\dfrac{\partial \beta}{\partial \delta}$ and $\dfrac{\partial \dot{\psi}}{\partial \delta}$ switch sign, as is shown in Figure 5-10 for the 30m radius turn.

The presence of the RHP zeros indicates that the vehicle may be difficult to control using steering angle inputs, especially on the intervals where the RHP in $H_1(s)$ is small, and on the interval where both zeros are positive. It is therefore not surprising that the majority of the control action using front lateral slip variations occurs on turn entry, where the RHP zero in $H_1(s)$ is still larger than 30.

Additional observations   From the results, the following observations regarding optimal control inputs can be done as well.

- For the major part of the turn the front lateral slip $s_{y,fl}$ and $s_{y,fr}$ are constant and on or slightly over the slip for maximal lateral force. Hence, the steering angle just follows and compensates for the influence of other states on front lateral slip. This phenomenon is clearest in the high-speed turn. Furthermore, the application of throttle has a clear influence on the yaw rate and body slip angle trajectory. This behavior is remarkable, since it means that stabilizing the dynamics and following the trajectory is done by a combination of the longitudinal control input and timing of the initial steering angle inputs.

- For all three turn radii, there is a step wise increase in positive longitudinal control input on turn exit. In addition, in the low and medium speed turn there is an interval with a small amount of positive longitudinal control before the step wise increase. As can be seen from the change in $\dot{\psi}$ and the difference between $\dot{\psi}$ and $\frac{A_y}{V}$, the body slip angle decreases rapidly in this interval. These observations leave the question to what decides the timing and magnitude of both the initial low throttle interval and the step wise increase.
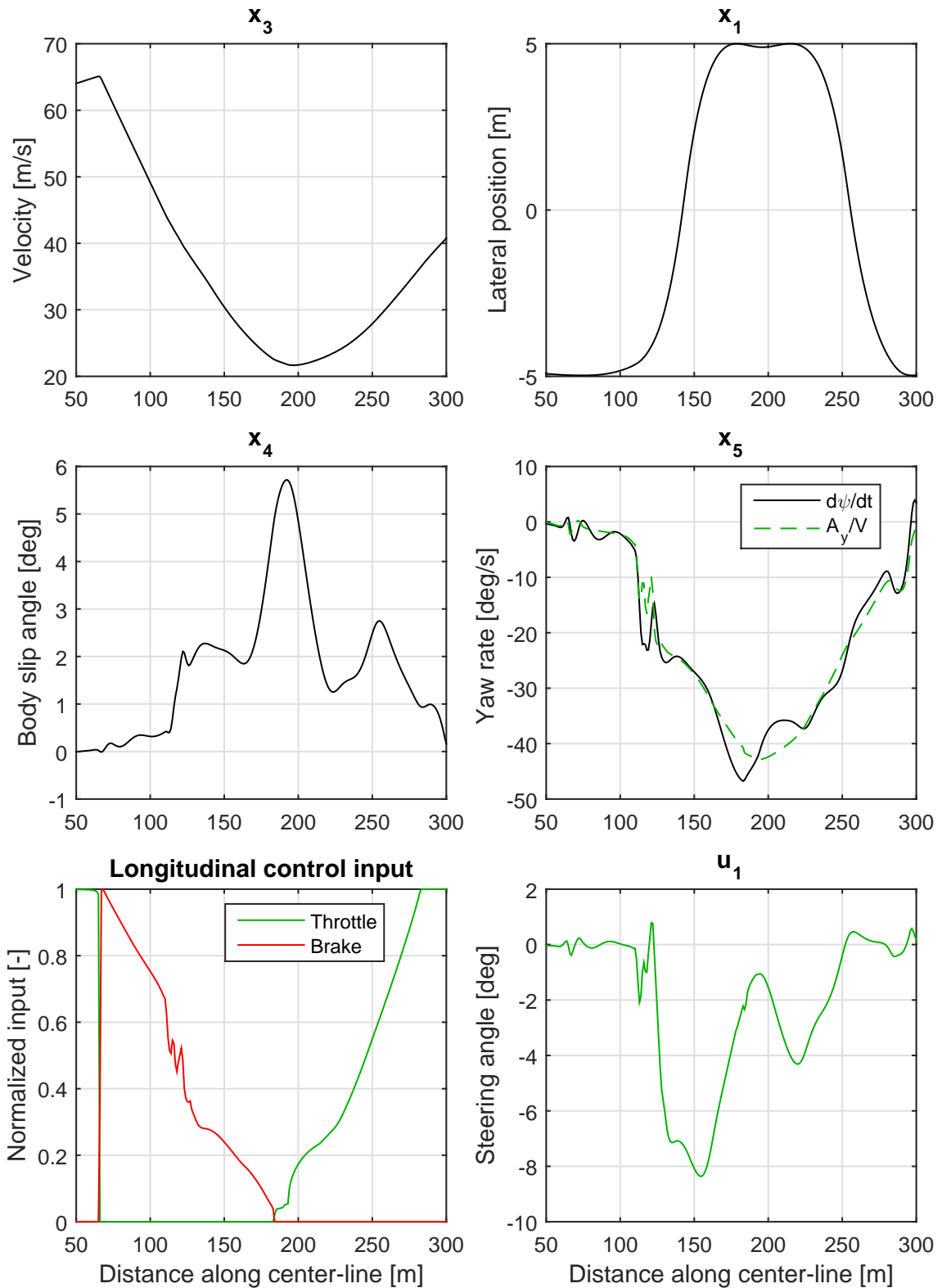
Figure 5-4: Nominal results of 35m radius hairpin, selection of states and inputs
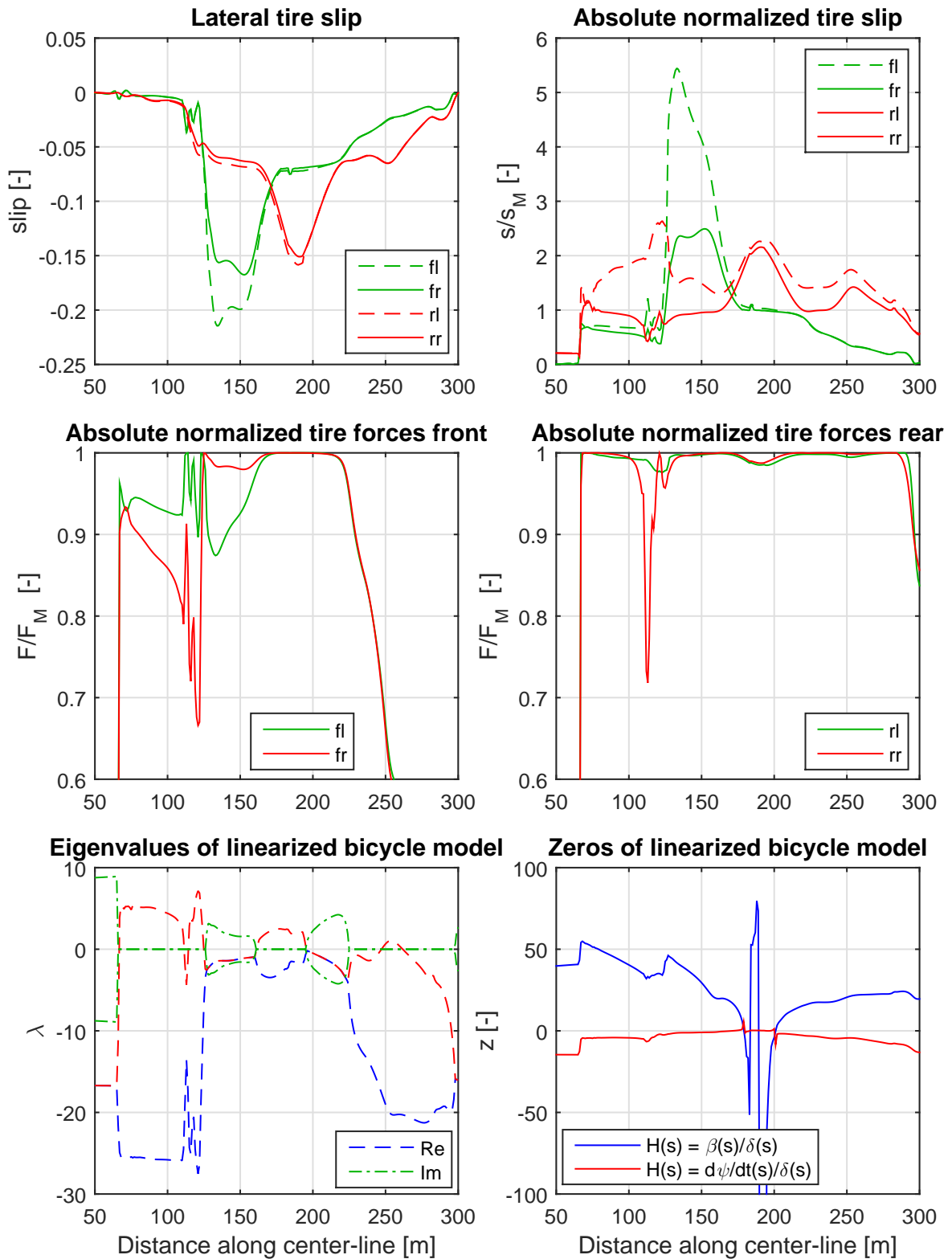
Figure 5-5: Nominal results of 35m radius hairpin. Tire slip s and s_y, tire utilization $\mathcal{F}$, eigenvalues and zeros of locally linearized system
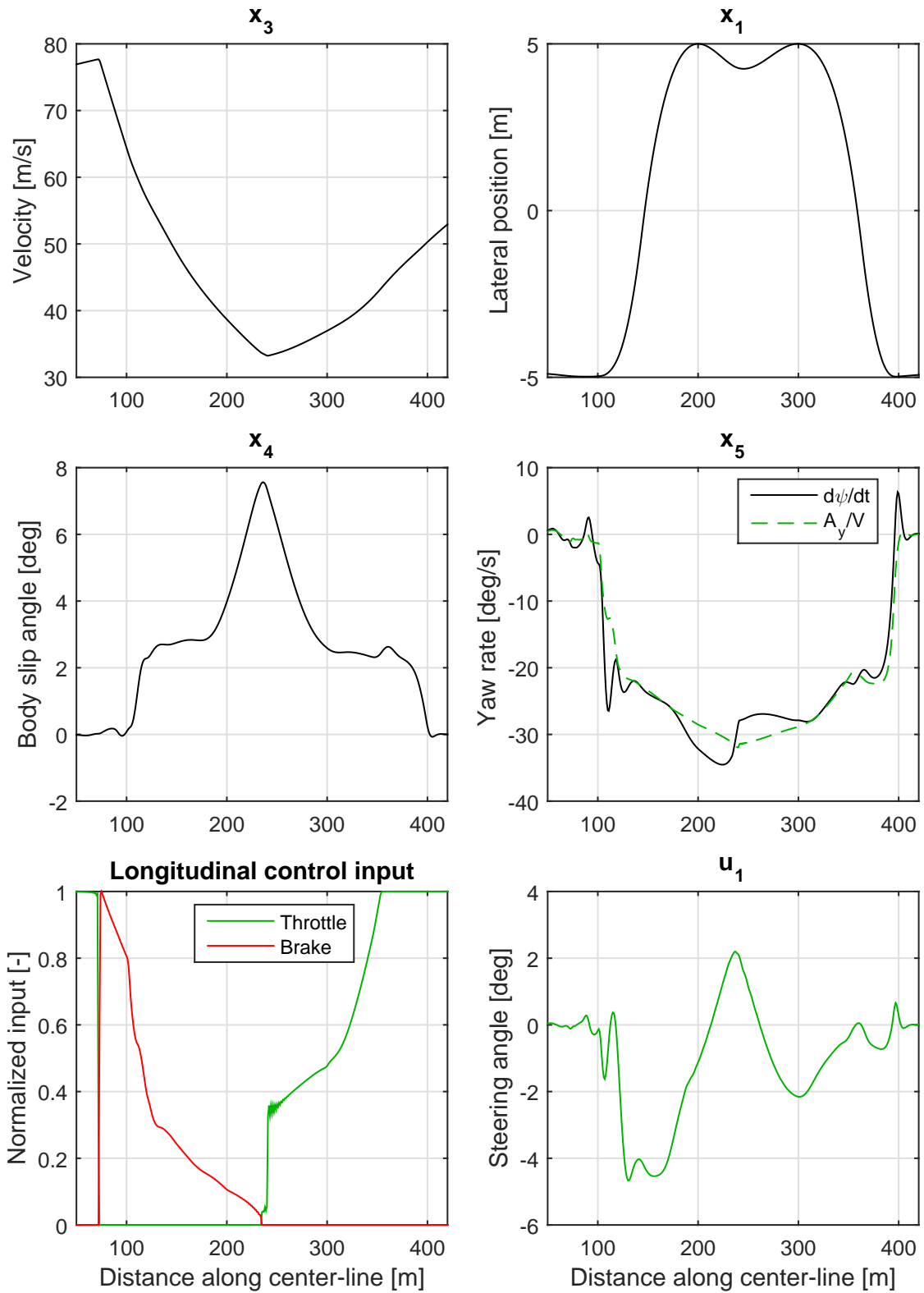
Figure 5-6: Nominal results of 70m radius hairpin, selection of states and inputs
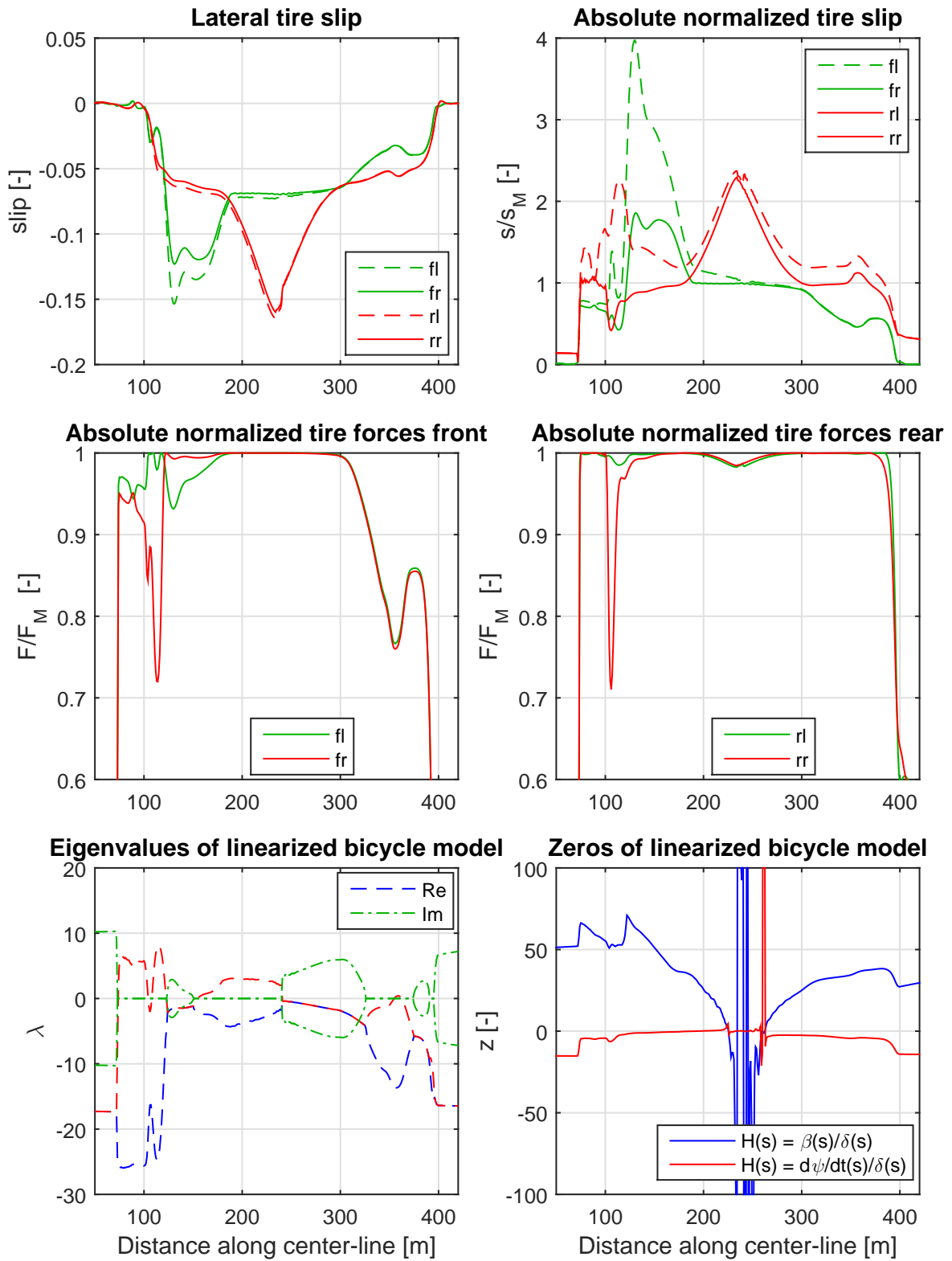
Figure 5-7: Nominal results of 70m radius hairpin. Tire slip s and s_y, tire utilization $\mathcal{F}$, eigenvalues and zeros of locally linearized system
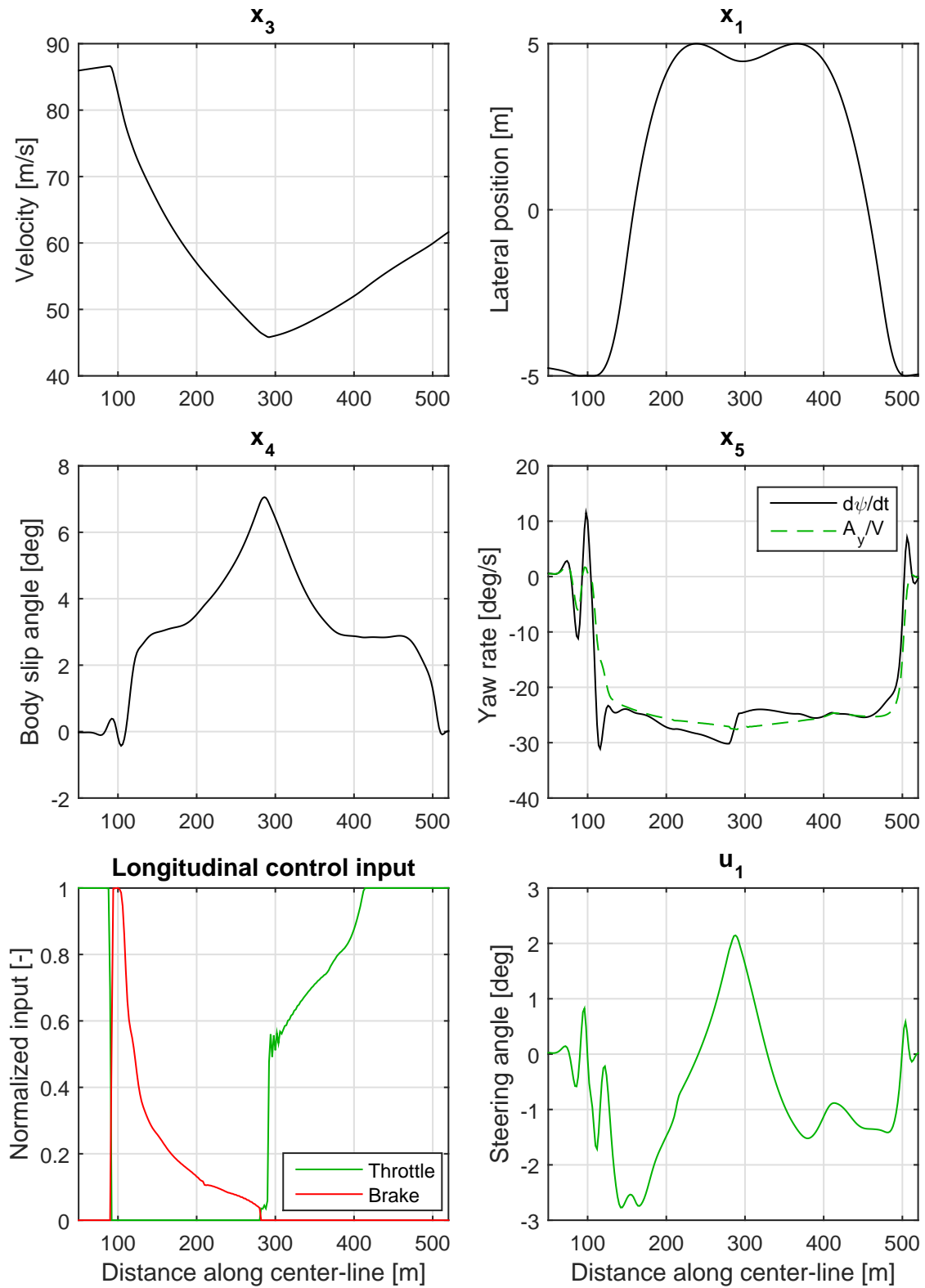
Figure 5-8: Nominal results of 105m radius hairpin, selection of states and inputs
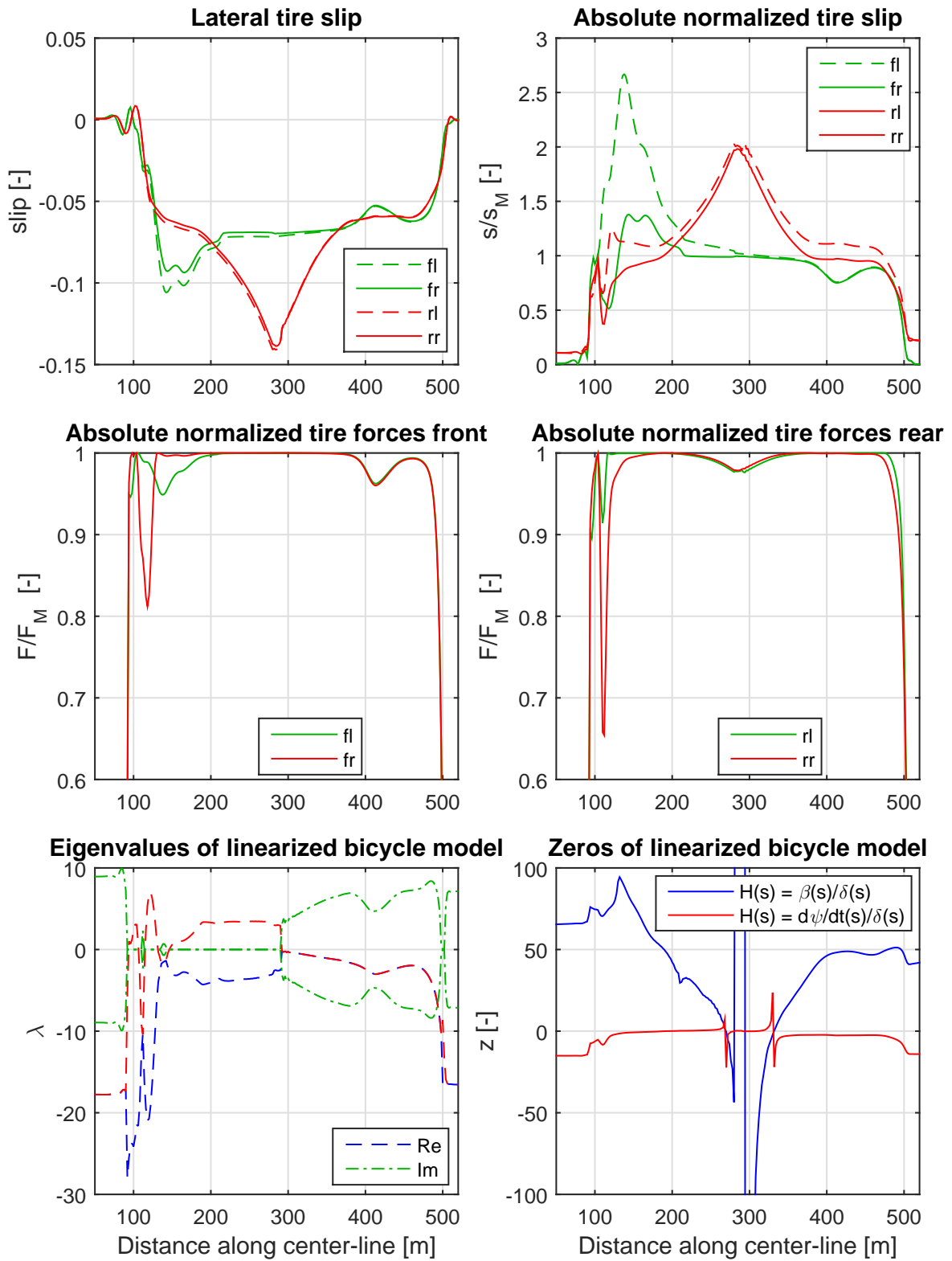
Figure 5-9: Nominal results of 105m radius hairpin. Tire slip s and s_y, tire utilization $\mathcal{F}$, eigenvalues and zeros of locally linearized system
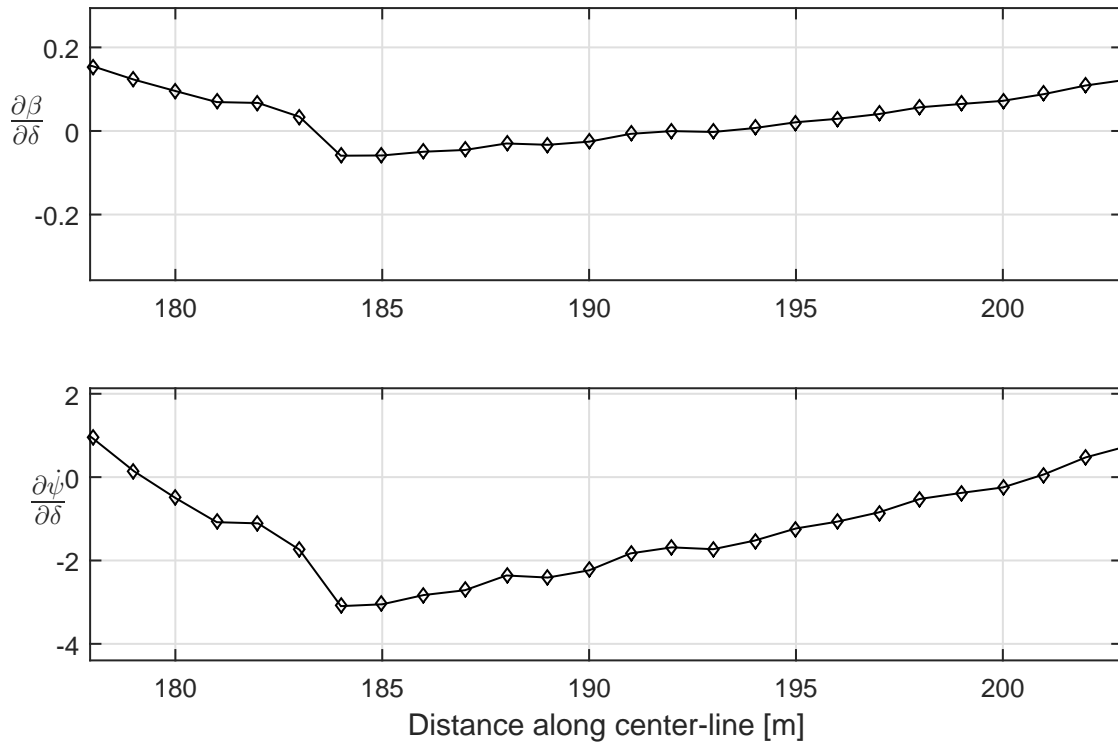
Figure 5-10: Control derivatives around $s = 190$m of the 30m radius hairpin

5-3-3   Conclusion and further questions

It can be concluded that full tire force potential is not always used for each tire. The deviations are caused by longitudinal force potential differences on the same axle, and by the need for globally stable yaw dynamics. Although the solution includes intervals under which close to full tire utilization for both axles is extended at the cost of yaw accelerations, it appears inevitable that one of the axles is not on its full potential all the time. Under initial turn-in, this is the front axle, and in a long interval in the middle of the turn the rear axle is below its full potential. In both situations, the underused axle is overdriven, hence its normalized slip is larger than one. It should be noted that this conclusion cannot be generalized, but only applies for this particular set of vehicle parameters and the hairpin maneuver.

In a large portion of the turn, the vehicle has locally open-loop unstable yaw dynamics. At the same time, controlling the dynamics with steering angle changes especially around the middle of the turn may be difficult, due to the presence of RHP zeros in the transfer functions from steering angle to body slip angle and yaw rate. Apart from the initial turn-in, the steering angle control input is such that the front lateral slip corresponding to full tire utilization is maintained, by compensating for vehicle state changes.

A final observation is the step wise increase in positive longitudinal control on turn exit, following on a interval with low, close to constant throttle for the medium and low speed turns.

Further questions

- The front tires lateral slip $s_{y,f}$ has a long constant zone. Furthermore there appear two RHP zeros in steering angle control. How does the reduced closed-loop bandwidth limit imposed by the RHP zeros affect the rejection of state disturbances in this phase?

- It was observed that the throttle has a step wise increase on turn exit. Since the control from the front tire lateral forces is minimal throughout the turn, it is suspected that the size of this step is related to the influence of the longitudinal force on yaw dynamics. What is the exact timing and magnitude of this step depending on?

- As was seen, most of the time one of the axles is overdriven. This includes turn exit, which is a useful result for TC. However, practical experience in the field tells that real drivers do not tend to overdrive the rear axle as much towards the middle of the turn. If overdriving on turn entry is not present, is the rear axle then still overdriven on turn exit?

The first question is treated in the perturbation study in Section 5-4, in which local perturbations are applied to the states. The last two questions are recommended for future work.

5-4   Simulation study 3: perturbation analysis

In reality, the vehicle may be subject to disturbances, such as local variations in road friction, wheel load variations through road unevenness and wind gusts. This, and the impreciseness of the human driver causes the state at a certain distance in the maneuver to vary from repetition to repetition. As mentioned before in some racing series TC is used, which makes the longitudinal control inputs partly determined by a semi-automated system. At the same time, the steering angle is determined entirely by the race driver. In this section it is studied what the ratio is between the reactions of these two control inputs in the rejection of disturbances to state and conditions under positive longitudinal acceleration.

The disturbances that are considered are:

- A local reduction of maximum tire force, to emulate a wet patch of tarmac or a dip in the road.

- A perturbation to the state-vector, in particular yaw rate and body-slip angle.

Note that the latter may occur as a result of the former: a local reduction in track grip leads to an increase of body slip angle, and depending on the state at the time of the disturbance, also to a change in yaw rate. In some cases, a disturbance might be known to a driver, for example in case of a crest in the road. In other cases, the disturbance might be unknown, e.g. if conditions change rapidly, or in case of a rough vertical road profile and a slightly different driving path.
We are interested in the adaption of the control input trajectory to both an expected and an unexpected disturbance. More specifically, the questions that are answered are:

1. Would TC need preview to reject grip disturbances in a time-optimal fashion?

2. Does a disturbance to the state in turn exit lead to a deviation from optimal front slip ($\mathbf{s}_f \neq 1$), or to a change in longitudinal control?

5-4-1   Local reduction in maximum friction force

The maneuver for the study is a medium-speed hairpin, with equal radius as in the nominal study. The parameter denoting maximum tire friction F_M is reduced to 80% in the interval $175 \leq s < 185$m. Three different cases are considered:

- The entire maneuver is solved with the information F_M described above.

- The problem is initialized at $s = 175$, at initial boundary condition $x = x_n[k_s]$, where $x_n[i]$ is the state trajectory of a nominal solution without any variations in F_M, and k_s corresponding to $s = 175$.

- The problem is initialized at $s = 175$, at initial boundary condition $x = x_n[k_s]$, where $x_n[i]$ is the state trajectory of a nominal solution without any variations in F_M, and k_s corresponding to $s = 175$. In addition, the control inputs are fixed to $u = u_n[k_s]$, where $u_n[i]$ is the control input trajectory of a nominal solution without any variations in F_M. This shows the natural response of the vehicle to the disturbance.

We will refer to these three cases as *with preview*, *without preview* and *without preview and action*. The results for the former two and the nominal solution are displayed in Figure 5-11. The maneuver times are shown in Table 5-3. The maneuver times from the problems initialized at $s = 175$m are obtained by adding the time of the interval $0 \leq s < 175$ of the nominal solution to the time of the interval $175 \leq s < s[N]$ of the perturbed solution. As can be seen, the time increases about 0.7% with preview. Without preview, this becomes 1%, and without reaction to the disturbance until $s = 185$ the increase in maneuver time is 1.1%.

Looking at the figures, first of all it can be seen that the reduction in throttle is multiple times smaller with preview. Furthermore it can be seen that with preview the lateral position, body slip angle and yaw rate are already corrected in the right direction before $s = 175$, by a combination of a lower velocity and different timing of the longitudinal control inputs in the initial part of the turn. It can be seen again that the front lateral slip barely reacts to the disturbance: the steering angle simply compensates for the changes in β and $\dot{\psi}$, such that $\mathbf{s}_f \approx 1$.

The main conclusion is that with preview the trajectory is altered, such that the longitudinal control does not need to be reduced as much on the disturbed interval. Furthermore, it can be seen that without preview but with action the state trajectory deviates from the state trajectory. Hence, on $s = 185$ the problem can be seen as that of a perturbation to the state vector.

Figure 5-12 shows the result for the nominal solution, and the the solution without preview and action on the low-grip interval. For comparison, the solution without preview but with control on the perturbed interval is plotted again as well. Since the control inputs are freezed, the red lines show the natural response to the disturbance. As can be seen, both the body slip angle and yaw rate rise rapidly. The interval is followed by a large reduction in longitudinal force, and furthermore a decrease in front lateral slip. Again, these conditions are equivalent to those of a perturbation to the state vector at $s = 185$ and more extreme than in case some action is allowed. The perturbation to the state vector will as a condition for the next study, to systematically investigate the influence of a wide variety of perturbations on the reaction of the control input trajectories.

Table 5-3: Maneuver times of hairpin with local road friction reduction under various levels of preview and control

Conditions	J [s]	Rel. time loss %
Nominal solution	8.607	0
$F_M = 80\%$ for $175 \leq s < 185$, preview	8.667	0.7
$F_M = 80\%$ for $175 \leq s < 185$, no preview	8.692	0.9
$F_M = 80\%$ for $175 \leq s < 185$, no preview, no control	8.705	1.1
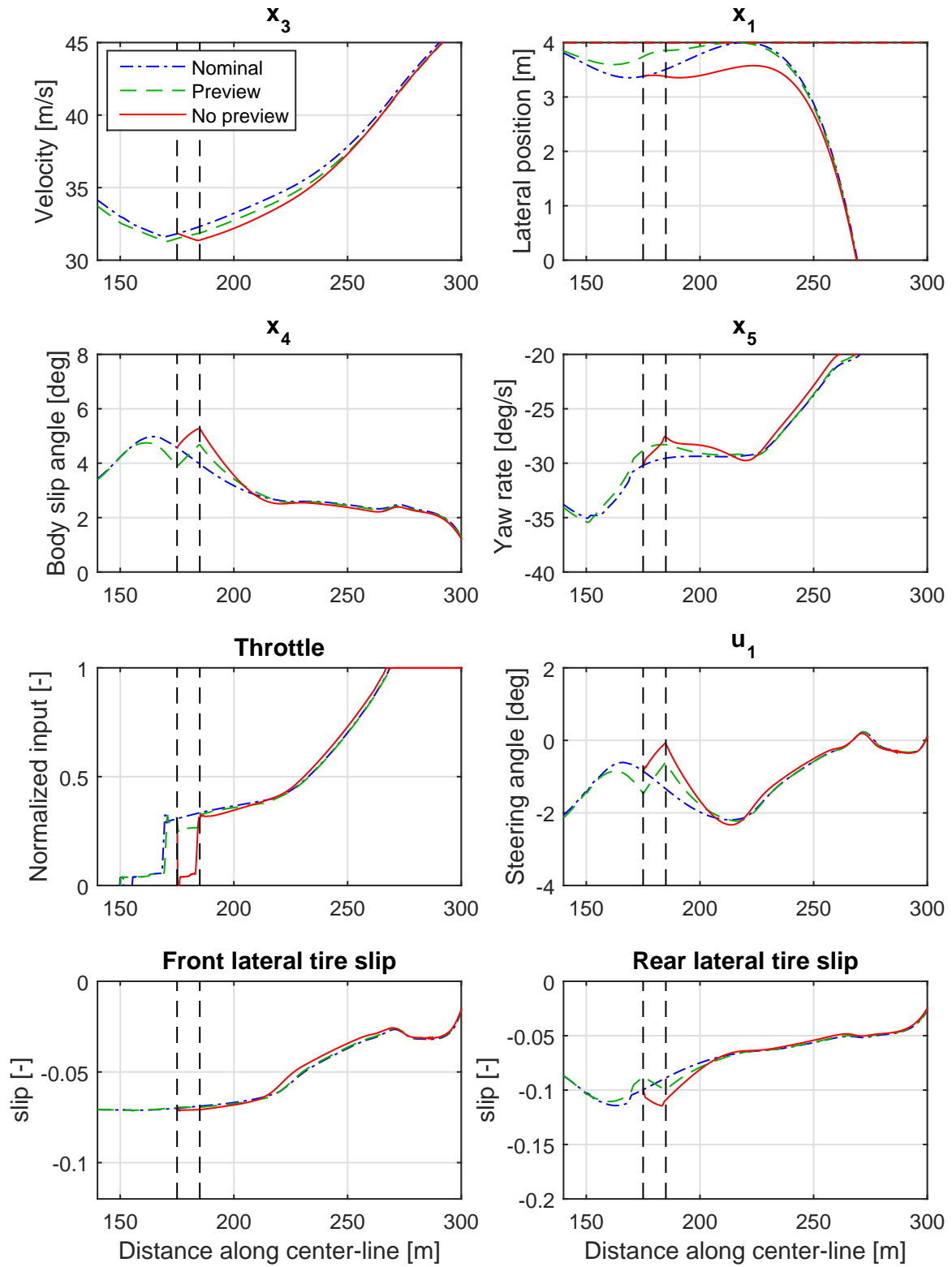
Figure 5-11: Results of hairpin with 10m long reduction of F_M to 80%. Nominal, with preview and without preview
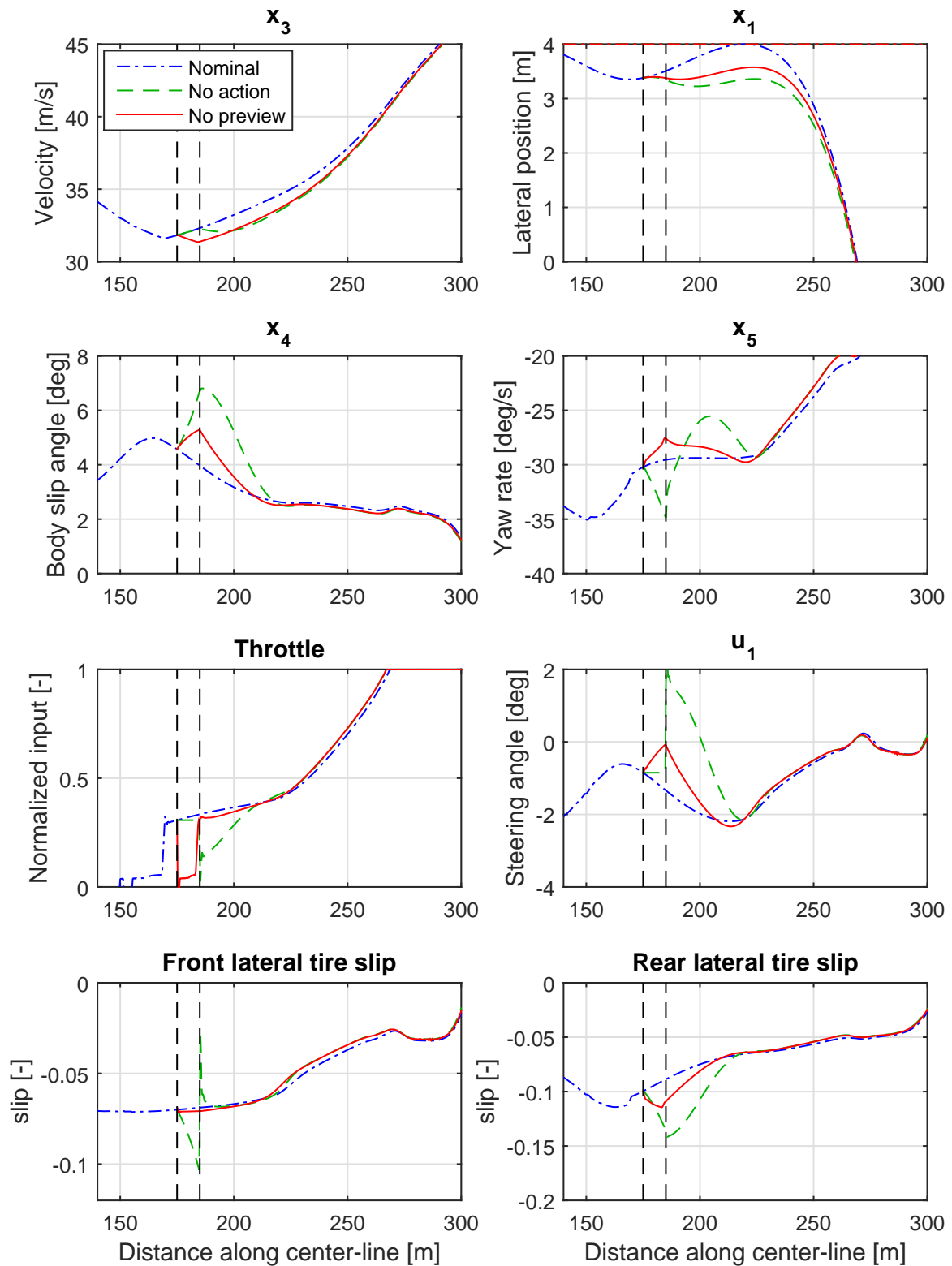
Figure 5-12: Results of hairpin with 10m long reduction of F_M to 80%. Nominal, with preview and without preview and control action.

5-4-2   Disturbance to state vector

In the previous study a special cause leading to a perturbation in the state vector was considered. In this study, a wider range of state perturbations is considered and no preview about the disturbance is assumed. The problem is initialized at $s = 175$, and the initial condition constraint (4-4) is defined as follows:

$$\Upsilon = x[1] - (x_n[k_s] + p) = 0 \qquad\qquad x_o, p \in \mathbb{R}^n \qquad (5\text{-}16)$$

Where $x_n[k_s]$ denotes the state of the solution to the nominal problem at $s = 175$m. p denotes a perturbation vector. Two different cases for p are considered. In the first case, a disturbance is applied to β, $\dot{\psi}$ and ξ. The disturbance to the vehicle orientation is equal to the disturbance to the body slip angle, hence:

$$p_1 = \begin{pmatrix} 0 & \beta_p & 0 & \beta_p & \dot{\psi}_p \end{pmatrix}^\top \qquad\qquad (5\text{-}17)$$

This means that the direction in which the vehicle moves is unchanged, but just the orientation of the vehicle relative to its direction of moving. Such a disturbance could result from e.g. a variation in driving on turn entry, leading to a different body slip angle. In the second case, only $\dot{\psi}$ and β are perturbed, hence:

$$p_2 = \begin{pmatrix} 0 & 0 & 0 & \beta_p & \dot{\psi}_p \end{pmatrix}^\top \qquad\qquad (5\text{-}18)$$

This means that the orientation of the vehicle itself has not changed, but rather the direction in which it is moving. Such a disturbance can be a result of a local reduction in tire-road friction or a crest in the track.

For the two cases, all combinations of the following disturbances are simulated.

$$\beta_p = -4, \quad -2, \quad 0, \quad 2, \quad 4, \quad 6 \qquad\qquad (5\text{-}19)$$
$$\dot{\beta}_p = -4, \quad -2, \quad 0, \quad 2, \quad 4 \qquad\qquad (5\text{-}20)$$

It should be noted that $\dot{\beta}$ is a state derivative instead of a state. To find $\dot{\psi}$ corresponding to a certain $\dot{\beta}$ the nonlinear equation solver `fsolve` from MATLAB was employed. This also included finding Γ_x and Γ_y such that the load transfer equations (3-16) and (3-17) are satisfied at the initial condition (5-16).

Examples   In Figure 5-14 the responses for $\beta_p = -4$ and $\beta_p = +6$ with $\dot{\beta}_p = 0$, for $\xi_p = 0$ is shown. Figure 5-15 shows the responses for $\dot{\beta}_p = -4$ and $\dot{\beta}_p = +4$ with $\beta_p = 0$, for $\xi_p = 0$ as well. It can be observed that the perturbed trajectory of $\dot{\psi}$ and β converge to the nominal solution within about 20m, in case of a disturbance to $\dot{\beta}$. Furthermore, negative perturbations to β and $\dot{\beta}$ lead to a briefly increased longitudinal control. A short reduction in front

lateral slip is observed in the first meter in case of a positive $\dot{\beta}$. Although this indicates that the front steering angle can be used for yaw-rate disturbances, it should be noted that this response might be too fast to be executed by a human driver.

Results The control action for all combinations of disturbances is shown in Figure 5-13. It displays the value of $s_{y,f}$ and throttle corresponding to the largest deviations from the nominal trajectory in the first 20m after the disturbance. The reason for this approach can be understood when observing Figure 5-14 and Figure 5-15: the point in distance s corresponding to the extreme deviation may differ per case. Going back to Figure 5-13, each point in the graphs of corresponds to the maximum deviation of $s_{y,f}$ or throttle at one single combination of β_p and $\dot{\beta}_p$. The two graphs on the left side correspond to a perturbation of type p_1, and the two graphs on the right side correspond to a perturbation of type p_2.

- For negative β_p and $\dot{\beta}_p$ the longitudinal control action is increased by multiple times. Inspecting the distance-based graphs in Figure 5-14 and Figure 5-15 learns that in these cases the longitudinal velocity is increased while bringing β and $\dot{\psi}$ back to the original trajectory. Going back to Figure 5-13, it is seen that the magnitude of this effect is similar for p_1 and p_2.

- For negative β_p and $\dot{\beta}_p$ the front lateral slip does not change, but is maintained at $\mathbf{s} \approx 1$. For positive β_p and $\dot{\beta}_p$, a combination of a reduction in longitudinal control and reduction in front lateral force is used to restore the trajectory. A reduction in throttle is employed as the first means to reject disturbances. However, as the throttle at the disturbance approaches its minimal value, an adjustment in $s_{y,f}$ is used in conjuction. This effect is most visible in case of a perturbation in $\dot{\beta}_p$. As can be seen in Figure 5-15, the duration of the $s_{y,f}$ reaction is short: a large negative yaw moment results in a rapidly decreasing yaw rate, where-after $\mathbf{s}_f \approx 1$ is maintained again. The influence of the inverse response of β to δ is not seen in this case, which may be caused by the simultaneous reduction in longitudinal control. Although is seen that the longitudinal control is the primary control input for rejecting disturbances, it can be said that the RHP in $H_1(s)$ is not significantly restrictive for disturbance rejection.

- Finally, there is a significant difference in distribution between control actions for the two perturbation types p_1 and p_2. For positive β_p, $\dot{\beta}_p$ and ξ_p, the front lateral slip is reduced more than in the case that ξ_p is not corrected (p_2). At the same time, the opposite counts for the longitudinal control action. Hence, if the direction of movement of the vehicle is perturbed the front lateral slip tends to stay longer at the optimum, and more of the disturbance is rejected by a reduction in longitudinal force. This indicates that the orientation of the vehicle is significantly influencing the distribution of control actions.
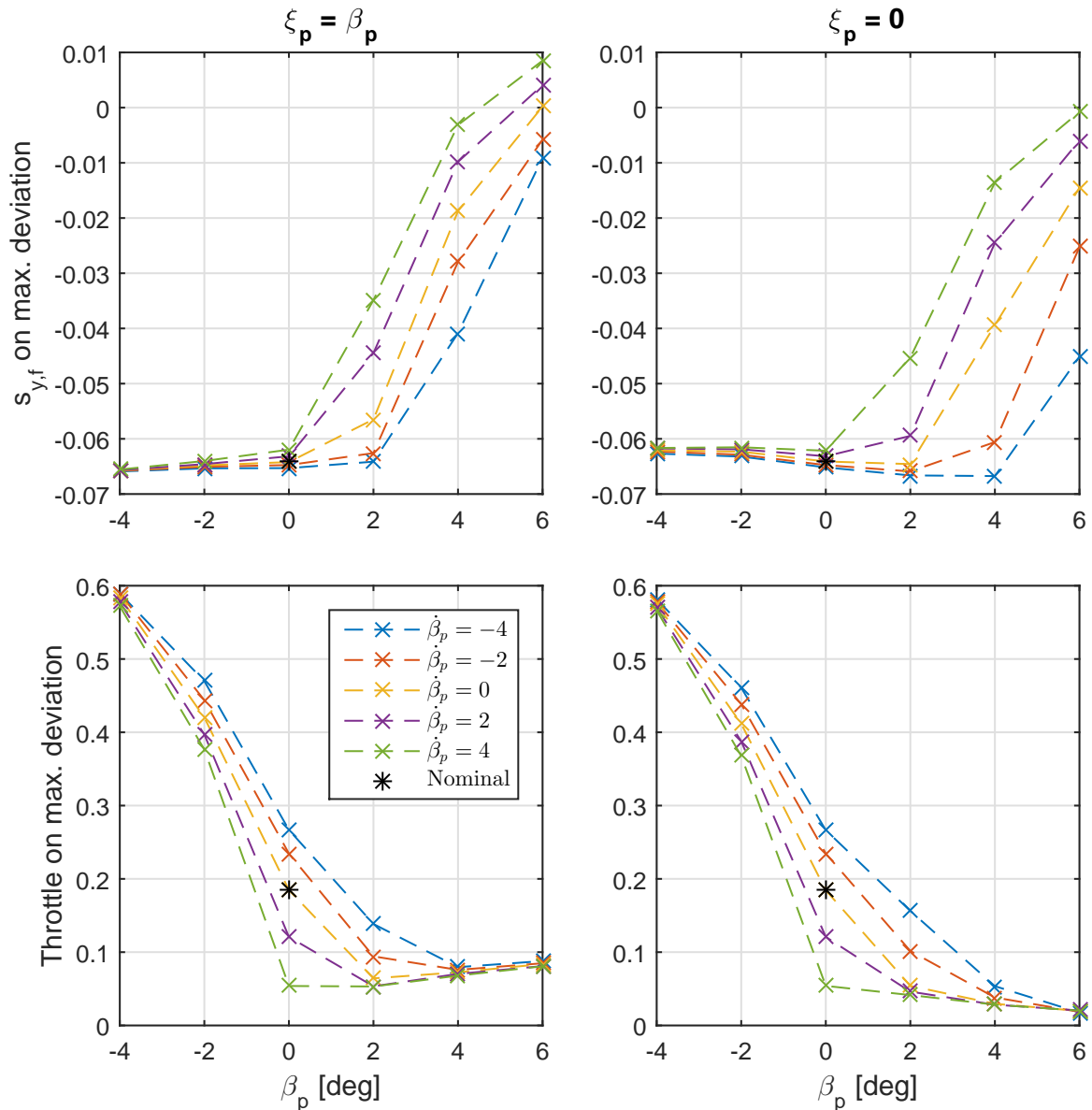
Figure 5-13: Overview of response magnitude of both control inputs to state disturbances. The black asterisks mark the nominal solution

5-4-3   Conclusions of disturbance study

The optimal rejection of disturbances was studied. For this, a distance interval with reduced maximal tire-road friction and a pure perturbation to the state vector were used, all for a 70m radius hairpin. The locally reduced maximal tire-road friction was used as an illustrative cause for a perturbation to the state vector. The main conclusion drawn from this case is that with preview of the local tire-road friction reduction, the state trajectory is corrected already before before the disturbance, resulting in a slightly lower velocity prior to it, but a reduced impact on the velocity after it. Not surprisingly, the overal maneuver time in case of

preview is lower than without preview.

For a combined perturbation to the body slip angle and yaw rate, it was shown that the throttle is the primary control input for rejection disturbances, but that the steering angle reacts in conjunction as soon as the throttle has reached a certain minimum, especially in case of large positive perturbations to body slip angle rate. In case of a simultaneous disturbance to the vehicle's orientation ξ and body slip angle β, a larger reduction in front lateral force is observed together with a smaller change in longitudinal control, even though the slip state of the vehicle is exactly the same. Unless it can be shown that this information can be derived from the steering angle δ, this leads to the conclusion that optimal longitudinal control requires information about ξ and n. It is recommended for future work to validate this hypothesis.

Future work   The perturbation study has led to the following new questions:

1. It was seen that the optimal response of steering angle takes place in a short time, before optimal front lateral slip is restored again. In reality this response may be impossible due to the time delay, limited bandwidth and steering velocity of the human driver. In a future study the human limitations could be included in the model, to see how the requirements for optimal longitudinal control change.

2. It was shown that the vehicle orientation influences the ratio of the lateral and longitudinal control response. As ξ and n are not available for TC, it is worth investigating if the optimal longitudinal control can be correlated to the steering angle and the states describing the motion of the vehicle instead.
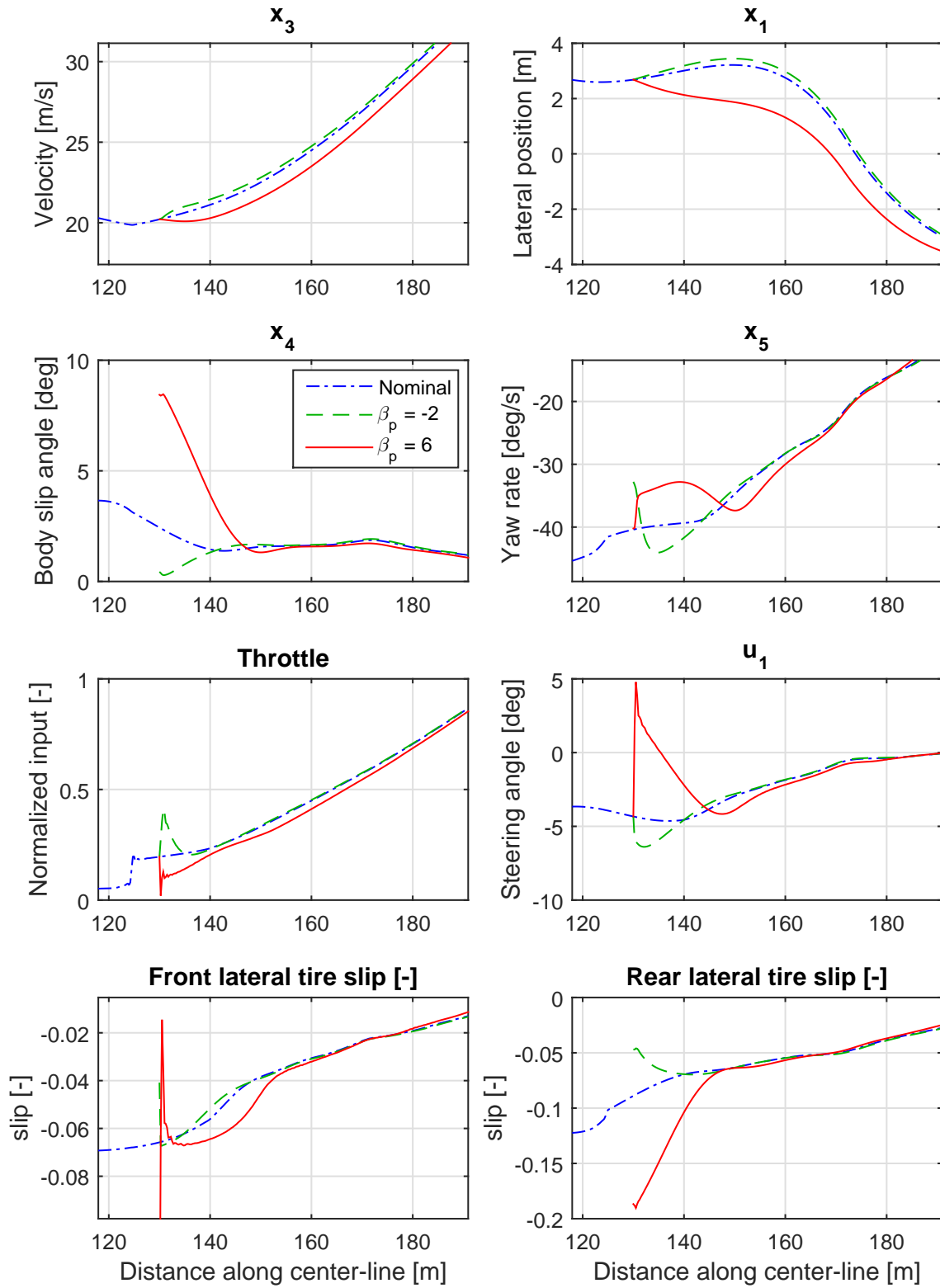
Figure 5-14: Response to disturbed β
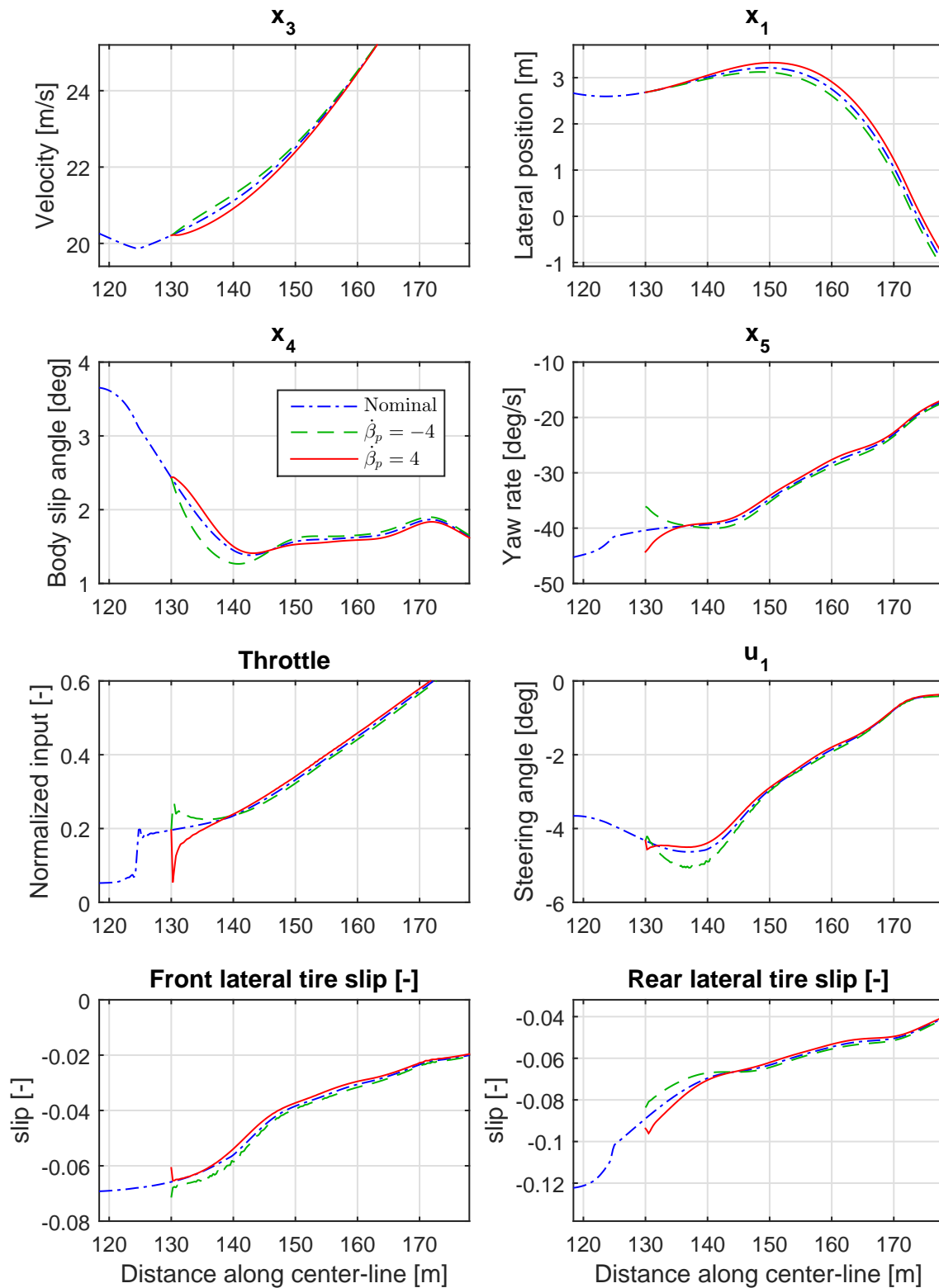
Figure 5-15: Response to disturbed $\dot{\beta}$

5-5 Conclusion

In this chapter three different simulation studies were described. In the first study, the modeling choice to neglect wheel rotational velocities was validated, by a comparison with a reference model which includes wheel rotational velocities. It was shown that both maneuver time and trajectory differences are negligible for the current vehicle model. Furthermore, it was shown that the artificial stability constraint on longitudinal slip prevents the solution to misuse the absence of the wheel dynamics.

In the second study, the nominal optimal control solution for a hairpin maneuver was studied on the basis of its relation to TC. It was shown that for the hairpin maneuver the friction for all four wheels is not used at all times. In general one of the axles is close to full tire force utilization, and the other is not. On a large interval of the solution, the axle with less than full utilization is overdriven, hence a tire slip of larger than the slip for maximum tire force is used. Furthermore, using Lyapunov's First Method it was shown that the optimal trajectory includes some intervals on which the yaw dynamics are locally unstable. An additional observation is that steering angle control on the majority of the turn only compensates for the influence of body slip angle and yaw rate changes on front lateral slip, to keep the front lateral slip at the value corresponding to maximal lateral force. Hence, the majority of the control of the dynamics is done by the longitudinal controls and timing of the control inputs during turn entry.

In reality, the trajectory of the vehicle may include some variations from repetition to repetition as a result of driver imprecision and disturbances to the vehicle. Therefore in the third study, the optimal reaction of the control inputs to disturbances was studied. First of all, the reaction to a local reduction in tire-road friction was compared for cases with and without preview. It was shown that for this particular case the preview led to a slightly lower velocity prior to the disturbance, combined with a reduction in yaw rate and body slip angle. However, after the disturbance the velocity is higher than without preview, due to the reduction in required reaction from throttle. In a more general study several combinations of perturbation to yaw rate and body slip angle have been applied. For a combined disturbance to these states, the longitudinal control is shown to be the primary control input for rejection disturbances, with the steering angle reacting in conjunction as soon as the longitudinal control has reached a certain minimum, especially in case of large positive perturbations to yaw rate. In case of a simultaneous disturbance to the vehicle's orientation ξ and body slip angle β, a larger reduction in front lateral force is observed together with a smaller change in longitudinal control, even though the slip state of the vehicle is exactly the same. This leads to the hypothesis that for optimal rejection of disturbances by TC, information about the orientation and lateral position of the vehicle is required. To the best knowledge of the author, a TC system using this information has not been implemented thus far, and as such this hypothesis is relevant to investigate in future studies.

In this chapter some proposals for future work regarding TC research using optimal control have been developed. First, it was shown that the rear axle is often overdriven during turn exit. However, in all cases, the overdriving had been initiated on turn entry. Practical

experience from the field has shown that human drivers do no often tend to overdrive the rear axle as much on turn entry, therefore it remains an unanswered question whether it is still time optimal to exceed $\mathtt{s}_r = 1$ on turn exit when overdriving did not occur on turn entry. Second, the longitudinal control appears to include a step wise increase on turn exit. Since it was shown that the dynamics during the majority of the turn are controlled by the longitudinal input, it is suspected that the magnitude of this step wise increase depends on the influence on yaw and lateral dynamics. Further research to the correlation of this step to variations in certain quantities can give additional information for time-optimal TC. It was shown that the longitudinal control is often the main means for rejecting disturbances. In case steering angle is used for disturbance rejection the control inputs are rather high-frequent. In reality, the human driver may not be able to supply this due to restrictions in bandwidth and delays. By including a human limitations in the model, the additional requirements this poses on TC could be studied. Finally, the ratio of longitudinal and lateral control in their reaction to disturbance was shown to be dependent on vehicle orientation. Since this measurement is not available for TC, it should be investigated whether the optimal amount of longitudinal control can be correlated to other states and the steering angle instead.

Chapter 6

Precision and Sensitivity

For simulation studies such as performed in Chapter 5 it is desirable to acquire a certain precision. That is, small variations in parameters or starting solution should not lead to disproportional differences in state trajectory. In Section 6-1 the precision is investigated by mapping the relation between mass and maneuver time. It is shown that there exist two classes of qualitatively different local minima, and that convergence to the one or the other minimum is influenced by small variations in mass. Two ways for improving the precision of the method are described. The first approach is the usage of inequality constraints reducing the solution space and the second approach is the usage of a warm-start. The results of both approaches is presented.

An important application of maneuver time simulation is to determine the maneuver time dependency on some key vehicle parameters, such as mass, power, aerodynamic downforce and drag. This information is used in determining vehicle set-up parameters, and is used for the plausibilization of test results in case of (known) variations to such parameters. In the framework of Minimal Time Maneuvering (MTM) methods, we are also interested in the variation of the optimal solution with small perturbations to parameters. The investigation of the change of the optimal solution with small perturbations to parameters is in this thesis defined as sensitivity study. The changes can be predicted by so-called sensitivity differentials. Methods for efficient calculation of sensitivity differentials are well developed. This thesis makes use of an existing theoretical framework for interior-point methods. An overview of the relevant literature and a brief introduction to the method are given in Section 6-2. As a proof of concept for the applicability of use of sensitivity differentials for the race car MTM, the method is applied in a small study of maneuver time sensitivity to vehicle mass. The results of this study are presented in Section 6-3.

6-1 Precision

The optimal solution may be affected by random errors as result of a finite-precision arithmetic operations. Furthermore, there is a certain tolerance on termination criteria, allowing all

solutions that are within these tolerances. Finally, for general nonlinear objective functions there could exist multiple local minima. Small variations in parameters or starting solution may lead to a convergence to a different solution even when infinite-precision and infinitely small tolerances would be used. In this section, an image of the combination of these three errors is formed. The metric we associate to precision is the relative standard deviation of the maneuver time, defined as:

$$\sigma_n = \frac{\sqrt{\dfrac{\sum\limits_{k=1}^{L} J^2[k] - E_J^2[k]}{L}}}{\dfrac{\sum\limits_{k=1}^{L} J[k]}{L}} \tag{6-1}$$

Where L is the number of optimization runs in the study. $J[k]$ and $E_J[k]$ denote the performance index and expected value of the performance index respectively. The latter is formed on the basis of all L solutions. Note that the general precision of the method cannot be assessed in this manner, but rather the precision of a certain study. The relative standard deviation for the maneuver time is considered, since this is assumed to contain the information of the most relevant states. We calculate σ_n for a variation in vehicle mass. This parameter is chosen because from physical properties it is known that an increase in vehicle mass should always increase maneuver time. The mass is varied in steps of 0.25 kg, in a range of 20 kg. In this range, the mass and maneuver time are assumed to have a linear relation. This forms the basis for the calculation of $E_J[k]$. The maneuver for the study is a 50 m radius hairpin, enclosed by two 100 m straight line sections.

Results   The result is shown in Figure 6-1. The first observation is the (expected) positive relation between mass and maneuver time. Second, it can be seen that there are two main solution classes, with a difference of approximately 0.01s between them. The nature of the difference between the solution classes can be seen from Figure 6-3, which contains the velocity, lateral position and rear lateral slip trajectories of all solutions. As can be seen there is a significant difference in body slip angle, yaw rate and velocity trajectory for the two solution classes. According to the definition given in Section 5-1 the rear axle is clearly overdriven for the faster local minimum. This corresponds to the conclusions given in Chapter 5. For the local minimum corresponding to the higher maneuver time, the rear axle is overdriven as well, but not as much. The velocity signal shows that the point of lowest velocity occurs around 8 m later for latter local minimum. The resulting relative standard deviation in maneuver time is equal to $\sigma_n = 5.8 \cdot 10^{-4}$.

6-1-1   Distance-dependent constraint

As was concluded in the previous paragraph the precision is decreased by the convergence of the method to two different local minima. As can be seen from Figure 6-3, the rear lateral slip $s_{y,r}$ trajectory for the two solution classes is significantly different around the middle of

Figure 6-1: Maneuver time for varying vehicle mass, hairpin maneuver

the maneuver, both qualitatively and quantitatively. In order to enforce solution class two, the following distance dependent constraint is added to the problem formulation:

$$g_4[i] = \phi[i](s_{y,r}[i] + 0.1) \leq 0 \tag{6-2}$$

$$\phi[i] = \begin{cases} 1 & \text{if} \quad 150 \leq s[i] \leq 170 \\ 0 & \text{otherwise} \end{cases} \tag{6-3}$$

For $i = 1 \quad ... \quad N$. Figure 6-3 shows a graphical representation of inequality constraint g_4. The result is shown in Figure 6-2. As can be seen, σ_n is decreased by around a factor ten with this additional constraint.

6-1-2 Exploiting IPOPT warm-start

An alternative approach for reducing the solution spread may be to initialize the optimization at a point closer to the solution. In the most extreme case, we may initialize problem (4-23) at the previous solution. We define the previous solution as the solution of the problem with a mass difference of 2.5 kg. Aside from the primal variables $\tilde{c}$, the full variable information of an interior-point solution includes the dual variables λ and Lagrange multipliers of decision variable upper and lower bounds, defined as z^L and z^U [39]. Initializing the optimization with the full-variable information from a previous solution is referred to as warm-start [44]. For the results in this study, the warm-start feature of IPOPT was exploited. The problem is now initialized as follows:

$$\tilde{c}_i = \bar{c}_k \tag{6-4}$$

$$\lambda_i = \bar{\lambda}_k \tag{6-5}$$

$$\tilde{c}_i^L = \bar{c}_k^L \tag{6-6}$$

$$\tilde{c}_i^U = \bar{c}_k^U \tag{6-7}$$

Where $\tilde{c}_i$, λ_i, $\tilde{c}_i^L$ and $\tilde{c}_i^U$ denote the full-state information for the starting solution, and $\bar{c}_k$, $\bar{\lambda}_k$, $\bar{c}_k^L$ and $\bar{c}_k^U$ the full-state information from the previous solution. The previous solution is defined as the solution of (4-23) with vehicle mass $m_k = m_i - 2.5$.

The results are displayed in Figure 6-2 as well. As can be seen, using warm-start leads to a further improvement in precision. The normalized standard deviation is in this case equal to $\sigma_n = 2.8 \cdot 10^{-6}$.
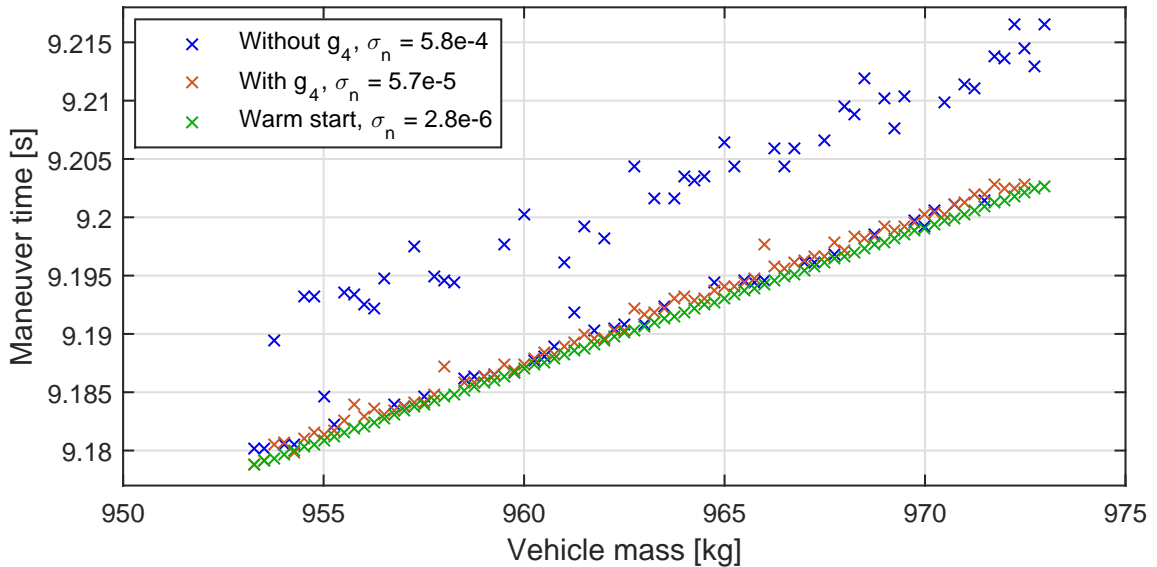
Figure 6-2: Maneuver time for varying vehicle mass, hairpin maneuver for three different approaches.

6-2 Parametric sensitivity for optimal control

In this work, sensitivity study is defined as the analysis of the influence of small parameter perturbations on the optimal solution. We approach this study by calculating so-called sensitivity differentials. The theory for the calculation of sensitivity differentials for parametric optimal control problems is well-developed. In the field of parametric sensitivity for optimal control the perturbations to the system are modeled by introducing parameters to the problem formulation. The theory relies on the implicit function theorem and the differentiability of the optimal solution with respect to the parameters. E.g. [45], [46] and [47] describe developments in the theoretic framework based on indirect methods. As already mentioned in Section 4,
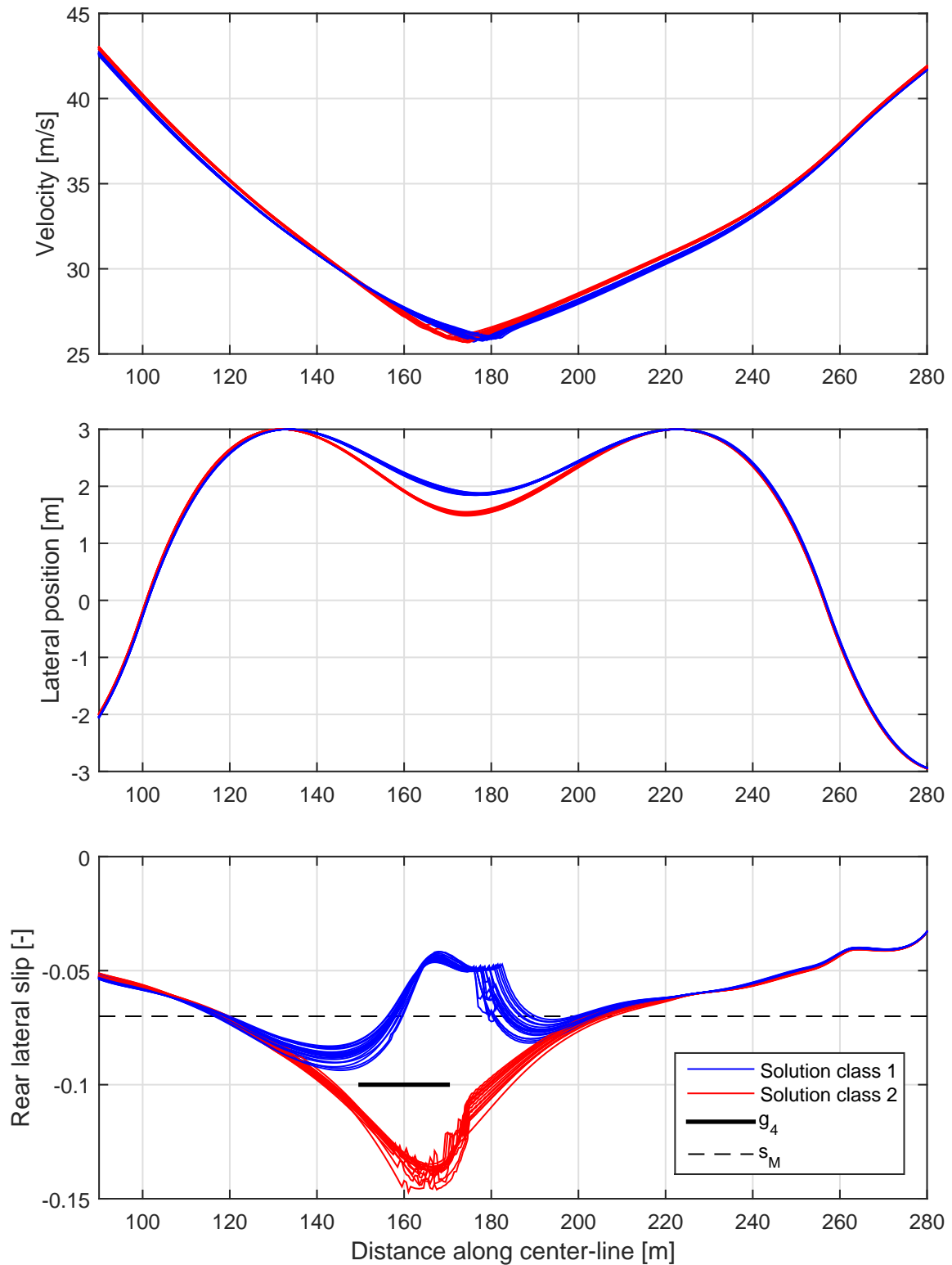
Figure 6-3: Velocity, lateral position and rear lateral slip as function of distance. The slower and faster solution classes are displayed in blue and red respectively.

indirect methods have the drawback that it implies the derivation of the necessary conditions for optimality, and furthermore that an initial guess of the trajectory of the adjoint variables and active set at the optimum are required. As an alternative, methods have been developed for parametric sensitivity using Non-Linear Programming (NLP) methods, for example in [48] and [49]. Essentially it is used that for a solution with suitable regularity conditions the sensitivity can be obtained by a linearization of the Karush-Kuhn-Tucker (KKT) conditions. The most recent implementation of parametric sensitivity to the barrier problem is described in [50]. The work builds on the advantage of the large-sparse capabilities of IPOPT, and has been implemented in the software package called sIPOPT. This software package is used for the application in this thesis.

6-2-1   Theoretical background on parametric sensitivity for interior-point methods

A brief overview of the theoretical background of parametric sensitivity for interior-point methods for NLP is presented here. This will be done on the hand of the description in [50]. For the full mathematical background the interested reader is referred to his work, and to the other references given in the previous paragraph.

Following the notation from Chapter 4, the following parametric nonlinear program is considered:

$$
\begin{aligned}
\min_{x} \quad & f(x, p) \\
\text{s.t.} \quad & c(x, p) = 0 \\
& x > 0
\end{aligned}
\tag{6-8}
$$

For this outline, no other inequality constraints than positive x have been assumed. The derivations are however extendable to upper bounds and nonlinear inequality constraints. IPOPT solves a sequence of the following barrier problems, with decreasing μ:

$$
\begin{aligned}
\min_{x} \quad & f(x, p) - \mu \sum_{i=1}^{m} \ln x \\
\text{s.t.} \quad & c(x, p) = 0
\end{aligned}
\tag{6-9}
$$

We are interested in the sensitivity differentials at the solution $p = p_0$, given by $\frac{\mathrm{d}x^*(p_0)}{\mathrm{d}p}$ and:

$$
\frac{\mathrm{d}f(x^*; p_0)^\top}{\mathrm{d}p} = \frac{\partial f(x^*; p_0)^\top}{\partial p} + \frac{\mathrm{d}x(p_0)^\top}{\mathrm{d}p} \frac{\partial f(x^*; p_0)^\top}{\partial x}
\tag{6-10}
$$

Where x^* denotes the value of x at the solution $p = p0$. The KKT conditions for this problem are given by:

$$\left.\begin{array}{rl} \nabla_x L(x^*, \lambda^*, \nu^*; p_0) = \nabla_x f(x^*, p_0) + \nabla_x c(x^*, p_0)\lambda^* - \nu^* &= 0 \\ c(x^*; p_0) &= 0 \\ XVe + \mu e &= 0 \end{array}\right\} \quad Q(s, p) = 0 \qquad (6\text{-}11)$$

Where X and V are diagonal matrices with the elements of x and ν on the diagonals, and $e \in \mathrm{R}^{n_x}$ a vector of ones. s denotes $s = \begin{bmatrix} x^\top & \lambda^\top & \nu^\top \end{bmatrix}$. Under certain conditions to the constraints and problem, it can be proven that the KKT conditions $Q(s, p) = 0$ become strong second order sufficient conditions for optimality. Furthermore, under the same assumptions the barrier sensitivity properties can be proven, which state that for $f(x; p)$ and $c(x; p)$ k times differentiable in p and $k + 1$ times differentiable in x:

- $x(\mu; p_0)$ is an isolated minimizer and the associated barrier multipliers $\lambda(\mu; p_0)$ and $\nu(\mu; p_0)$ are unique.

- For some p in the neighborhood of p_0 there exists a k times differentiable function:

$$s(\mu; p) = \begin{bmatrix} x(\mu; p)^\top & \lambda(\mu; p)^\top & \nu(\mu; p)^\top \end{bmatrix} \qquad (6\text{-}12)$$

    Corresponding to a locally unique minimum for (6-9).

- $\lim_{\mu \longrightarrow 0, p \longrightarrow p_0} s(\mu; p) = s(0, p_0) = s^*$

These properties form the basis for the remainder of the outline. For a proof and precise formulations of the conditions, the reader is referred to [50]. An important result however, is that all conditions can be checked for at the optimal solution from some information provided by IPOPT. This includes the inertia of the KKT matrix M which will be defined in the following.

The sensitivity differentials are now obtained by differentiating the KKT conditions using the Implicit Function Theorem:

$$\underbrace{\frac{\partial Q(s^*(p_0), p_0)}{\partial s}}_{M(s(\mu; p_0))} \left.\frac{\partial s}{\partial p}\right|_{p_0} + \underbrace{\frac{\partial Q(s^*(p_0), p_0)}{\partial p}}_{N_p(s(\mu; p_0))} = 0 \qquad (6\text{-}13)$$

The matrices M and N are given by:

$$M(s(\mu; p_0)) = \begin{pmatrix} W(s(\mu; p_0)) & A(x(\mu; p_0)) & -I \\ A(x(\mu; p_0)) & 0 & 0 \\ V(\mu; p_0) & 0 & X(\mu; p_0) \end{pmatrix} \qquad (6\text{-}14)$$

$$N_p(s(\mu; p_0)) = \begin{pmatrix} \nabla_{xp} L(s(\mu; p_0)) \\ \nabla c(x(\mu; p_0)) \\ 0 \end{pmatrix} \qquad (6\text{-}15)$$

Where $W(s(\mu; p_0))$ and $A(x(\mu; p_0))$ denote the Hessian of the Lagrangian and constraint Jacobian evaluated at $s(\mu, p_0)$ and $x(\mu, p_0)$. For the same a set of constraint qualifications that

turn the KKT conditions into sufficient conditions for optimality, the KKT matrix $M(s(\mu; p_0))$ is nonsingular. Hence, the sensitivity differential can be calculated as follows:

$$\frac{\mathrm{d}s(\mu; p_0)^\top}{\mathrm{d}p} = -M(s(\mu; p_0))^{-1} N_p(s(\mu; p_0)) \tag{6-16}$$

Note that this term already includes the required result $\frac{\mathrm{d}x^*(p_0)}{\mathrm{d}p}$. The state trajectory of the optimal solution of the perturbed problem can now be approximated using a Taylor expansion for small values of $\|p - p_0\|$:

$$x(p) = x(p_0) + \frac{\mathrm{d}x^*(p_0)}{\mathrm{d}p}(p - p_0) + o\|p - p_0\| \tag{6-17}$$

Where $o\|p - p_0\|$ denotes the unknown contribution of higher order terms in the expansion. The matrix M and N_p are directly available in IPOPT from the solution of (6-9). Hence, the sensitivity of a solution can be calculated with a small amount of additional calculations.

6-2-2 Implementation through sIPOPT

The theory described in the previous paragraphs is implemented in the sIPOPT package [50]. Interface with sIPOPT is currently only possible with AMPL [51]. For this study, therefore the problem (4-23) was reformulated in AMPL language. There are some differences compared to the implementation described in the rest of the thesis:

- The cost function gradient and constrained Jacobian are calculated using the automatic differentiation [52] feature implemented in AMPL, rather than by a finite-difference approximation.

- The warm-start and distance-dependent constraint features in the rest of the work have not been implemented in this version, due to the inexperience of the author with AMPL and the limited available time.

- Instead of the MA57-linear solvers available in the MATLAB implementation, only the MUMPS linear solver for internal IPOPT subproblems could be used. As stated in [44], this solver is less suitable for large-scale problems. This disadvantage was experienced during the implementation, and limited the problem size that could be handled with this version. As such, the sensitivity analysis in Section 6-3 was performed with a relatively large discretization interval of $h = 2$ m.

6-3 Results of sensitivity study

In this sensitivity analysis we consider the variation of maneuver time and state trajectory for small perturbations to the vehicle mass. The questions that are answered are as follows:

1. Does the sensitivity differential provide accurate information regarding the dependency of maneuver time on mass?

2. Does the approximated solution using sensitivity differentials satisfy all inequality constraints?

For answering the first question, we perform a similar study as in Section 6-1. The vehicle mass is varied over a range of 20 kg in steps of 0.25 kg. At each solution we calculate $\dfrac{\partial J}{\partial m}$ using the theory described in Section 6-2. The result from the sensitivity differential is compared to the trend obtained from the solutions at multiple values of m.

For answering the second question, we consider a rather large perturbation to vehicle mass of $\Delta m = 50$ kg. A variation in vehicle mass of such magnitude may occur during a race because of variations in the amount of fuel on board. From the sensitivity differentials, we calculate the approximated optimal state trajectories according to (6-17). Following on this, the nonlinear inequality constraints g and decision variable bounds are evaluated.

6-3-1   Dependency of maneuver time on mass

Figure 6-4 shows the maneuver time as well as the value of the cost sensitivity differential $\dfrac{\partial J}{\partial m}$ for a vehicle mass varying from 953 to 972 kg. As can be seen, the precision of this AMPL implementation is somewhat lower than for the MATLAB implementation of Section 6-1 with g_4. The value of $\hat{J}$ indicated by the red dashed line is obtained by integration of $\dfrac{\partial J}{\partial m}$ in the following manner:

$$\hat{J}[j] = J_{953} + \sum_{i=1}^{j} \frac{\partial J}{\partial m}[i](m[j] - m[j-1]) \tag{6-18}$$

Where J_{953} denotes the maneuver time at $m[0] = 953$ kg. Note that the integration handles variable mass step sizes. This is needed since some data points are missing from the results. The convergence of problem (4-23) with the AMPL implementation of IPOPT is somewhat less robust, due to the inexperience of the user with it and the limited available time. An interesting result however, is that the integrated performance $\hat{J}$, which is entirely based on the sensitivity differentials, is matching the trend observed from the nominal solutions over the mass range. Hence, even with paled precision due to the presence of several local minima, the sensitivity result is accurate.

6-3-2   Inequality constrained evaluation and qualitative solution study.

The theory described in Section 6-2-1 assumes the active-set along the trajectory to be invariant for a perturbation $\Delta p = p - p_0$. In the full parametric NLP however, a perturbation Δp may lead to an active set change, for which a positive variable becomes active at zero, or an active variable becomes positive [50]. Informally speaking: the linear approximation to the optimization problem may neglect bounds that are not active at p_0, or may satisfy bounds that are not active any more.

In this particular study, the feasibility is assessed for a perturbation to vehicle mass equal to
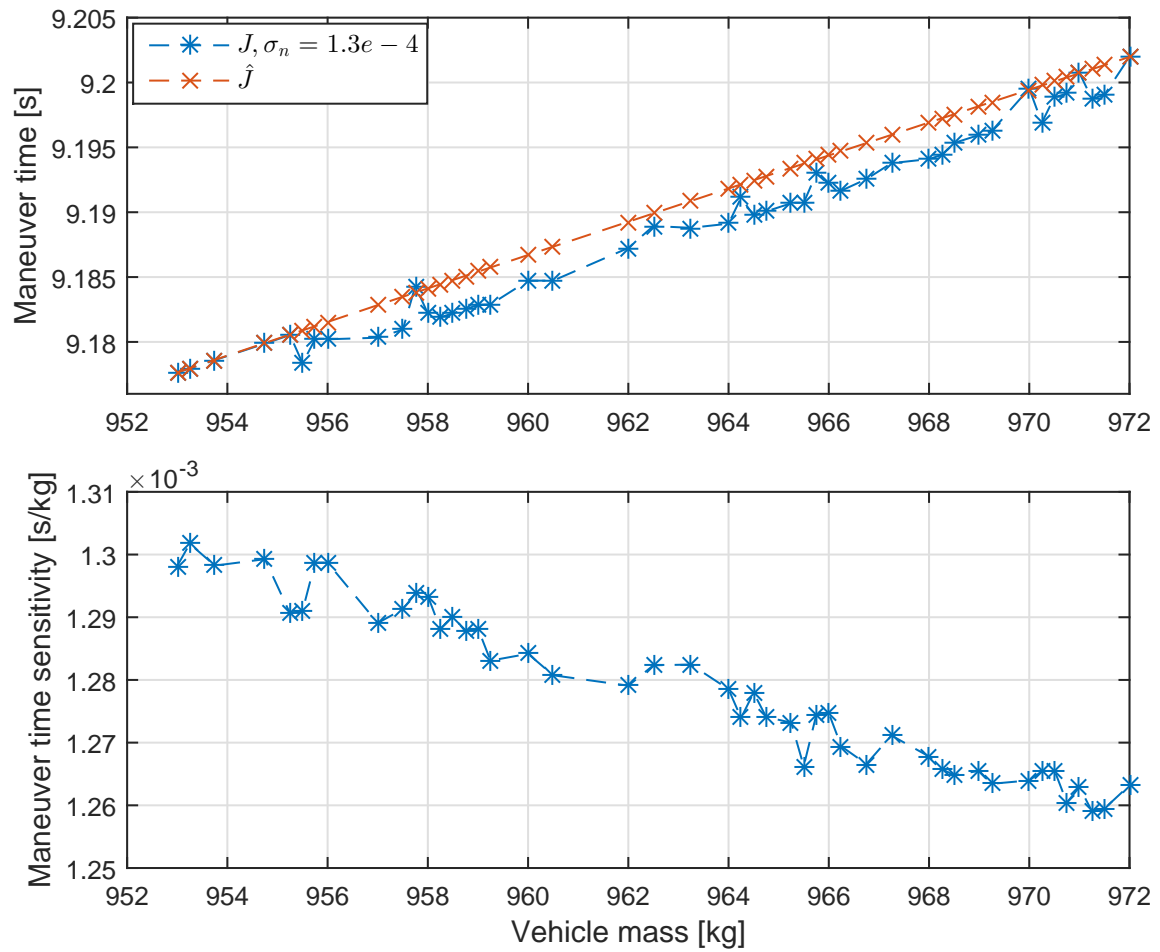
Figure 6-4: Maneuver time and maneuver time sensitivity with varying vehicle mass for a hairpin maneuver.

$\Delta m = 50$ kg. The results are shown in Figure 6-5. It shows the nominal trajectory and the approximation of the perturbed trajectory for a selection of states and inputs. The lower two graphs display the violation of respectively the lower and upper bounds of lateral position n, and the violation of the power constraint $g_1 < 0$. All other bounds and constraints were not violated at all in the approximated solution at $\Delta m = 50$ kg.

As can be seen, the lateral position bounds are violated for short distance intervals around $s = 65$ and $s = 220$. In both cases, the trajectory of n and $\bar{n}$ are slightly different prior to the point where n touches the bound. Since the interval on which the bound on n is active is very short, it is not surprising that the slightly different trajectory causes a mismatch in active set. The magnitude of the violation however stays below 1 cm, which is an acceptable level for a mass variation of 50 kg.
The power constraint g_1 is violated briefly around $s = 270$. Again, the violation occurs on a change of the active set. As can be seen, for the approximated solution with $\Delta m = 50$ kg the power constraint becomes active at an earlier point in distance. The magnitude of 0.002, corresponding to less than 1kW is accepted for this study.

Although the constraint violation due to active set changes was acceptable for this study, the effect may be of higher relevance for other parameters. Especially parameters which have a relatively high influence on the active set along the trajectory may be expected to cause inaccuracies. [50] handles this problem via a fix-relax strategy, using results from [53]. This is an efficient iterative strategy based on Schur complements. It is recommended for future work to implement this method.

6-4   Conclusion

This chapter discussed the precision of the method in predicting the influence of mass on maneuver time. Furthermore a sensitivity analysis using sensitivity differentials was performed. It was shown that imprecision is introduced as a result of converging to different local minima. Two qualitatively different local minima were found, with a maneuver time difference of only 0.1%. It was shown that using distance-dependent inequality constraints on rear lateral slip one of the cases can be excluded from the solution space, improving the precision of the method. Furthermore, the IPOPT warm-start feature was exploited to improve the precision by more than an order of magnitude. This confirms that the main contribution to method imprecision is the presence of multiple local minima which the solver is likely to converge to.

A proof of concept-like sensitivity study was performed using existing theory for parametric sensitivity for barrier methods. For this, the software package sIPOPT, interfaced with the language AMPL was implemented. For the proof of concept, the vehicle mass was taken as the variable parameter. The result of the sensitivity differential appeared to be in good accordance with the sensitivity to mass from the precision experiment. It was shown that at some active set changes the upper and lower bounds on lateral position and the upper bound on power are violated. This behavior is inherent to the principle behind the calculation of sensitivity differentials. For future work it is recommended to exploit the fix-relax strategy
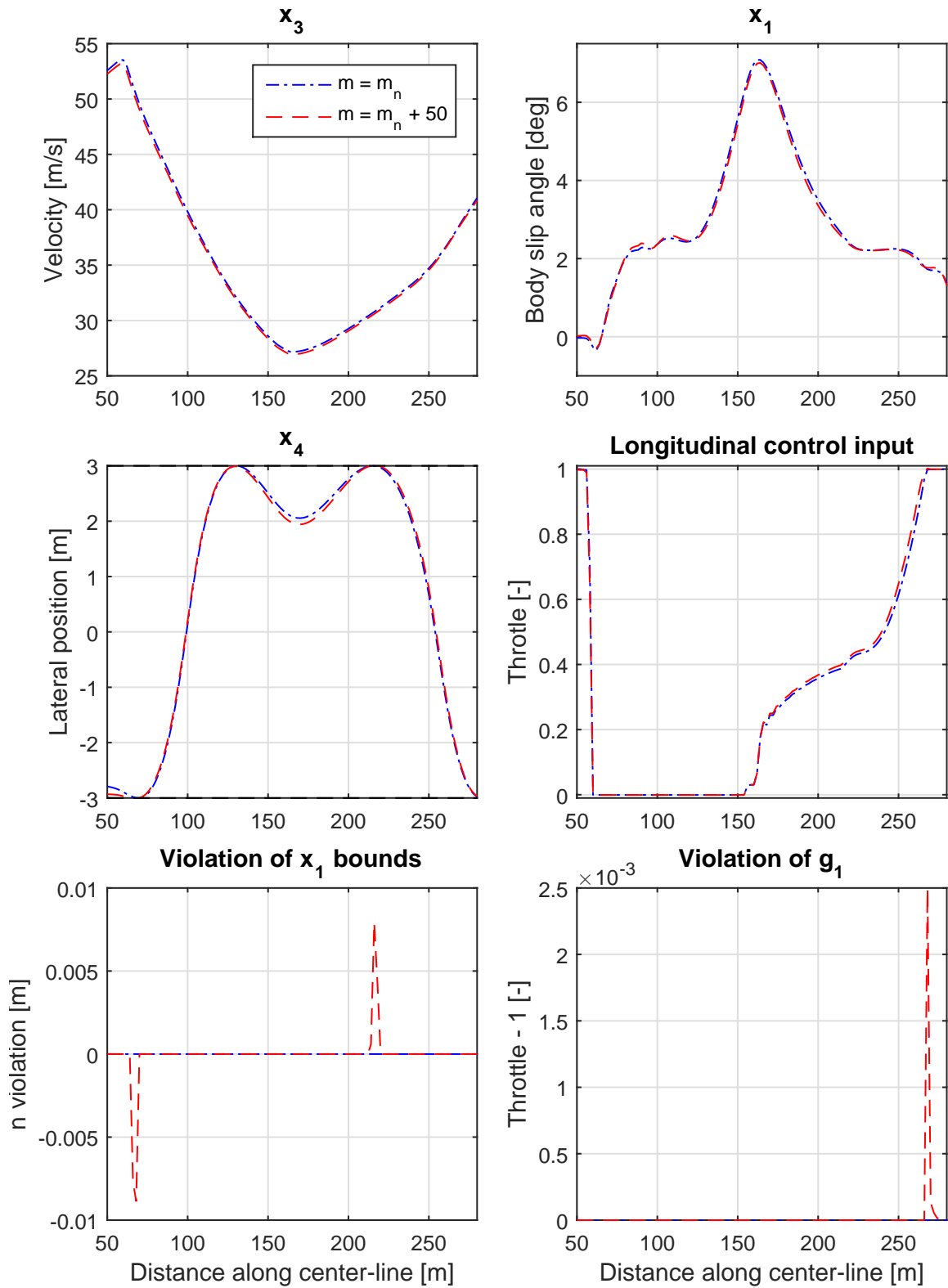
Figure 6-5: State trajectory for nominal solution and approximated solution at $\Delta m = 50$. The bound violations for the approximated solution are displayed in the lower two graphs.

which is implemented in sIPOPT, especially in parametric sensitivity analysis for parameters which have a relatively large influence on the intervals on which inequality constraints are active.

Chapter 7

Conclusion and recommendations for future work

This thesis described the implementation and application of a time-minimal trajectory generation method using optimal control. A direct collocation method was applied, using B-splines to represent control input and state trajectories. For solving the resulting nonlinear program, the IPOPT and SNOPT solvers have been compared. The model was based on a study of the influence of modeling alternatives on steady-state acceleration limits and dynamic properties. Using the described method, some case studies related to Traction Control (TC) systems have been performed. In addition, the precision of the method under certain conditions was assessed. Finally, a sensitivity study using so-called sensitivity differentials was performed.

Summary of contributions

- Different modeling alternatives have been compared based on their completeness for a qualitative study of the optimal control inputs. This was indicated by the influence of a modeling method on steady-state acceleration potential and potential yaw moment, and by the influence on the eigenvalues of the linearized dynamics under various longitudinal accelerations.

- The minimal time trajectory planning problem is formulated as an optimal control problem, which is discretized following the full collocation method where the state and input trajectories are parameterized in terms of B-spline coefficients. The integration of the equations of motion is approximated by the trapezoidal rule. The dynamics are formulated with distance as independent variable, and a curvilinear coordinate system is used.

- The SQP method SNOPT and interior-point method IPOPT have been compared based on their suitability for the race car Optimal Control Problem (OCP) on various maneuver lengths and discretization intervals. The precision of the resulting method in predicting maneuver time dependency on vehicle mass was assessed.

- The wheel rotational velocities are omitted from the state vector. Instead, tire longitudinal slip is included in the state vector. The hydraulic brake system and mechanical differential characteristics are satisfied by three independent algebraic equality constraints, resulting in one degree of freedom for the longitudinal control. The wheel rotational velocity is restricted to the velocity corresponding to stable wheel dynamics by additional inequality constraints. The presented formulation is validated using a reference model which does include wheel rotational velocities.

- The hairpin maneuver was studied in depth for three different corner radii. Questions regarding tire friction utilization, overdriving and vehicle stability which are relevant to TC were answered.

- A perturbation study was done, in which the reaction to a local reduction in tire-road friction with and without preview was compared. In addition, the time-optimal reaction of steering angle and longitudinal control for perturbations to the yaw rate, body slip angle and orientation compared to the nominal optimal trajectory is studied.

- A proof of concept of the applicability to the race car MTM of the use of sensitivity differentials for performing parametric sensitivity studies.

7-1   Summary of conclusions

The thesis makes the following conclusions:

- Longitudinal load transfer, lateral load transfer, aerodynamic downforce and a limited-slip differential have a significant influence on steady-state acceleration limits, potential yaw moment, and on eigenvalues at various longitudinal accelerations for the parameters used in this study. As such, these effects have to be included for a qualitative study of the optimal control input.

- Omitting wheel rotational velocities from the state vector does not result in a significant difference in trajectory of the other states if constraints are incorporated to represent the wheel stability boundaries.

- With the OCP formulated as a Nonlinear Program as described in the previous paragraph, using sparse-finite differencing for the constraint Jacobian calculation and using the IPOPT solver results in a method which can be used as a fast and robust analysis tool. That is, a maneuver with a length of 400m discretized on a 1m grid takes less than one minute to solve. With the inclusion of distance-dependent inequality constraint on rear lateral slip, a precision of 0.006% in predicting maneuver time dependency on vehicle mass was achieved.

- For this application, the interior-point solver IPOPT is clearly superior over the SQP solver SNOPT for problems with 1000 decision variables or more.

- For a hairpin maneuver the peak friction potential for all four wheels is not utilized at all times. In general one of the axles utilizes the full tire friction, and the other does not. On a large interval of the solution, the axle with less than full utilization

is overdriven, hence a tire slip of larger than the slip for maximum tire force is used. The optimal trajectory includes some intervals on which the yaw dynamics are locally unstable. The control of the dynamics during the major part of the turn is done by the longitudinal controls and timing of the control inputs during turn entry. The steering angle trajectory mainly compensates for the influence of body slip angle and yaw rate on front lateral slip, aiming to the front lateral slip at the value corresponding to maximal lateral force.

- A temporary reduction in tire-road friction leads to a lower velocity prior to the disturbance, combined with a reduction in yaw rate and body slip in case preview is provided. When preview is omitted, the reaction of longitudinal control to the reduction is multiple times larger, leading to lower velocity after the disturbance than in the case with preview. For a combined disturbance on yaw rate and body slip angle, the longitudinal control is the primary control input for rejecting disturbances, with the steering angle reacting in conjunction as soon as the longitudinal control has reached a certain limit. In case of a simultaneous disturbance on the vehicle's orientation and body slip angle, a larger reduction in front lateral force is observed together with a smaller change in longitudinal control, even though the slip state of the vehicle is exactly the same. This indicates that for time-minimal disturbance rejection, information about the vehicle's orientation relative to the road is needed for TC.

- The sensitivity of maneuver time to vehicle mass can accurately be estimated by the calculation of sensitivity differentials using internal information from IPOPT, when the mass is included as decision variable. This approach however leads to small bound violations in situations where the active set changes.

7-2   Recommendations for future work

In the following, recommendations for future work are listed. These do not just include suggested improvements to the method, but also new applications for it.

Roll and pitch dynamics One of the arguments for neglecting suspension dynamics was the assumption that optimal circuit driving is smooth enough to not excite the roll and pitch dynamics. The optimal solution however often shows a step wise increase in longitudinal control on turn exit. Studying this non-smooth phenomenon more closely may require the inclusion of a pitch degree of freedom. Furthermore, turn entry showed some high-frequency yaw oscillations induced by the steering angle. This indicates that it is worth investigating whether or not turn entry changes significantly with the inclusion of a roll degree of freedom.

Restrictions on rear lateral slip It was shown that the rear axle is often overdriven during turn exit. However, in all cases this was already initiated on turn entry. Practical experience from the field has shown that human drivers do no often tend to overdrive the rear axle as much on turn entry, therefore it remains an unanswered question whether it is still time optimal to exceed $s_r = 1$ on turn exit when overdriving did not occur on turn entry. It was already found that inequality constraints on the rear lateral slip over

a certain distance interval work well. This can be employed to induce a more realistic driving behavior on turn entry.

Correlation of initial release to yaw moment The throttle appears to include a step-wise increase on turn exit. Since it was shown that all control of dynamics throughout the majority of a turn happens through the brake and throttle, it is suspected that the magnitude of this step-wise increase depends on the influence on yaw and lateral dynamics. Further research on the correlation of this step to variations in quantities such as velocity can give additional information for time-optimal TC.

Incorporate human limitations It was shown that the longitudinal control is often the main means for rejecting disturbances. However, in the case where steering angle is used for disturbance rejection, the control input is rather high-bandwidth. In reality, the human driver may not be able to supply this control input due to limited reaction time and a limited rate of change of steering angle. By including human limitations in the model, the additional requirements this poses on TC could be studied.

Correlation of optimal longitudinal reaction to steering angle In simulation study 3 it was shown that the ratio of longitudinal and lateral control in their reaction to disturbance is dependent on vehicle orientation. Since vehicle orientation measurement is not available for current TC systems, it is worth investigating whether the optimal amount of longitudinal control can be correlated to the steering angle and other states instead.

Adaptive grid refinement There exist reliable adaptive grid refinement algorithms which find the required mesh size in an iterative fashion using a local error estimation [27], [41], [42]. This type of method rules out the need to assess accuracy for each problem manually, and is more efficient if longer maneuvers with long straight-line sections requiring a less fine grid are to be solved.

Alternative SQP solver The WORHP solver for Non-Linear Programming (NLP) could be tried as an alternative SQP method. Although solver SNOPT was shown to be not competitive with interior-point method IPOPT, WORHP is said to be suitable for very large (or even huge) problems. This is worth trying, to see if the benefits of Sequential Quadratic Programming (SQP) methods in the presence of nonlinear constraints and a relatively small amount of free variables can be exploited.

Fix-relax strategy for bound violation in parametric sensitivity study As was shown, the approximated solution by the sensitivity differentials leads to violation of variable bounds and nonlinear inequality constraints. It is recommended to exploit the fix-relax strategy which is implemented in sIPOPT, for robustness in parametric sensitivity analysis in case parameter variations have a large influence on the length of constrained arcs.

Appendix A

Vehicle models

A-1 Subscripting system

The subscript *f*, *r* denote the front and rear axle respectively. The subscripts *fl*, *fr*, *rl*, *rr* denote the front-left, front-right, rear-left and rear-right wheel respectively.

The subscript x, y and z indicate the value of the quantity (for example velocity or Force) projected on the respective axis of the Cartesian system. Unless the superscript T is used for the local tire frame, the frame is always the local vehicle coordinate system.

When subscripts are combined, they are separated by a comma. $F_{x,fl}$ for example indicates the force in x-direction on the front-left tire.

A-2 Single-track model

In this section, the single-track vehicle model used in Section 2 is described. The states and control inputs are defined as:

$$x = \begin{pmatrix} V & \beta & \dot{\psi} & \omega_f & \omega_r \end{pmatrix}^\top \tag{A-1}$$

$$u = \begin{pmatrix} \delta & T \end{pmatrix}^\top \tag{A-2}$$

With T the total wheel torque excluding engine drag torque, ω_f and ω_r the front and rear wheel rotational velocities and the other variables as shown in Figure 2-1. The state derivatives are given by:

$$\dot{V} = \frac{F_x \cos\beta + F_y sin\beta - F_d}{m} \tag{A-3}$$

$$\dot{\beta} = \dot{\psi} + \frac{F_y \cos\beta - F_x \sin\beta}{mV} \tag{A-4}$$

$$\ddot{\psi} = \frac{M_z}{I_{zz}} \tag{A-5}$$

$$\dot{\omega}_f = T_f - R_l F_{x,f} \tag{A-6}$$

$$\dot{\omega}_r = T_r - R_l F_{x,r} \tag{A-7}$$

With vehicle mass m and yaw moment of inertia I_z, and tire loaded radius R_l. The forces and moments acting on the vehicle body are composed as follows:

$$F_x = F_{x,f} \cos\delta - F_{y,f} \sin\delta + F_{x,r} \tag{A-8}$$

$$F_y = F_{x,f} \sin\delta + F_{y,f} \cos\delta + F_{y,r} \tag{A-9}$$

$$M_z = l(1 - d_m)(F_{x,f} \sin\delta + F_{y,f} \cos\delta) - l d_m F_{y,r} \tag{A-10}$$

With wheel base l and weight distribution d_m. The longitudinal and lateral velocity at the wheel in vehicle coordinates are given by:

$$v_x = V \cos\beta \tag{A-11}$$

$$v_y = V \sin\beta \tag{A-12}$$

$$v_{x,f} = v_x \tag{A-13}$$

$$v_{y,f} = v_y + l_f \dot{\psi} \tag{A-14}$$

$$v_{x,r} = v_x \tag{A-15}$$

$$v_{y,r} = v_y - l_f \dot{\psi} \tag{A-16}$$

Expressed in tire coordinates:

$$v_{x,f}^T = v_{x,f} \cos\delta + v_{y,f} \sin\delta \tag{A-17}$$

$$v_{y,f}^T = v_{y,f} \cos\delta - v_{x,f} \sin\delta \tag{A-18}$$

$$v_{x,r}^T = v_{x,r} \tag{A-19}$$

$$v_{y,f}^T = v_{y,r} \tag{A-20}$$

The lateral and longitudinal tire slip are calculated by:

$$s_{x,f} = \frac{\omega_f R_{\text{eff}} - v_{x,f}^T}{\omega_f R_{\text{eff}}} \tag{A-21}$$

$$s_{y,f} = -\frac{v_{y,f}^T}{v_{x,f}^T} \tag{A-22}$$

$$s_{x,r} = \frac{\omega_r R_{\text{eff}} - v_{x,r}^T}{\omega_r R_{\text{eff}}} \tag{A-23}$$

$$s_{y,r} = -\frac{v_{y,r}^T}{v_{x,r}^T} \tag{A-24}$$

With tire effective rolling radius R_{eff}. From the tire slip and vertical force the tire planar forces can be calculated:

$$(F_{x,f}, F_{y,f}) = F(s_{y,f}, s_{x,f}, F_{z,f}) \tag{A-25}$$

$$(F_{x,r}, F_{y,r}) = F(s_{y,r}, s_{x,r}, F_{z,r}) \tag{A-26}$$

$$\tag{A-27}$$

Where f denotes the TMeasy tire model, given by [25], p59. The vertical force on the tires is given by:

$$F_{z,f} = mgd_m - \frac{F_x h_{cg}}{l} + F_l d_l \tag{A-28}$$

$$F_{z,r} = mg(1 - d_m) + \frac{mF_x h_{\text{cg}}}{l} + F_l(1 - d_l) \tag{A-29}$$

$$\tag{A-30}$$

With wheelbase l, vehicle mass m, center of gravity height h_{cg}. The weight and aerodynamic downforce are distributed over the axles by d_l and d_m. Note that in case of neglecting longitudinal load transfer, h_{cg} is assumed equal to zero.

The aerodynamic drag F_d and downforce F_l in N are given by:

$$F_d = 0.5\rho C_d A V^2 \tag{A-31}$$

$$F_l = 0.5\rho C_l A (V \cos\beta)^2 \tag{A-32}$$

Where $C_d A$ and $C_l A$ are the drag and downforce coefficient times the frontal area, and ρ the air density. Finally, the wheel torques for the rear wheel drive model are defined as follows:

$$T_f = \begin{cases} 0 & \text{if } T \geqslant 0 \\ d_T T & \text{otherwise} \end{cases} \tag{A-33}$$

$$T_r = \begin{cases} T & \text{if } T \geqslant 0 \\ (1 - d_T)T & \text{otherwise} \end{cases} \tag{A-34}$$

With d_T the brake torque distribution.

A-3 Two-track model

In this section, the two-track vehicle model as used in this thesis is described. The states and control inputs are defined as:

$$x = \begin{pmatrix} V & \beta & \dot{\psi} & \omega_{fl} & \omega_{fl} & \omega_{rl} & \omega_{rr} \end{pmatrix}^\top \tag{A-35}$$

$$u = \begin{pmatrix} \delta & T \end{pmatrix}^\top \tag{A-36}$$

With T the total wheel torque, ω_{fl}, ω_{fr}, ω_{rl} and ω_{rr} the wheel rotational velocities and the other variables as shown in Figure 2-1. The state derivatives are given by:

$$\dot{V} = \frac{F_x \cos \beta + F_y \sin\beta - F_d}{m} \tag{A-37}$$

$$\dot{\beta} = \dot{\psi} + \frac{F_y \cos \beta - F_x \sin \beta}{mV} \tag{A-38}$$

$$\ddot{\psi} = \frac{M_z}{I_{zz}} \tag{A-39}$$

$$\dot{\omega}_{fl} = T_{fl} - R_l F_{x,fl} \tag{A-40}$$

$$\dot{\omega}_{fr} = T_{fr} - R_l F_{x,fr} \tag{A-41}$$

$$\dot{\omega}_{rl} = T_{rl} - R_l F_{x,rl} \tag{A-42}$$

$$\dot{\omega}_{rr} = T_{rr} - R_l F_{x,rr} \tag{A-43}$$

With vehicle mass m and yaw moment of inertia I_z, and tire loaded radius R_l. The forces and moments acting on the vehicle body are composed as follows:

$$F_x = (F_{x,fl} + F_{x,fr}) \cos \delta - (F_{y,fl} + F_{y,fr}) \sin \delta + (F_{x,rl} + F_{x,rr}) \tag{A-44}$$

$$F_y = (F_{x,fl} + F_{x,fr}) \sin \delta + (F_{y,fl} + F_{y,fr}) \cos \delta + (F_{y,rl} + F_{y,rr}) \tag{A-45}$$

$$M_z = l(1 - d_m)((F_{x,fl} + F_{x,fr}) \sin \delta + (F_{y,fl} + F_{y,fr}) \cos \delta) - l d_m F_{y,rl} + F_{y,rr})$$
$$+ ((F_{x,fl} - F_{x,fr}) \cos \delta - (F_{y,fl} - F_{y,fr}) \sin \delta + F_{x,rl} - F_{x,rr}) \frac{\nu}{2} \tag{A-46}$$

With wheel base l, track width ν and weight distribution d_m. The longitudinal and lateral velocity at the wheel in vehicle coordinates are given by:

$$v_x = V \cos \beta \tag{A-47}$$

$$v_y = V \sin \beta \tag{A-48}$$

$$v_{x,fl} = v_x + \frac{\nu}{2}\dot{\psi} \tag{A-49}$$

$$v_{x,fr} = v_x - \frac{\nu}{2}\dot{\psi} \tag{A-50}$$

$$v_{y,f} = v_y + l_f\dot{\psi} \tag{A-51}$$

$$v_{x,rl} = v_x + \frac{\nu}{2}\dot{\psi} \tag{A-52}$$

$$v_{x,rr} = v_x - \frac{\nu}{2}\dot{\psi} \tag{A-53}$$

$$v_{y,r} = v_y - l_f\dot{\psi} \tag{A-54}$$

Expressed in tire coordinates:

$$v_{x,fl}^T = v_{x,fl}\cos\delta + v_{y,fl}\sin\delta \tag{A-55}$$

$$v_{x,fr}^T = v_{x,fr}\cos\delta + v_{y,fr}\sin\delta \tag{A-56}$$

$$v_{y,f}^T = v_{y,f}\cos\delta - v_{x,f}\sin\delta \tag{A-57}$$

$$v_{x,rl}^T = v_{x,rl} \tag{A-58}$$

$$v_{x,rr}^T = v_{x,rr} \tag{A-59}$$

$$v_{y,f}^T = v_{y,r} \tag{A-60}$$

The lateral and longitudinal tire slip are calculated by:

$$s_{x,fl} = \frac{\omega_{fl}R_{\text{eff}} - v_{x,fl}^T}{\omega_{fl}R_{\text{eff}}} \tag{A-61}$$

$$s_{x,fr} = \frac{\omega_{fr}R_{\text{eff}} - v_{x,fr}^T}{\omega_{fr}R_{\text{eff}}} \tag{A-62}$$

$$s_{x,rl} = \frac{\omega_{rl}R_{\text{eff}} - v_{x,rl}^T}{\omega_{rl}R_{\text{eff}}} \tag{A-63}$$

$$s_{x,rr} = \frac{\omega_{rr}R_{\text{eff}} - v_{x,rr}^T}{\omega_{rr}R_{\text{eff}}} \tag{A-64}$$

$$s_{y,fl} = -\frac{v_{y,fl}^T}{v_{x,fl}^T} \tag{A-65}$$

$$s_{y,fr} = -\frac{v_{y,fr}^T}{v_{x,fr}^T} \tag{A-66}$$

$$s_{y,rl} = -\frac{v_{y,rl}^T}{v_{x,rl}^T} \tag{A-67}$$

$$s_{y,rr} = -\frac{v_{y,rr}^T}{v_{x,rr}^T} \tag{A-68}$$

With tire effective rolling radius R_{eff}. From the tire slip and vertical force the tire planar forces can be calculated:

$$(F_{x,fl}, F_{y,fl}) = F(s_{y,fl}, s_{x,fl}, F_{z,fl}) \tag{A-69}$$

$$(F_{x,fr}, F_{y,fr}) = F(s_{y,fr}, s_{x,fr}, F_{z,fr}) \tag{A-70}$$

$$(F_{x,rl}, F_{y,rl}) = F(s_{y,rl}, s_{x,rl}, F_{z,rl}) \tag{A-71}$$

$$(F_{x,rr}, F_{y,rr}) = F(s_{y,rr}, s_{x,rr}, F_{z,rr}) \tag{A-72}$$

$$\tag{A-73}$$

Where F denotes the tire model, described in [25], p59. The vertical force on the tires is given by:

$$F_{z,fl} = \frac{1}{2}mgd_m - \frac{F_x h_{\text{cg}}}{l} + \frac{F_y h_{\text{cg}}}{\nu}d_{\text{LT}} + \frac{1}{2}F_l d_l \tag{A-74}$$

$$F_{z,fr} = \frac{1}{2}mgd_m - \frac{F_x h_{\text{cg}}}{l} - \frac{F_y h_{\text{cg}}}{\nu}d_{\text{LT}} + \frac{1}{2}F_l d_l \tag{A-75}$$

$$F_{z,rl} = \frac{1}{2}mg(1 - d_m) + \frac{mF_x h_{\text{cg}}}{l} + \frac{F_y h_{\text{cg}}}{\nu}(1 - d_{\text{LT}}) + \frac{1}{2}F_l(1 - d_l) \tag{A-76}$$

$$F_{z,rr} = \frac{1}{2}mg(1 - d_m) + \frac{mF_x h_{\text{cg}}}{l} - \frac{F_y h_{\text{cg}}}{\nu}(1 - d_{\text{LT}}) + \frac{1}{2}F_l(1 - d_l) \tag{A-77}$$

With wheelbase l, vehicle mass m, center of gravity height h_{cg}. The weight,aerodynamic downforce and lateral load transfer are distributed over the axles by d_m, d_l and d_{LT}. Note that in case of neglecting longitudinal and lateral load transfer, h_{cg} is assumed equal to zero. The aerodynamic drag F_d and downforce F_l in N are given by:

$$F_d = 0.5\rho C_d A V^2 \tag{A-78}$$

$$F_l = 0.5\rho C_l A (V \cos\beta)^2 \tag{A-79}$$

Where $C_d A$ and $C_l A$ are the drag and downforce coefficient times the frontal area, and ρ the air density. Finally, the wheel torques for the rear wheel drive model are defined as follows:

$$T_{fl} = T_{fr} = \begin{cases} 0 & \text{if } T \geqslant 0 \\ d_T T & \text{otherwise} \end{cases} \tag{A-80}$$

$$T_r = \begin{cases} T - T_{E,\text{drg}} & \text{if } T \geqslant 0 \\ (1 - d_T)T - T_{E,\text{drg}} & \text{otherwise} \end{cases} \tag{A-81}$$

With d_T the brake torque distribution. Note that in the brake balance calculation the $T_{E,\text{drg}}$ is not taken account. The magnitude of $T_{E,\text{drg}}$ follows from the wheel rotational velocities and engine drag power $P_{E,\text{drg}}$.

$$T_{E,\mathrm{drg}} = \frac{2P_{E,\mathrm{drg}}}{\omega_{rl} + \omega_{rr}} \tag{A-82}$$

The distribution of the rear axle torque T_r over the two rear wheels is determined by the model of the mechanical differential.

A-4 Differential model

The mechanical differential model is obtained from [1]. It can be interpreted as a clutch with coulomb friction characteristics, with the normal force acting on the clutch plates depending on the torque applied by the powertrain. This dependence is parameterized using three parameters, G_{drv}, G_{brk} and T_0 following the relation:

$$\Delta T_d = \mathrm{sign}(\omega_{rl} - \omega_{rr})T_{d,\max} \tag{A-83}$$

$$T_{d,\max} = \begin{cases} \max(G_{\mathrm{drv}}T_E \quad , T_0) & \text{if} \quad T_E > 0 \\ \max(-G_{\mathrm{brk}}T_E \quad , T_0) & \text{if} \quad T_E < 0 \end{cases} \tag{A-84}$$

Where the case $T_E < 0$ corresponds to a situation when the engine is in overrun. G_{drv}, G_{brk} are referred to as locking ratio on the drive and overrun side respectively. T_0 is the differential preload, placing a lower bound on the transmittable friction torque by the clutch plates. The torque from the powertrain T_E is calculated from the total wheel torque T and engine drag torque $T_{E,\mathrm{drg}}$ as follows:

$$T_E = \begin{cases} -T_{E,\mathrm{drg}} & \text{if} \quad \sum T \leq -T_{E,\mathrm{drg}} \\ \sum T & \text{otherwise} \end{cases} \tag{A-85}$$

Appendix B

Baseline model parameters

Table B-1: Baseline model parameters

Parameter	Meaning	Value	Unit
m	Vehicle mass	960	kg
I_{zz}	Yaw moment of inertia	1400	kgm^2
l	Wheel base	3	m
ν	Track width	1.5	m
h_{cg}	Center of gravity height	0.3	m
R_l	Tire loaded radius	0.35	m
R_{eff}	Tire effective rolling radius	0.35	m
d_{LT}	Front lateral load transfer distribution	0.50	-
d_m	Front weight distribution	0.47	-
d_T	Front braking torque distribution	0.60	-
T_0	Differential pre-load	100	Nm
G_{drv}	Differential locking ratio on drive side	0.8	-
G_{brk}	Differential locking ratio on overrun side	0.8	-
P_E	Engine power	400	kW
$P_{E,\text{drg}}$	Engine drag power	20	kW

Table B-2: Constants

Parameter	Meaning	Value	Unit
ρ	Air density	960	kgm^{-3}
g	Gravitational acceleration	9.81	ms^{-2}

Bibliography

[1] W. F. Milliken and D. L. Milliken, *Race car vehicle dynamics*. SAE International, 1995.

[2] D. Casanova, *On Minimum Time Vehicle Manoeuvring: The Theoretical Optimal Lap*. PhD thesis, Cranfield University, 2000.

[3] D. Brayshaw, *The use of numerical optimisation to determine on-limit handling behaviour of race cars*. PhD thesis, Cranfield University, 2004.

[4] B. Siegler, *Lap Time Simulation for Racing Car Design*. PhD thesis, The University of Leeds, 2002.

[5] M. Mühlmeier and N. Müller, "Optimization of the driving line on a race track," *SAE Technical Paper 2002-01-3339*, 2002.

[6] D. Casanova, R. Sharp, and P. Symonds, "Minimum time manoeuvring: The significance of yaw inertia," *Vehicle System Dynamics*, vol. 34, no. 2, pp. 77–115, 2000.

[7] D. P. Kelly, *Lap Time Simulation with Transient Vehicle and Tyre Dynamics*. PhD thesis, Cranfield University School of Engineering, 2008.

[8] G. Perantoni and D. Limebeer, "Optimal control for a formula one car with variable parameters," *Vehicle System Dynamics: International Journal of Vehicle Mechanics and Mobility*, vol. 52, 2014.

[9] G. Perantoni, A. Rao, and D. Limebeer, "Optimal control of formula one car energy recovery systems," *International Journal of Control*, vol. 87, 2014.

[10] G. Perantoni and D. Limebeer, "Optimal control of a formula one car on a three-dimensional track-part 2: Optimal control," *Journal of Dynamic Systems, Measurement, and Control*, vol. 137, May 2015. Accepted for publication.

[11] M. A. Patterson and A. V. Rao, "GPOPS-II: A matlab software for solving multiple-phase optimal control problems using hp-adaptive gaussian quadrature collocation methods and sparse nonlinear programming," *ACM Trans. Math. Softw.*, vol. 41, pp. 1–37, Oct. 2014.

[12] A. Rucco, G. Notarstefano, and J. Hauser, "Computing minimum lap-time trajectories for a single-track car with load transfer," in *IEEE 51st Annual Conference on Decision and Control (CDC)*, pp. 6321–6326, Dec 2012.

[13] A. Rucco, G. Notarstefano, and J. Hauser, "On a reduced-order two-track car model including longitudinal and lateral load transfer," in *European Control Conference (ECC)*, pp. 980–985, July 2013.

[14] A. Rucco, G. Notarstefano, and J. Hauser, "Optimal control based dynamics exploration of a rigid car with longitudinal load transfer," *IEEE Transactions on Control Systems Technology*, vol. 22, pp. 1070–1077, May 2014.

[15] A. Rucco, G. Notarstefano, and J. Hauser, "An efficient minimum-time trajectory generation strategy for two-track car vehicles," *IEEE Transactions on Control Systems Technology*, February 2015.

[16] J. Hauser, "A projection operator approach to the optimization of trajectory functionals," in *IFAC World Congress, Barcelona*, pp. 310–316, July 2002.

[17] J. Frasch, A. Gray, M. Zanon, H. Ferreau, S. Sager, F. Borelli, and M. Diehl, "An auto-generated nonlinear MPC algorithm for real-time obstacle avoidance of ground vehicles," in *European Control Conference (EEC), Zürich, Switzerland*, pp. 4136 – 4141, 2013.

[18] H. Bock and K. Plitt, "A multiple shooting algorithm for direct solution of optimal control problems," *Proceedings of the 9th IFAC World Congress, Budapest*, 1984.

[19] D. B. Leineweber, "An efficient multiple shooting based reduced SQP strategy for large-scale dynamic process optimization, part I & II," *Computers & Chemical Engineering*, vol. 27, pp. 157–174, 2003.

[20] R. Verschueren, S. De Bruyne, M. Zanon, J. Frasch, and M. Diehl, "Towards time-optimal race car driving using nonlinear MPC in real-time," in *IEEE 53rd Annual Conference on Decision and Control (CDC)*, pp. 2505–2510, Dec 2014.

[21] B. Mavroudakis, *About the Simulations of Formula 1 Racing Cars*. PhD thesis, University of Stuttgart, 2011.

[22] S. Fuchshumer, K. Schlacher, and T. Rittenschober, "Nonlinear vehicle dynamics control - a flatness based approach," in *Proceedings of the 44th IEEE Conference on Decision and Control*, 2005.

[23] S. C. Peters, *Optimal Planning and Control of Hazard Avoidance of Front-Wheel Steered Ground Vehicles*. PhD thesis, Massachusetts Institute of Technology, 2012.

[24] M. Mitschke and H. Wallentowitz, *Dynamik der Kraftfahrzeuge*. VDI-Buch, Springer, 2004.

[25] G. Rill, *Simulation von Kraftfahrzeugen*. Vieweg, 2007.

[26] T. Gustafsson, "Computing the ideal racing line using optimal control," Master's thesis, Linköping university, 2008.

[27] J. T. Betts, *Practical Methods for Optimal Control and Estimation Using Nonlinear Programming.* Advances in Design and Control, 2nd ed., 2010.

[28] D. E. Kirk, *Optimal control theory - An Introduction.* Dover Publications, Inc., 1970.

[29] M. B. Milam, *Real-Time Optimal Trajectory Generation for Constrained Dynamical Systems.* PhD thesis, California Institute of Technology, 2003.

[30] A. L. Schwarz, *Theory and Implementation of Numerical Methods Based on Runge-Kutta Integration for Solving Optimal Control Problems.* PhD thesis, University of California at Berkeley, 1996.

[31] D. Augustin and H. Maurer, "Computational sensitivity analysis of state constrained control problems," in *Optimization, Dynamics, and Economic Analysis* (E. Dockner, R. F. Hartl, M. Luptačik, and G. Sorger, eds.), pp. 12–21, Physica-Verlag HD, 2000.

[32] J. Nocedal and S. Wright, *Numerical Optimization.* Springer, 2nd ed., 2006.

[33] S. Leyffer and A. Mahajan, "Software for nonlinearly constrained optimization," *Wiley Encyclopedia of Operations Research and Management Science*, 2010.

[34] P. Gill, W. Murray, and M. Saunders, "SNOPT: an SQP algorithm for large-scale constrained optimization," *SIAM Review*, vol. 47, no. 1, pp. 99–131, 2005.

[35] A. Wächter and L. T. Biegler, "On the implementation of an interior-point filter line-search algorithm for large-scale nonlinear programming," *Mathematical Programming*, vol. 106, pp. 25–57, 2006.

[36] F. Curtis, J. Huber, O. Schenk, and A. Wächter, "A note on the implementation of an interior-point algorithm for nonlinear optimization with inexact step computations," *Mathematical Programming*, vol. 136, no. 1, pp. 209–227, 2012.

[37] O. Schenk, A. Wächter, and M. Hagemann, "Matching-based preprocessing algorithms to the solution of saddle-point problems in large-scale nonconvex interior-point optimization," *Computational Optimization and Applications*, vol. 36, no. 2-3, pp. 321–341, 2007.

[38] A. Wächter and L. T. Biegler, "Line search filter methods for nonlinear programming: Motivation and global convergence," *SIAM Journal on Optimization*, vol. 16, no. 1, pp. 1–31, 2005.

[39] A. Wächter, *An interior point algorithm for large-scale nonlinear optimization with applications in process engineering.* PhD thesis, Carnegie Mellon University, 2002.

[40] C. Büskens and D. Wassel, "The ESA NLP solver WORHP," in *Modeling and Optimization in Space Engineering* (G. Fasano and J. D. Pintúr, eds.), vol. 73 of *Springer Optimization and Its Applications*, pp. 85–110, Springer New York, 2013.

[41] M. Bittner, P. Bruhs, M. Richter, and F. Holzapfel, "An automatic mesh-refinement method for aircraft trajectory optimization problems," in *AIAA GNC and Co-Located Conferences*, pp. 710–719, 2013.

[42] Y. Zhao and P. Tsiotras, "Density functions for mesh refinement in numerical optimal control," *Journal of guidance, control and dynamics*, vol. 34, no. 1, 2011.

[43] K. J. Aström and R. M. Murray, *Feedback systems: An Introduction for Scientists and Engineers*. Princeton Universtity Press, Princeton and Oxford, 2009.

[44] Y. Kawajir, C. Laird, and A. Wächter, *Introduction to IPOPT, A Tutorial for downloading, installing and using IPOPT*, 2422 ed., November 2013.

[45] H. Maurer and H. J. Pesch, "Solution differentiability for nonlinear parametric control problems," *SIAM Journal on Control and Optimization*, vol. 32, no. 6, pp. 1542–1554, 1994.

[46] H. Maurer and D. Augustin, "Sensitivity analysis and real-time control of parametric optimal control problems using boundary value methods," in *Online Optimization of Large Scale Systems* (M. Grötschel, S. Krumke, and J. Rambau, eds.), pp. 17–55, Springer Berlin Heidelberg, 2001.

[47] H. Maurer and G. Vossen, "Sufficient conditions and sensitivity analysis for optimal bang-bang control problems with state constraints," in *System Modeling and Optimization* (A. Korytowski, K. Malanowski, W. Mitkowski, and M. Szymkat, eds.), vol. 312 of *IFIP Advances in Information and Communication Technology*, pp. 82–99, Springer Berlin Heidelberg, 2009.

[48] A. Fiacco, *Introduction to Sensitivity and Stability Analysis in Nonlinear Programming*. Mathematics in science and engineering, Academic Press, 1983.

[49] C. Büskens and H. Maurer, "Sensitivity analysis and real-time control of parametric optimal control problems using nonlinear programming methods," in *Online Optimization of Large Scale Systems* (M. Grötschel, S. Krumke, and J. Rambau, eds.), pp. 57–68, Springer Berlin Heidelberg, 2001.

[50] H. Pirnay, R. López-Negrete, and L. Biegler, "Optimal Sensitivity Based on IPOPT," *Mathematical Programming Computation*, vol. 4, no. 4, pp. 307–331, 2012.

[51] R. Fourer, D. M. Gay, and B. W. Kernighan, "A Modeling Language for Mathematical Programming," *Management Science*, vol. 36, pp. 519–554, 1990.

[52] D. M. Gay, "Automatic Differentiation of Nonlinear AMPL models," in *Automatic Differentiation of Algorithms: Theory, Implementation, and Application*, (Philadelphia), pp. 61–73, SIAM, 1991.

[53] R. Bartlett and L. Biegler, "QPSchur: A dual, active-set, Schur-complement method for large-scale and structured convex quadratic programming," *Optimization and Engineering*, vol. 7, no. 1, pp. 5–32, 2006.

Glossary

List of Acronyms

LMP1   Le Mans Prototype 1

TC   Traction Control

MTM   Minimal Time Maneuvering

NLP   Non-Linear Programming

QP   Quadratic Programming

SQP   Sequential Quadratic Programming

KKT   Karush-Kuhn-Tucker

BFGS   Broyden-Fletcher-Goldfarb-Shannon

NMPC   Nonlinear Model Predictive Control

NRMSD   Normalized root-mean-square deviation

QSS   Quasi-Steady State

OCP   Optimal Control Problem

SISO   single input, single output

RHP   right-half plane

List of Symbols

Greek Symbols

β Body slip angle

$\dot{\psi}$ Vehicle yaw angle

Γ_x Longitudinal load transfer

Γ_y Lateral load transfer

λ Lagrange multipliers of inequality constraints

Λ_u B-spline collocation matrix for augmented input vector

Λ_x B-spline collocation matrix for augmented state vector

ν Vehicle track width

ω Wheel rotational velocity

ρ Air density

σ_n Relative standard deviation of maneuver time

$\tilde{\Phi}$ Augmented vector of integration defects

Υ Initial boundary condition

ϱ_J Cost function scaling

ξ Angle relative to center-line angle

Latin Symbols

$\mathcal{F}$ Tire friction potential utilization

$\mathcal{N}_l(s)$ Maximum offset from center-line to left side, marking the track edge

s Absolute tire slip normalized by slip s_M for maximum tire force

$\tilde{c}$ Augmented vector of B-spline coefficients

$\tilde{g}$ Augmented vector of nonlinear equality constraints in x and u

$\tilde{q}$ Augmented vector of nonlinear inequality constraints in x and u

$\tilde{u}$ Augmented control input vector

$\tilde{x}$ Augmented state vector

$A_{y,\text{ssmax}}$ Maximal steady-state lateral acceleration

C Center-line curvature

$C_d A$ Aerodynamic drag coefficient multiplied by frontal area

$C_l A$ Aerodynamic lift coefficient multiplied by frontal area

d_{LT} Fraction of lateral load transfer at front axle

d_l Fraction of aerodynamic downforce on front axle

d_m Fraction of vehicle weight on front axle

d_T Fraction of total brake torque on front axle

F_d Aerodynamic drag force

F_l Aerodynamic downforce

F_x Longitudinal tire force

F_y Lateral tire force

g Nonlinear equality constraint functions in x and u

G_{brk} Differential locking ratio, overrun side

G_{drv} Differential locking ratio, drive side

h Distance discretization interval

h_{cg} Vertical distance of center of gravity to ground

I_z Vehicle yaw moment of inertia

k_u	B-spline order for input trajectory
k_x	B-spline order for state trajectory
l	Wheel base
L_u	B-spline collocation matrix for u
L_x	B-spline collocation matrix for x
m	Vehicle mass
M_{zp}	Potential yaw moment at maximal steady-state lateral acceleration
N	Number of discretization points
n	Distance perpendicular to center-line
$P_{E,\mathrm{drg}}$	Engine drag power
q	Nonlinear inequality constraint functions in x and u
R_l	Tire loaded radius
R_{eff}	Effective rolling radius
s	Distance along center line
S_f	Inverse velocity along center-line
s_x	Longitudinal tire slip
s_y	Lateral tire slip
T	Sum of torque on all wheels
T_E	Drivetrain torque on rear axle
T_0	Differential pre-load
$T_{E,\mathrm{drg}}$	Engine drag torque
u	Input vector in $\mathbb{R}^m$
V	Vehicle speed
x	State vector in $\mathbb{R}^n$

Subscripts

fl	Front-left tire
fr	Front-right tire
f	Front axle
r	Rear axle
rl	Rear-left tire
rr	Rear-right tire